

DISSERTATION

submitted to the
Combined Faculty of Natural Sciences and Mathematics
of
Heidelberg University, Germany
for the degree of
Doctor of Natural Sciences

Put forward by

Jonas Klüter

born in Lübeck, Germany

Oral examination: July 31st, 2020

**ON THE
USE OF *Gaia* FOR
ASTROMETRIC MICROLENSING**

Referees: Prof. Dr. Joachim Wambsganß
apl. Prof. Dr. Jochen Heidt

Abstract

On the use of *Gaia* for astrometric microlensing

Astrometric microlensing is a unique tool to directly determine the mass of an individual star (“lens”). By measuring the astrometric shift of a background source in combination with precise predictions of its unlensed position as well as of the lens position, it is possible to determine the mass of the lens with an uncertainty of a few per cent. In this thesis, the prediction of such astrometric microlensing events using the second data release of *Gaia* is presented, and the possibility of measuring the deflection of these events with *Gaia* is discussed. In the first part, it was possible to predict 3914 microlensing events between 2010 and 2065 with an expected astrometric shift larger than 0.1 mas. Of these events, 640 have a date of the closest approach between 2020 and 2030. Furthermore, 127 events could be found, which might lead to a photometric magnification larger than 1 mmag. Since the typical timescales of these events are of the order of a few months to years, it might be possible for *Gaia* to detect the deflections, and to determine the masses of the lenses. This is investigated in the second part of this thesis. For that purpose, the individual *Gaia* measurements for 501 events during the *Gaia* era (2014.5 - 2024.5) were simulated. It is shown that *Gaia* can detect the astrometric deflection for 114 events by simultaneously fitting the motions of lens and source stars. Furthermore, for 13 and for 34 events *Gaia* can determine the mass of the lens with a precision better than 15% and 30%, respectively. The results presented in this thesis allow the optimal selection of targets for future observational campaigns.

Zusammenfassung

Über die Verwendung von *Gaia* für astrometrisches Microlensing

Der astrometrische Mikrolinseneffekt bietet eine einzigartig Möglichkeit, die Masse eines einzelnen Sterns ("Linse") direkt zu bestimmen. Durch die genaue Messung der astrometrischen Verschiebung eines gelinsten Hintergrundsterns ("Quelle") und die präzise Voraussage sowohl der ungelinsten Position der Quelle als auch der Position der Linse ist es möglich, die Masse der Linse auf wenige Prozent genau zu bestimmen. Diese Arbeit beschäftigt sich mit der Vorhersage solcher astrometrischen Mikrolinsen-Ereignisse anhand der zweiten Datenveröffentlichung der *Gaia*-Raumsonde. Des Weiteren wird diskutiert, ob es für *Gaia* möglich ist, die Verschiebung der Quelle zu messen und so die Masse der Linse zu bestimmen. Im ersten Teil gelang es, 3914 Ereignisse im Zeitraum 2010 bis 2065 vorherzusagen, für die eine Verschiebung von mehr als 0,1 mas zu erwarten ist. 640 dieser Ereignisse werden ihre größte Annäherung zwischen 2020 und 2030 erreichen. Zudem konnten 127 Ereignisse gefunden werden, für die eine photometrische Verstärkung von mehr als 1 mmag möglich ist. Da die typische Zeitskala dieser Ereignisse mehrere Monate bis Jahre beträgt, könnte die astrometrische Verschiebung auch durch *Gaia* gemessen werden. Um zu überprüfen, wie gut *Gaia* in der Lage ist, die Massen der Linsen zu bestimmen, wurden im zweiten Teil dieser Arbeit für 501 Ereignisse, die während der *Gaia*-Mission (2014,5 - 2024,5) erwartet werden, die einzelnen *Gaia*-Messungen simuliert. Durch das gleichzeitige Fitten der Bewegung von Linse und Quelle konnte gezeigt werden, dass *Gaia* für 114 Ereignisse eine Verschiebung bestimmen kann. Des Weiteren kann *Gaia* für 13 bzw. 34 Ereignisse die Masse der Linse mit einer Genauigkeit besser als 15% bzw. 30% bestimmen. Die in dieser Arbeit präsentierten Ergebnisse ermöglichen eine optimierte Planung für weitere astrometrische Beobachtungen.

“Far out in the uncharted backwaters of the unfashionable end of the western spiral arm of the Galaxy lies a small unregarded yellow sun. Orbiting this at a distance of roughly ninety-two million miles is an utterly insignificant little blue green planet ...”

Hitchhiker’s Guide to the Galaxy, DOUGLAS ADAMS

Contents

Abstract	iii
Zusammenfassung	v
Contents	ix
1 Introduction	1
1.1 Outline	3
2 Gravitational lensing	5
2.1 Strong lensing	8
2.2 Weak lensing	9
2.3 Microlensing	10
2.3.1 Photometric microlensing	10
2.3.2 Astrometric microlensing	13
3 Gaia	19
3.1 Gaia satellite	19
3.1.1 The scanning law	20
3.1.2 Focal plane	21
3.1.3 Readout windows	23
3.1.4 Astrometric performance	24
3.2 Gaia catalogues	25
3.2.1 Gaia DR2	26
3.2.2 Upcoming data releases and data products	26
4 Prediction of astrometric microlensing events from Gaia DR2	27
4.1 Introduction	27
4.2 List of high-proper-motion stars	28
4.3 Background stars	32
4.4 Position forecast and determination of the closest approach	33
4.5 Approximate mass and Einstein radius	34
4.6 Results	37

4.6.1	Proxima Centauri - the nearest	42
4.6.2	Barnard's star - the fastest	42
4.6.3	Two microlensing events in 2018	42
4.6.4	Photometric microlensing effects of our astrometric microlensing events.	45
4.7	Summary and conclusion	47
5	Measuring stellar masses using astrometric microlensing with <i>Gaia</i>	51
5.1	Introduction	51
5.2	Data input	52
5.3	Simulation of <i>Gaia</i> 's individual astrometric measurements	53
5.3.1	Astrometry	54
5.3.2	Resolution	56
5.3.3	Measurement errors	56
5.4	Mass reconstruction and analysis of fit results	58
5.5	Results	59
5.5.1	Single background source	61
5.5.2	Multiple background sources	64
5.6	Summary and conclusion	67
6	Summary and perspectives	71
A	Tables	75
	List of Figures	81
	List of Tables	83
	List of Abbreviations	85
	Publications of Jonas Klüter	87
	Bibliography	91

Für meine Familie.

Chapter 1

Introduction

Gravitation is the most prominent force in the universe. It dominates many astrophysical processes on different scales, from the collapse of molecular clouds and the formation of stars and planets to the formation of galaxies. The appearance, structure and evolution of stars are also mainly defined by the mass of the stars. Even the formation and evolution of life on the Earth and our daily life is affected by the masses of the Sun, Earth, and Moon. For example, the orbital period T of the Earth around the Sun, that is the length of a year, is dependent on the mass of the Sun. Using the third Keplerian law, it can be determined by:

$$T^2 = \frac{4\pi^2}{G(M_\odot + M_E)} a_E^3, \quad (1.1)$$

where a_E is the semi major axis of the orbit of the Earth, and M_\odot and M_E are the masses of Sun and Earth, respectively. G is the gravitational constant.

Vice versa this can be used to estimate the mass of the Sun. This was done for the first time in 1687, by Isaac Newton in his work *Principia* (Cohen, 1998). Since the distance of the Sun was only poorly known, he corrected his estimates in the second and third edition of the *Principia*. Newton's last estimation of the solar mass ($169\,282 M_E$) still differs by a factor of 2 from the value known today ($332\,946 M_E$). Using this approach it is also possible to determine the masses of binary stars. With interferometric measurements, it is possible to determine the masses with uncertainties below 1% (Halbwachs et al., 2016). However, for most of the stars, it is extremely difficult or impossible to directly determine their mass. Typically, these are then estimated using the mass-luminosity relation (Hertzsprung, 1923; Russell et al., 1923):

$$\frac{L}{L_\odot} \sim \left(\frac{M}{M_\odot} \right)^{\tilde{\alpha}}. \quad (1.2)$$

where L is the luminosity and M is the mass of a star. The exponent $\tilde{\alpha} \approx 3$ can only be partially determined theoretically, and observation shows that a single power can hardly fit the entire mass range. Hence, the determination of the mass-luminosity function requires a set of accurately known masses. These are mainly derived from binary stars (Andersen, 1991; Torres et al., 2010). However, binary stars and isolated stars may evolve differently. Therefore, it is not known how well this empirical relation describes the masses of individual stars. Consequently, for a better understanding of the mass-luminosity relations, direct mass measurements of individual stars are important.

To directly measure the mass of an individual star, to date two methods can be used: asteroseismology and microlensing. Since asteroseismology shows a strong dependency on stellar models (Chaplin et al., 2014) it can not be used for robust mass measurements. Via microlensing on the other hand, it is possible to determine the mass with uncertainties in the order of a few per cent, either by observing positional deflection of astrometric microlensing events (Paczynski, 1991, 1995) or by detecting finite source effects in photometric microlensing events and measuring the microlens parallax (Gould, 1992).

As a sub-area of gravitational lensing (Einstein, 1915), microlensing describes the time-dependent positional deflection (astrometric microlensing) and magnification (photometric microlensing) of a background source due to an intervening star (“lens”). In comparison to photometric microlensing, astrometric microlensing has an important advantage: It can be observed at larger angular separations ($\Delta\phi \gg 1$ mas) between the background source and the foreground lens. This results in a longer timescale of the event of the order of months to years (Dominik and Sahu, 2000), and in the possibility to confidentially predict astrometric microlensing using stars with precisely known proper motion (Paczynski, 1995).

For this purpose, the *Gaia* mission (Gaia Collaboration et al., 2016b) of the European Space Agency (ESA) provides the ideal data set. Since mid-2014, *Gaia* observes the full sky on a regular basis, with an average of 14 observations per star and year. With its second data release (*Gaia* DR2), *Gaia* published precise proper motions for about 1.3 billion sources, allowing an extensive search for astrometric microlensing. Furthermore, due to the long timescale of an astrometric microlensing event, it might be possible for *Gaia* to measure the positional shift of the source and thereby determine the mass of the lens itself.

The aim of this thesis is to answer the following questions:

- 1) *Can Gaia DR2 be used to predict astrometric microlensing events?*

Is it possible by follow-up observations to detect the deflection for the predicted events in order to determine the mass of the lens?

- 2) *Is Gaia itself able to measure the deflection of the predicted microlensing events?*

If so, how precise will the mass determination by Gaia be?

What can be expected if additional external observations from the Hubble Space Telescope or the Very Large Telescope are included?

1.1 Outline

Starting with this introduction, the thesis is organised into six chapters. First, gravitational lensing is explained in Chapter 2. The chapter introduces the different effects and the fundamental equations. It is shortly discussed how strong lensing (Section 2.1) and weak lensing (Section 2.2) lead to a better picture of the universe, and how they benefit from *Gaia*. The main focus of this chapter is on astrometric and photometric microlensing. This is explained in Section 2.3, which also explains how both can be used to determine the mass of a star.

Afterwards, Chapter 3 presents the *Gaia* mission in more detail. In Section 3.1, the properties of the *Gaia* satellite and of the individual astrometric Gaia measurements are discussed while in Section 3.2, an overview of the current and upcoming *Gaia* data releases is given.

Chapter 4 covers the prediction of astrometric microlensing events from *Gaia* DR2. This chapter is mainly based on the two papers “Ongoing astrometric microlensing events of two nearby stars” and “Prediction of astrometric microlensing from *Gaia* DR2 proper motions” published by myself and my co-authors in Klüter et al. (2018a) and Klüter et al. (2018b).

In Chapter 5, the opportunities to measure the astrometric deflection of the predicted events with *Gaia* as well as the precision of *Gaia* in determining the mass of the lensing star is discussed. The result of this study is published in “Expectations on the mass determination using astrometric microlensing by *Gaia*” (Klüter et al., 2020).

Finally, in Chapter 6, the results of the previous chapters are summarised and discussed. An outlook on further studies as well as possible improvements of my studies are presented as well.

Chapter 2

Gravitational lensing

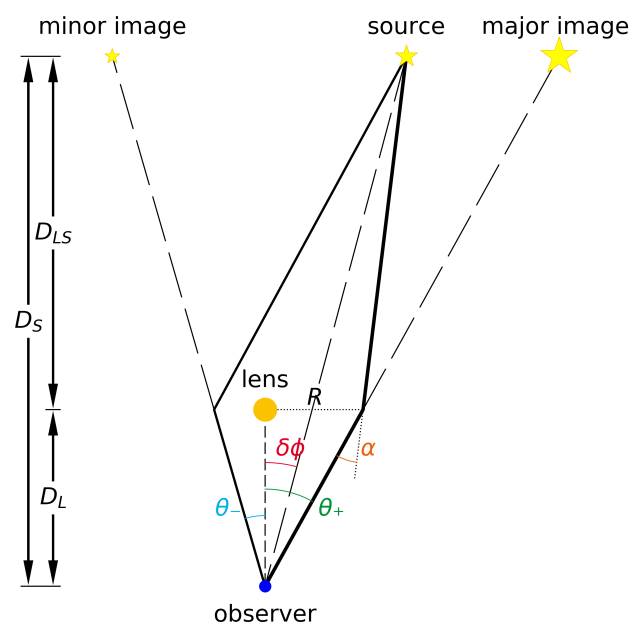


FIGURE 2.1: Light deflection by a point mass. If light from a distant source passes a lensing mass in a distance R , it is deflected by an angle α due to gravitational lensing. Thereby, two images of the source are created. Their angular separations are given by θ_+ and θ_- . The observed positions depend on the mass of the lens, the actual angular separation between lens and source β , and the distance of the lens D_S and source D_L (after [Refsdal, 1964](#), Figure 1).

In 1916, Albert Einstein published his theory of general relativity (Einstein, 1916). One of the predictions of his theory is that light passing a massive object is deflected due to the curvature of spacetime. The mass, therefore, acts as a “gravitational lens” and is called “lens” in the following. When light passes a point-like lens of mass M at a distance R it is deflected by the angle

$$\alpha = \frac{4GM}{c^2} \frac{1}{R}, \quad (2.1)$$

where G is the gravitational constant and c the speed of light. This angle is twice as large as the expected deflection for massive particles using Newtonian mechanics (Soldner, 1801). Consequently, the undeflected angular separation β between source and lens is slightly smaller than the observed angular separation θ (see Figure 2.1). This can be calculated, under the assumption $\beta, \theta, \alpha \ll 1$, by:

$$\beta = \theta - \frac{D_S - D_L}{D_S} \cdot \alpha(R) = \theta - \frac{4GM}{c^2} \frac{D_S - D_L}{D_S D_L} \frac{1}{\theta}, \quad (2.2)$$

where D_L, D_S is the distance of observer to the lens and source, respectively. In 1919, Arthur Eddington managed to measure the deflection by the Sun during a solar eclipse, and his result ($1.98'' \pm 0.18''$ and $1.60'' \pm 0.31''$), published by Dyson et al. (1920), is in a good agreement with Einstein’s prediction of $1.75''$ at the solar limb. Hence, gravitational lensing is the first confirmed prediction of Einstein’s theory of general relativity, although the uncertainty of Eddington’s measurement is rather large. Multiple recent and more precise measurements of the deflection by the Sun also agree with Einstein’s prediction (e.g. Bruns, 2018).

By solving Equation (2.2) for θ , two solutions can be found resulting in a major image (+) and a minor image (-). Their angular separations are given by (Paczynski, 1996a):

$$\theta_{\pm}(\beta) = \frac{\beta \pm \sqrt{\beta^2 + 16GM/c^2 \frac{D_S - D_L}{D_S D_L}}}{2}. \quad (2.3)$$

For stellar-mass lenses, the separation of the two images is on the order of milli-arc-seconds (mas) to micro-arc-seconds (μ as). Hence, modern instruments are required to measure this angle which was done for the first time only recently by Dong et al. (2019). However, by considering extragalactic sources lensed by galaxies or galaxy clusters the separation between the images is much larger (see Section 2.1). Therefore, gravitational lensing was initially envisaged to be observable only for extragalactic sources (Zwicky, 1937).

Furthermore, gravitational lensing leads to a distortion of an extended source. This effect

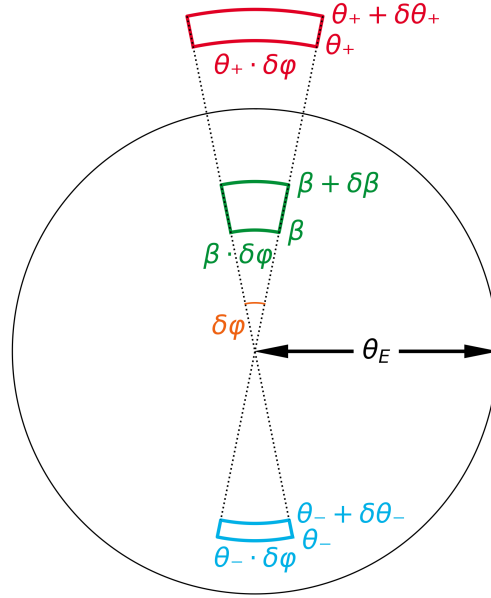


FIGURE 2.2: Distortion due to gravitational lensing. An extended source (green box) gets distorted due to gravitational lensing. The two images (red and blue boxes) are tangentially elongated. Their radial sizes get reduced ($\delta\theta_{\pm} < \delta\beta$), while the azimuthal component ($\delta\varphi$) is conserved. In case of a perfect alignment a ring (black circle) with the size of $1\theta_E$ can be observed. The surface ratio between unlensed and lensed images reflects the magnification of the source (after Congdon and Keeton, 2018, Figure 2.3).

arises because the light is only deflected and focused on the radial component, whereas the azimuthal component stays unaffected (see Figure 2.2). For small angular separations, an extended source appears as an arc, and in the case of perfect alignment of source and lens, a so-called Einstein ring can be observed. Its size is given by the Einstein radius (Chwolson, 1924; Einstein, 1936; Paczyński, 1986a):

$$\theta_E = \sqrt{\frac{4GM_L}{c^2} \frac{D_S - D_L}{D_S \cdot D_L}} = 2.854 \text{ mas} \sqrt{\frac{M_L}{M_{\odot}} \cdot \frac{\varpi_L - \varpi_S}{1 \text{ mas}}}, \quad (2.4)$$

where $\varpi_{L,S}$ is the the parallax of the lens and source, respectively. The Einstein radius provides a natural scale for gravitational lensing and is therefore often used to express the lens equation in dimensionless units:

$$u = \frac{\beta}{\theta_E}. \quad (2.5)$$

By applying this, Equation (2.3) can be simplified:

$$\theta_{\pm}(u) = \frac{u \pm \sqrt{u^2 + 4}}{2} \theta_E. \quad (2.6)$$

In addition, the apparent brightness of a source is magnified due to gravitational lensing. Since gravitational lensing is a purely geometrical effect and does involve neither emission nor absorption, the surface brightness is constant. The magnification of the two images A_{\pm} can be obtained from the ratios of their areas (see Figure 2.2) (Paczynski, 1986a):

$$A_{\pm} = \left| \frac{\theta_{\pm}}{\beta} \frac{d\theta_{\pm}}{d\beta} \right| = \frac{u^2 + 2}{2u\sqrt{u^2 + 4}} \pm \frac{1}{2}. \quad (2.7)$$

The appearance of gravitational lensing depends on the different masses and mass distribution of the lens as well as on the angular separation between lens and source. Hence, gravitational lensing is divided into three categories, *strong lensing*, *weak lensing*, and *microlensing*, each with a slightly different scientific case. The main topic of this thesis is microlensing. Nevertheless, a short presentation of strong and weak lensing with a focus on their use cases and their benefit from the *Gaia* mission, is given.

2.1 Strong lensing

The appearance of distant sources as multiple resolved images and the formation of arcs or even Einstein rings is called “strong lensing”. These phenomena only appear if light passes through a strong gravitational field, usually created by galaxies or galaxy clusters. Hence, a close angular alignment between lens and source is necessary (of the order of the Einstein radius). The first strongly lensed object was discovered in 1979 by Walsh et al. (1979): a double imaged quasar. Afterwards, strong lensing became a powerful tool to study the properties of lensing galaxies as well as the evolution and composition of the universe. Due to the extended mass distribution of the lens, it is often possible to detect more than two images of the same source. By using the position and brightness of the different images, it is possible to estimate simple models for

the mass distribution of the lens. Due to the large discrepancy between the determined masses and estimates based on the luminosity of the galaxy, strong lensing provides solid evidence for the existence of dark matter (Congdon and Keeton, 2018). Another use case of strong lensing is the detection of far distant sources from the early universe. The photometric magnification allows the detection of objects which are otherwise too faint. Several of the most distant known objects are magnified by strong lensing (e.g. Coe et al., 2012; Zheng et al., 2012). By studying strongly lensed objects, it is also possible to draw conclusions on the universe as a whole. Light from the different images travels along slightly different paths which differs especially in length. Consequently, if the sources vary with time, as expected to be the case for quasars, time delays between the different images can be observed. The time delays do not only depend on the distance and alignment of lens and source, but also on cosmological parameters. Hence, strong lensing provides an independent method to determine the Hubble constant H_0 (Refsdal, 1964). Several working groups are therefore searching for strongly lensed quasars and try to measure time delays. *Gaia* is expected to detect about 600,000 quasars, of which about 2500 are expected to be strongly lensed (Finet and Surdej, 2016). The first two *Gaia* data releases already led to the discovery of a few dozens of multiply imaged quasars (e.g. Ostrovski et al., 2018; Krone-Martins et al., 2018; Lemon et al., 2018; Wertz et al., 2019; Krone-Martins et al., 2019) and several dozen candidates (e.g. Delchambre et al., 2019).

2.2 Weak lensing

Arcs and multiple images are only created when the lens and source are in very close alignment. At larger angular separations, gravitational lensing only leads to a slight shear and magnification of the size of background galaxies. This phenomenon is called weak lensing (Kaiser and Squires, 1993; Brainerd et al., 1996). Since the distortion is superposed with the intrinsic ellipticity of the background galaxies, weak lensing can only be detected by a statistical analysis of several background sources, i.e galaxies. While the intrinsic parameters are homogeneously distributed over a larger sample, the shear due to gravitational lensing always acts tangentially, thus creating an anisotropy. Therefore, correlations between the shape and orientation can reveal the mass density distribution of the lens (Kaiser and Squires, 1993). Beside others, such observations have led to the detection of dark matter halos in nearby galaxy clusters. Especially the gravitational deflection by the Bullet Cluster provides strong evidence for dark matter. Since other theories,

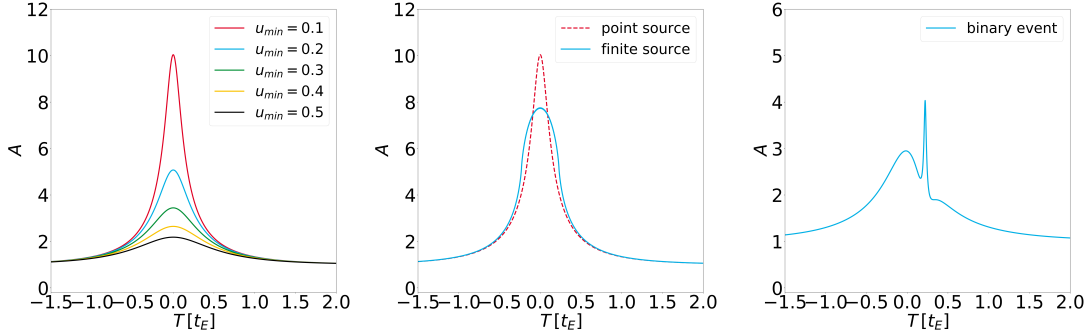


FIGURE 2.3: Light curves of photometric microlensing events. Left: Light curves of a point lens and point source for different impact parameters ranging from $0.1 \theta_E$ to $0.5 \theta_E$. Middle: Light curve of a finite source (blue solid line) in comparison with the point source (red dashed line). In both cases, the impact parameter is $0.1 \theta_E$. Right: Light curve of a binary lens (after Paczyński, 1996a, Figure 5).

e.g. modified Newtonian dynamics can not explain the misalignment of luminous matter and the centre of the gravitational deflection (Clowe et al., 2006).

2.3 Microlensing

Originally, microlensing was introduced by Paczyński to describe the magnification of unresolved images, regardless if the lens is within our Milky Way or in distant galaxies (Paczynski, 1986a,b). Due to modern astrometric instruments, it is nowadays also possible to measure the deflection of the background sources. This phenomenon is called “astrometric microlensing”, and was suggested by Paczyński (1996b) and Miralda-Escude (1996). For clarification, the magnification of a background source in this context is usually called “photometric microlensing”. Both effects can only be observed if they vary over time since the unlensed position and the unmagnified brightness of the source are unknown.

2.3.1 Photometric microlensing

When a lens passes a source with a sufficiently small angular separation, a characteristic increase and decrease of the brightness of the source can be observed. Figure 2.3 shows the corresponding

light curve for several impact parameters. For a dark point-like lens and a point-like source, the light curve only depends on the scaled angular separation u , given by:

$$A = A_+ + A_- = \frac{u^2 + 2}{u \sqrt{u^2 + 4}}. \quad (2.8)$$

At large angular separations ($u \gg 1$), the magnification shows a strong decline (Dominik and Sahu, 2000):

$$A \simeq 1 + \frac{2}{u^4}. \quad (2.9)$$

Hence, a magnification is only observable when the impact parameter is on the order of the Einstein radius. This also means that the time scale of a photometric microlensing event is quite short. It can be estimated by the Einstein ring crossing time, expressed by Gould (1992):

$$t_E = \frac{2\theta_E}{\mu_{rel}}, \quad (2.10)$$

where μ_{rel} is the absolute value of the relative proper motion between lens and source. For stellar-mass lenses within the Milky Way, the timescale is typically on the order of a few days or weeks. The observed magnification of photometric microlensing events can further be reduced due to luminous lenses. By considering a flux ratio $f_{LS} = f_L/f_S$ between the lens and the unmagnified source star, the resulting observable magnification is given by

$$A_{lum} = \frac{f_{LS} + A}{f_{LS} + 1}. \quad (2.11)$$

The magnitude change Δm can be calculated via:

$$\Delta m = 2.5 \cdot \log_{10} \left(\frac{f_{LS} + A}{f_{LS} + 1} \right). \quad (2.12)$$

It might also be blended by further stars close-by to the sky. However, in the context of this thesis only the blending from the lens is of interest.

Due to the requirement of close angular alignments between lens and source, the chance of a source to be lensed at any given time is very low. Towards the galactic bulge it is about 2.3×10^{-6} (Mróz et al., 2019). In 1986, Paczyński (1986b) suggested monitoring a few million stars in the Magellanic Clouds in order to detect photometric microlensing events. He estimated that for each star the probability to be lensed by a dark compact halo object at any given time

is roughly one in a million, if the missing matter in the Milky Way halo is made of objects with masses greater than $10^{-8} M_{\odot}$.

Several photometric events were observed afterwards (e.g. [Alcock et al., 1993](#); [Aubourg et al., 1993](#)), but the observed occurrence rate was lower than expected, only one in 10 million ([Bennett, 2005](#)). Consequently, it was concluded, that only a few per cent of the missing matter can be explained by massive astrophysical halo objects ([Tisserand et al., 2007](#); [Griest et al., 2013](#)).

Nowadays microlensing is primarily used to search for extrasolar planets. For that purpose, millions of stars are monitored in dense regions towards the bulge by several surveys such as the Optical Gravitational Lensing Experiment (OGLE) ([Udalski, 2003](#)), the Microlensing Observations in Astrophysics (MOA) ([Bond et al., 2001](#)) or the Korea Microlensing Telescope Network (KMTNet) ([Kim et al., 2016](#)). By using densely-sampled light curves, it is possible to detect features indicating a binary lens (e.g. [Bond et al., 2004](#)) (see Figure 2.3). Up to today, microlensing has led to the detection of 105 extrasolar planets¹, which orbit their host stars with separations from 0.5 AU to 18 AU, and masses from $\sim 1.4 M_{\text{Earth}}$ to $\sim 13 M_{\text{Jupiter}}$. Hence, microlensing covers a much different area of the (mass-separation) parameter space than the transit method and the radial velocity method. Consequently, it provides a better basis for a statistical census of planetary systems, and has led to the insight that there are “One or more bound planets per Milky Way star” ([Cassan et al., 2012](#)).

In some cases, it is also possible to determine the mass of a single lens. For that purpose, it is necessary to determine the Einstein radius and the distance of lens and source. In principle, the Einstein radius can be determined using the duration of an event and the relative proper motion via Equation (2.10). However, an astrometric measurement of the proper motion and parallax is rarely possible, due to the required precision and resolution. Another option is to use finite-source effects if they can be detected ([Gould, 1994b](#)). These arise when the separation between lens and source is on the order of the angular size of the source. Different areas of the source are then magnified differently, leading to a “flattened” light curve (see Figure (2.3)). The size of the source in units of Einstein radii ρ can then be determined from a light-curve fit. By comparing this value with the expected stellar radius R based on the spectra and luminosity of the source, it is possible to determine the Einstein radius:

$$\theta_E = \frac{R}{\rho \cdot D_S}. \quad (2.13)$$

¹The Extrasolar Planets Encyclopaedia: <http://www.exoplanet.eu>, accessed on May 13th 2020.

To determine the difference between the parallax of the lens and source ($\varpi_{rel} = \varpi_L - \varpi_S$), one option is to observe the microlensing event from two well-separated locations (Gould, 1994a), ideally using a space telescope with a distance to Earth on the order of one AU. Due to the different arrangement of the lens, the source and the telescope, two different light curves will be observed from the two sites. The parallax over the Einstein radius $\varpi_E = \varpi_{rel}/\theta_E$ can then be determined from the difference of the observed impact parameter, divided by the distance between the telescopes. Via

$$M = \frac{c^2}{4G} \frac{1 \text{ AU}}{\varpi_E} \theta_E \quad (2.14)$$

it is then possible to determine the mass of the lens (Gould, 1992). Using the data of OGLE and Spitzer Telescope, it was possible to determine the mass of a few isolated stars (e.g. Zhu et al., 2016; Chung et al., 2017; Shvartzvald et al., 2019; Zang et al., 2020). In addition to the uncertainties of the light-curve fit, the results also depend on the astrophysical relations used to determine the radius of the source.

For some long-duration events, *Gaia* can detect the rise of a photometric event. These are published through the *Gaia* alert system. While it is not possible to measure a densely sampled light curve, *Gaia* can contribute a few data points helping to determine ϖ_E . This was used among others in Wyrzykowski et al. (2020)

2.3.2 Astrometric microlensing

In astrometric microlensing, the signal of interest is the change of the position of the background star. Figure 2.4 shows the deflection of a background source due to an intervening lens. Besides the strength of the deflection, also the direction changed over time. Using the two-dimensional unlensed angular separation $\Delta\phi$ between lens and source, the two-dimensional unlensed scaled angular separation can be determined as

$$\mathbf{u} = \Delta\phi/\theta_E. \quad (2.15)$$

The position of the two images with respect to the unlensed position of the source is given by:

$$\delta\theta_{\pm} = \frac{u \pm \sqrt{u^2 + 4}}{2} \cdot \frac{\mathbf{u}}{u} \cdot \theta_E - \mathbf{u} \cdot \theta_E = \frac{\pm \sqrt{u^2 + 4} - u}{2} \cdot \frac{\mathbf{u}}{u} \theta_E, \quad (2.16)$$

For the major image (+), the shift is at most $1 \theta_E$, when lens and source are perfectly aligned. In those cases, it is usually not possible to resolve the two images. Hence, only the centre of light

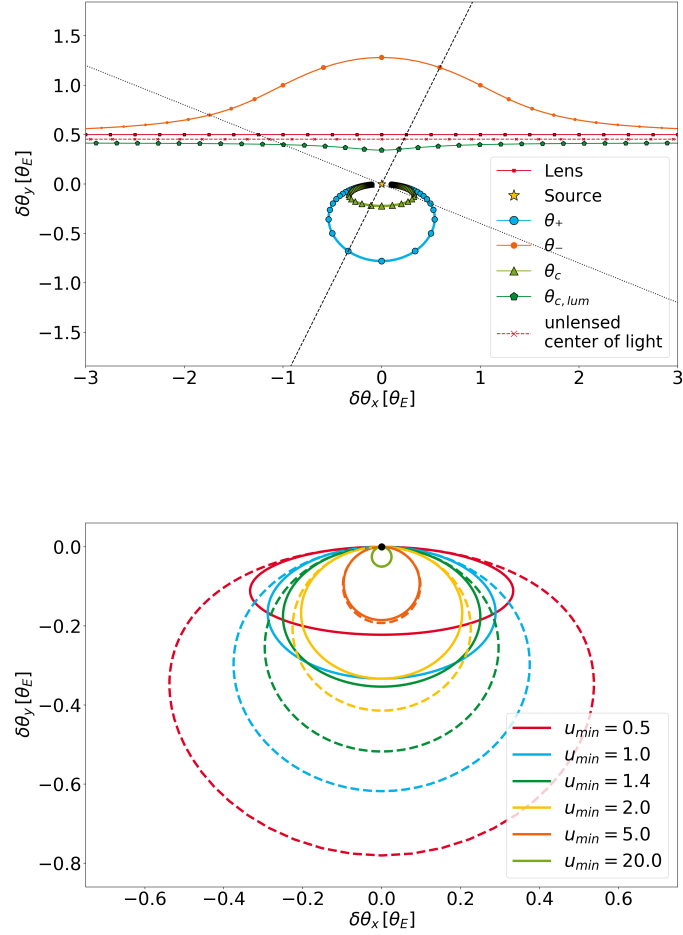


FIGURE 2.4: Top: Positional shift in units of Einstein radii for an astrometric microlensing event with an impact parameter of $u = 0.75$. While the lens (red, squares) passes a background star (yellow star, fixed at the origin), two images (major image: blue circles, minor image: orange circles) of the source are created due to gravitational lensing. This also leads to a shift of the centre of light, shown in light green (triangles) for a dark lens. In dark green (pentagons), the centre of the combined light is shown for a flux ratio of $f_{LS} = 10$. The unlensed centre of the combined light is shown as a red dashed line. The markers correspond to certain time steps. Each of the two black lines connects the positions of for a given epoch (based on Paczyński, 1996a, Figure 3). Bottom: Astrometric shift for different impact parameters u_{min} . The black dot shows the fixed unlensed source position. The solid lines indicate the shift of the centre of light for a dark lens and the dashed lines indicate the shift of the brighter image. The maximum shift of the centre of light is reached at an angular distance of $u = \sqrt{2}$ (green) (Paczynski, 1998), whereas the shift of the brightest image has its maximum in case of a perfect alignment ($u = 0$) (based on Dominik and Sahu, 2000, Figure 4); (adapted from Klüter et al., 2018b, Figure 1).

can be observed (see Figure 2.4). For a dark lens, the position of the centre of light is given by:

$$\theta_c = \frac{A_+ \theta_+ + A_- \theta_-}{A_+ + A_-} = \frac{u^2 + 3}{u^2 + 2} \cdot \mathbf{u} \cdot \theta_E, \quad (2.17)$$

where A_{\pm} is the magnification of the two images, respectively, given in Equation (2.7). The corresponding angular shift of the centre of light can be calculated by:

$$\delta\theta_c = \frac{\mathbf{u}}{u^2 + 2} \cdot \theta_E. \quad (2.18)$$

Due to the blending of the minor image the maximum deflection is $\delta\theta_{c,max} = 0.35\theta_E$ at a separation of $u = \sqrt{2}$ (see Figure 2.4, bottom panel). A bright lens further decreases the observable deflection. The position of the centre of light of the combined system relative to the lens can be calculated by (Hog et al., 1995; Miyamoto and Yoshii, 1995; Walker, 1995):

$$\theta_{c,lum} = \frac{A_+ \theta_+ + A_- \theta_-}{A_+ + A_- + f_{LS}} \quad (2.19)$$

and the shift between lensed and unlensed position can be determined via

$$\delta\theta_{c,lum} = \frac{\mathbf{u} \cdot \theta_E}{1 + f_{ls}} \frac{1 + f_{LS}(u^2 + 3 - u\sqrt{u^2 + 4})}{u^2 + 2 + f_{LS}u\sqrt{u^2 + 4}}. \quad (2.20)$$

Hence, astrometric microlensing can only be observed for events with large Einstein radii (see Figure 2.5).

While the photometric magnification can only be observed when the impact parameter is on the order of the Einstein radius, it is possible to observe the astrometric deflection at larger angular separations $u \gg \sqrt{2}$, due to a weaker dependency:

$$\delta\theta_c \simeq \delta\theta_+ \simeq \frac{\theta_E}{u} = \frac{\theta_E^2}{|\Delta\phi|} \propto \frac{M_L \cdot (\varpi_L - \varpi_S)}{|\Delta\phi|}, \quad (2.21)$$

which scales with $1/u$ rather than with $1/u^4$. (see Equation (2.9)). For large angular separations, the deflection is also directly proportional to the mass of the lens. Consequently, in comparison to photometric microlensing, astrometric microlensing can also be observed at larger angular separations. This results in a much longer timescale during which an astrometric microlensing event can be observed (Paczynski, 1996b; Miralda-Escude, 1996) (see Figure 2.5).

The timescale can be approximated by (Honma, 2001)

$$t_{aml} = t_E \sqrt{\left(\frac{\theta_E}{\theta_{min}}\right)^2 - u_{min}^2}, \quad (2.22)$$

where θ_{min} is the precision threshold of the used instrument and t_E the Einstein ring crossing time (Equation 2.10). Nowadays, highly accurate astrometry can reach a precision of $\theta_{min} = 0.5$ mas or lower. With such high-precision instruments, some events can be observed over many months or even a few years (see Figure 2.5). Therefore, astrometric microlensing can also be directly measured by high-precision, long-term surveys like *Gaia*, if the lensed stars are observed at a sufficient number of epochs suitably distributed in time.

Equation 2.18 is also a good approximation for the shift of the brightest image when the second image is negligibly faint, which is usually the case for ($u > 5$). This approximation will mostly be used in Chapter 5.

The limitation to events with large Einstein radii results in a much smaller event rate, compared to photometric microlensing. Furthermore, it is only measurable using high-precision instruments. Consequently, monitoring several million stars as done for photometric microlensing is also not feasible. However, since the alignment of lens and source does not need to be within $1 \theta_E$, it is possible to confidently predict astrometric microlensing events using precise proper motion catalogues, as presented in Chapter 4.

Aside from the deflection caused by the Sun, astrometric microlensing was only recently observed for the first time. In 2014, Sahu et al. (2017) measured the deflection by the nearby white dwarf Stein 2051 B using the Hubble Space Telescope (HST) equipped with the Wide Field Camera 3 (WFC3). They derived a mass of $0.675 \pm 0.051 M_\odot$. This shows the potential of astrometric microlensing to measure the mass with a precision of a few per cent (Paczýński, 1995). For the second time, Zurlo et al. (2018) measured the shift of a background source caused by Proxima Centauri in 2016 using the Very Large Telescope (VLT) equipped with the SPHERE² coronagraph. They determined a mass of $0.150^{+0.062}_{-0.05} M_\odot$.

²Spectro-Polarimetric High-contrast Exoplanet REsearch

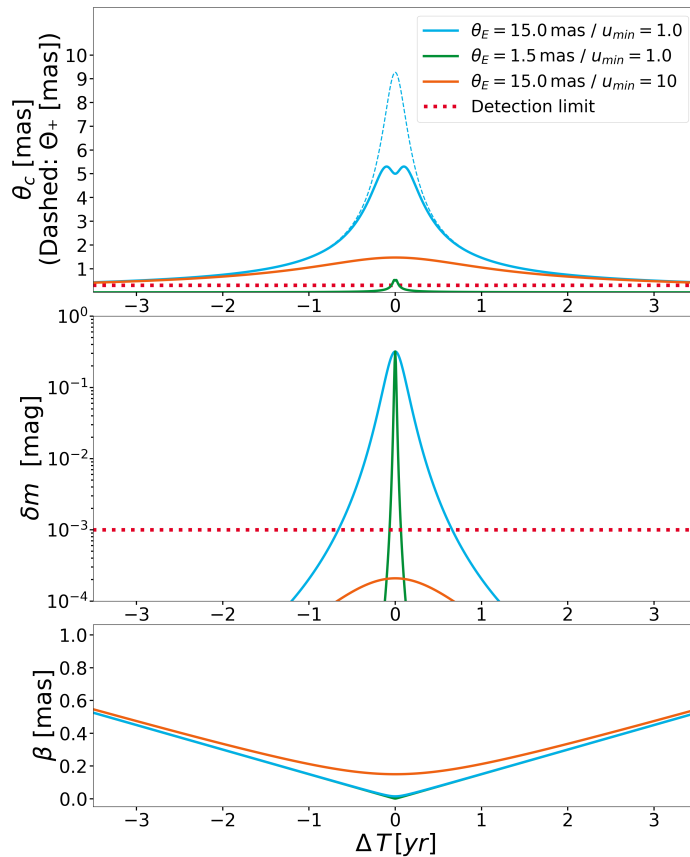


FIGURE 2.5: Comparison between astrometric microlensing and photometric microlensing. Top: Absolute astrometric deflection. Middle: Photometric magnification. Bottom: Angular separation between lens and source. The red dashed lines indicate a detection limit of 0.5 mas and 1 mmag, respectively. In blue, orange and green, the light curve and astrometric deflection for three different events are shown. The Einstein radius of the blue event is $\theta_E = 15$ mas and the impact parameter is $u_{min} = 1$. The dashed line shows the shift of the brightest image and the solid line indicates the shift of the centre of light assuming a dark lens. The event is detectable photometrically and astrometrically, however the duration of the astrometric event is much longer than the duration of the magnification. The orange event has the same Einstein radius, but a larger impact parameter of $u_{min} = 10$. This event is only detectable astrometrically. For the green event, the Einstein radius is by a factor of 10 smaller ($\theta_E = 1.5$ mas), and the impact parameter is $u_{min} = 1$. An astrometric deflection can only hardly be observed, while the maximum magnification is as large as for the blue event.

Chapter 3

Gaia

In this chapter, I present the properties of the *Gaia* satellite and the *Gaia* data releases. The details can be found in (Gaia Collaboration et al., 2016b), on the main *Gaia* web pages^{3,4} and in the Data Release Documentation⁵. More detailed references are provided for each section separately.

3.1 *Gaia* satellite

The *Gaia* satellite is an astrometric space telescope of the European Space Agency (ESA). *Gaia* was launched in December 2013 and is located at the Lagrangian Point L2 of the Sun-Earth system, 1 500 000 km away from the Earth. The main scientific goal of *Gaia* is to measure the position and motion of more than a billion stars and thereby create a 3-dimensional map of the Milky Way, and to determine the kinematics of the galaxy. *Gaia* will also detect and characterise several thousand solar-system objects and exoplanets as well as several million extragalactic sources, leading to a variety of scientific fields benefiting from *Gaia* (Mignard, 2005). For that purpose, *Gaia* observes the full sky with high astrometric precision. The nominal mission started in mid-2014 and ended in mid-2019 after 5 years. However, *Gaia* might continue to observe until mid-2024, leading to a 10-years baseline. An extension until the end of 2022 is already approved⁶.

³*Gaia* main web page: <http://www.cosmos.esa.int/web/gaia>, accessed on May 13th 2020.

⁴*Gaia* main web page: <http://sci.esa.int/gaia/>, accessed on May 13th 2020.

⁵*Gaia* Data Release Documentation: <https://gea.esac.esa.int/archive/documentation/GDR2/index.html>, accessed on May 13th 2020.

⁶*Gaia* Data Release Scenario: <https://www.cosmos.esa.int/web/gaia/release>, accessed on May 13th 2020.

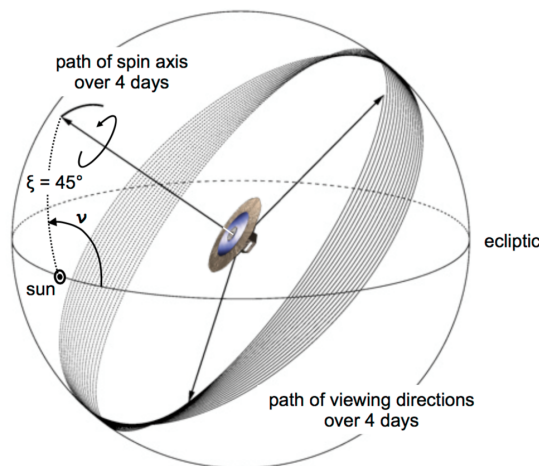


FIGURE 3.1: Illustration of *Gaia*'s scanning law. The figure shows the different rotational motion of *Gaia*. Further, the path of the spin axis over 4 days and the corresponding path of the preceding field of view is displayed (from [Gaia Collaboration et al., 2016b](#)).

3.1.1 The scanning law⁷

Gaia is not meant to be pointed towards specified targets, but observes the sky on a regular basis defined by a nominal (pre-defined) scanning law, consisting of various periodic motions (see Figure 3.1). *Gaia* rotates with a period of 6 hours around itself. Further, *Gaia*'s spin axis is inclined by $\xi = 45^\circ$ to the Sun, with a precession frequency of one turn every 63 days. Finally, due to its position at L2, *Gaia* orbits the Sun once a year. Additionally, *Gaia* is not fixed at L2, but is moving on a 100 000 km Lissajous-type orbit around L2. On average, each source is observed about 70 times during the nominal 5-year mission (2014.5-2019.5). However, certain parts of the sky are inevitably observed more often. For the nominal mission Figure 3.2 shows the number of focal-plane transits as function of position on the sky. At ecliptic latitudes of about $\pm(90^\circ\xi) = \pm 45^\circ$, *Gaia* observes each source up to 200 times in 5 years. Whereas, some regions are only observed 40 times during the nominal mission.

The 6 hour rotation is fixed, due to the synchronous readout of the CCD chips (see Section 3.1.2). The precession frequency and inclination are chosen to provide optimal constraints for the astrometric solutions. Whereas, the initial phase of the rotation and precession are free

⁷*Gaia* Data Release Documentation - The scanning law in theory:
https://gea.esac.esa.int/archive/documentation/GDR2/Introduction/chap_cu0int/cu0int_sec_mission/cu0int_ssec_scanning_law.html, accessed on May 13th 2020.

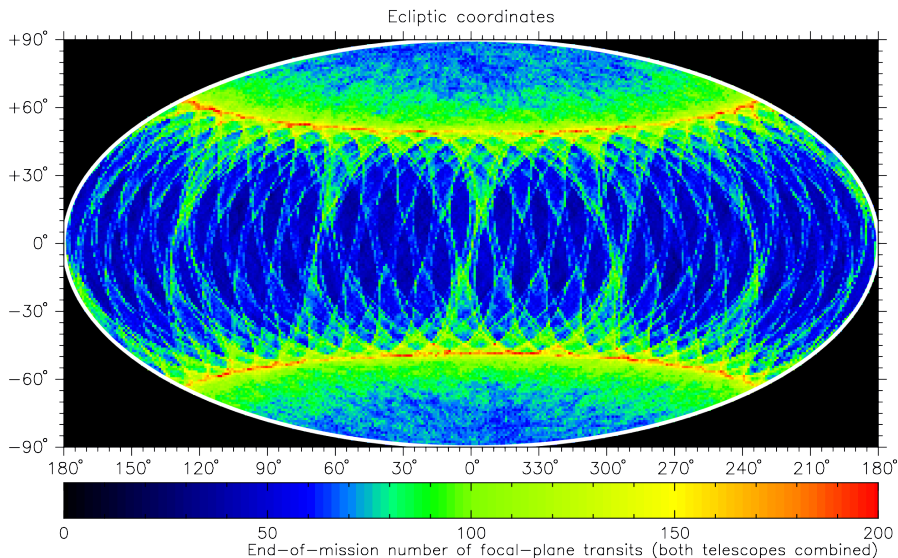


FIGURE 3.2: Number focal-plane transits for the nominal mission of *Gaia* as a function of ecliptic coordinates. The high number of focal plane transits around ecliptic latitudes of 45° are caused by the fixed solar aspect angle in the scanning law (ESA⁸).

parameters, these were optimised to the benefit of the observation of bright stars in the vicinity of Jupiter (Gaia Collaboration et al., 2016b) which allows the measurement of quadrupole moments of the light deflection by Jupiter (de Bruijne et al., 2010).

3.1.2 Focal plane⁹

Gaia is equipped with two separate telescopes with rectangular primary mirrors, pointing on two different fields of view, separated by 106.5° . This, for any given star typically results in two observations a few hours apart with the same scanning direction. The light from the two fields of view is focused on one common focal plane in order to precisely measure large-scale separations. The focal plane is equipped with 106 CCDs arranged in 7 rows (see Figure 3.3). The majority of the CCDs (62) are used for the astrometric field. While *Gaia* rotates, a source moves within two minutes over the focal plane, thereby, passing all CCDs in one of the rows.

⁸Image: End-of-mission focal plane transits: <https://www.cosmos.esa.int/web/gaia/transits>, accessed on May 13th 2020.

⁹*Gaia* Data Release Documentation - The spacecraft: https://gea.esac.esa.int/archive/documentation/GDR2/Introduction/chap_cu0int/cu0int_sec_mission/cu0int_ssec_spacecraft_intro.html, accessed on May 13th 2020.

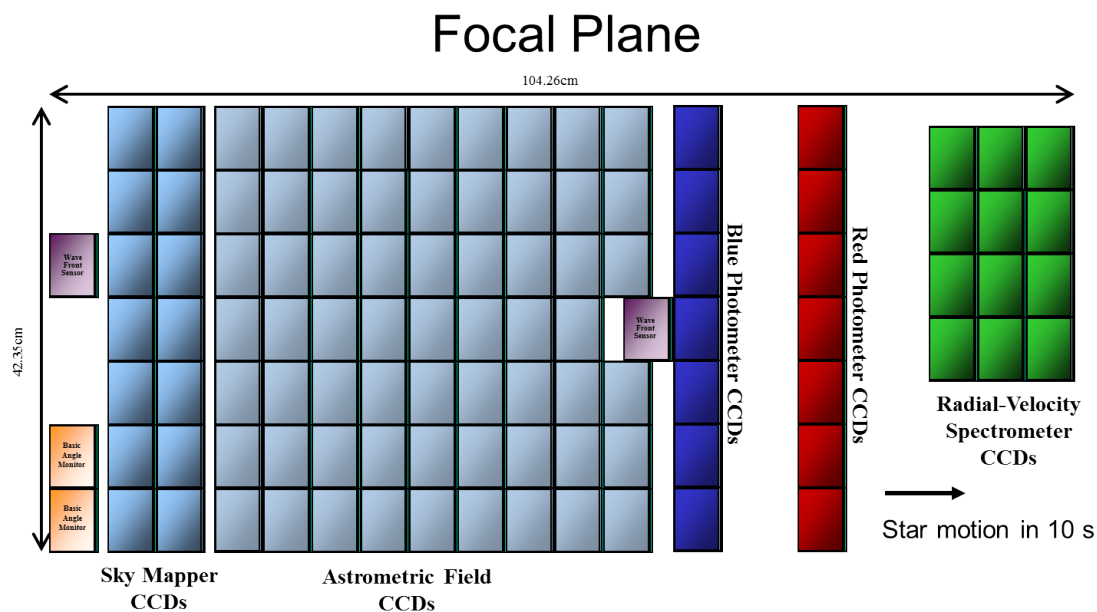


FIGURE 3.3: The focal plane of *Gaia* is equipped with 106 CCDs. It is devoted into five categories: the sky mapper, the astrometric field, two photometers, a radial velocity spectrometer, and sensors for monitoring and operating. During a focal-plane transit, a source passes the focal plane in roughly 2 minutes from left to right (ESA¹⁰).

First, it passes one of the two so-called sky mappers, which can differentiate between both fields of view. The data from the sky mapper is mainly used to trigger the readout of the succeeding CCD chips. Afterwards, the star passes nine CCDs of the astrometric field (the middle row only contains eight CCDs). The astrometric field is devoted to position measurements, and G band photometry. Then two low-resolution spectra are taken by the blue (330 – 680 nm) and red (640 – 1050 nm) photometer. Their integrated flux is given as G_{Bp} and G_{Rp} magnitudes (Evans et al., 2018). For bright sources ($G < 17$ mag) also medium-resolution ($\lambda/\Delta\lambda \sim 11500$) near-infrared (845 – 872 nm) spectra are taken, mainly to determine the radial velocity. Besides the 102 CCDs used for scientific observations, 4 CCDs are used for monitoring and operating *Gaia*.

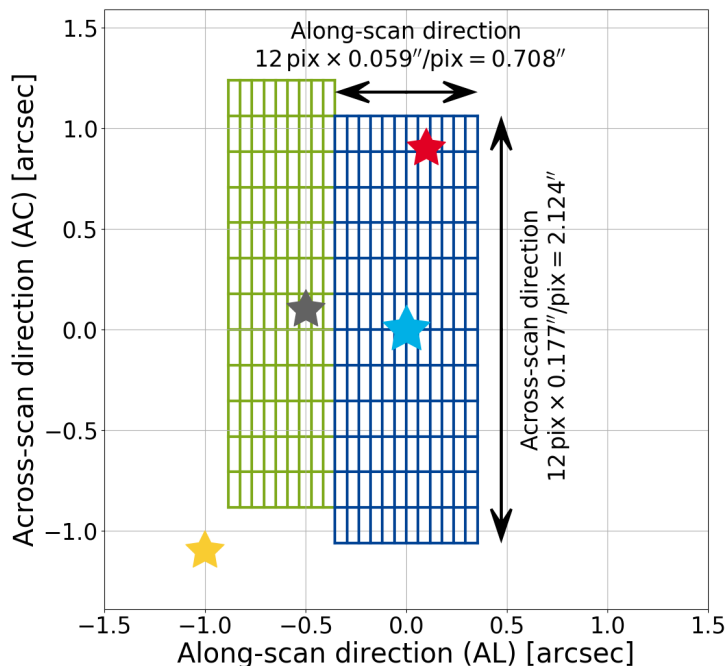


FIGURE 3.4: Illustration of the readout windows. For the brightest source (blue big star) *Gaia* assigns the full window (blue grid) of 12×12 pixels. For a second source close by but outside of the readout window (e.g. grey star) *Gaia* assigns a truncated readout window (green grid). A second source within the readout window (e.g. red star) might only be detected by a deeper analysis. For more distant sources (e.g. yellow star) *Gaia* assigns a full window (adopted from Klüter et al., 2020, Figure. 2).

3.1.3 Readout windows

Gaia's capabilities are limited by its downlink to Earth. Hence, an onboard reduction of the volume of data is indispensable. For that purpose, sources with a G magnitude (G) brighter than $G = 21$ are detected onboard using the data of the two sky mappers. Only small “windows” around each detected source are then read out and transmitted to the ground. Apart from the reduction of the telemetry data flow, this method also strongly reduces the readout noise on the

¹⁰Image: *Gaia*'s focal plane: <https://www.cosmos.esa.int/web/gaia/focal-plane>, accessed on May 13th 2020.

CCDs. For faint sources ($G > 13$ mag) the size of the window is 12×12 pixels (along-scan \times across-scan, see Figure 3.4). This corresponds to $708 \text{ mas} \times 2124 \text{ mas}$, due to a 1:3 pixel-size ratio. For a further reduction of the volume of data and readout noise, the data are stacked along the across-scan direction, leading to a one-dimensional strip, which is then transmitted to Earth. Hence the measured image position is precise in along-scan direction only. For bright sources ($G < 13$ mag) larger windows of 18×12 pixel are read out. These data are transferred as 2D images (Carrasco, J. M. et al., 2016). The readout windows of two close-by sources may overlap, shown as an example by the blue and grey star in Figure 3.4. In most cases, only for one of the two sources, a full window is assigned by *Gaia*'s onboard processing. This is usually the brighter source. For the second source, *Gaia* assigns only a truncated window (green grid in Figure 3.4) if it is fainter than $G = 13$. A source within the readout window (red star) might only be detected using a non-single source treatment at a later stage of the data analysis. Consequently, the current resolution of *Gaia* is not limited by its full width at half maximum (FWHM) of 103 mas but the size of the readout windows.

3.1.4 Astrometric performance¹¹

Gaia's astrometric measurements are remarkably precise. Even with the second data release which is only based on the first two years of observations, the position of a source can be determined with an uncertainty below 0.1 mas for sources brighter than $G = 17$ and below 0.7 mas for sources brighter than $G = 20$ (Lindegren et al., 2018). The uncertainty for the proper motion and parallax are also exceptionally small, and will be further improved with the upcoming data releases. For most of the use cases of *Gaia*, for example the ‘‘Prediction of astrometric microlensing events’’ as described in Chapter 4, the end of mission uncertainties are important. Hence, published information about the precision and accuracy of *Gaia* mostly refers to the end-of-mission standard errors. These are shown in Table 3.1. The *Gaia* Collaboration provides an analytical formula to estimate this precision as a function depending on the G magnitude and $V - I_C$ colour (Gaia Collaboration et al., 2016b):

$$\sigma_w = \sqrt{-1.631 + 680.766 \cdot z + 32.732 \cdot z^2} \cdot (0.986 + (1 - 0986) \cdot (V - I_C)) \cdot 1\mu\text{as} \quad (3.1)$$

where

$$z = 10^{(0.4(\max(G, 12.09) - 15))}. \quad (3.2)$$

¹¹*Gaia* Science Performance: <https://www.cosmos.esa.int/web/gaia/science-performance>, accessed on May 13th 2020.

TABLE 3.1: End-of-(nominal)-mission sky average astrometric performance. The standard errors for the position (σ_0), proper motion (σ_μ) and parallax (σ_ϖ) are given for different G magnitudes (ESA¹²).

G	< 12	13	14	15	16	17	18	19	20
σ_0 [μas]	5.0	7.7	12.3	19.8	32.4	55.4	102	208	466
σ_μ [$\mu\text{as/yr}$]	3.5	5.4	8.7	14.0	22.9	39.2	72.3	147	330
σ_ϖ [μas]	6.7	10.3	16.5	26.6	43.6	74.5	137	280	627

However, for the "Expectations on the mass determination using astrometric microlensing by *Gaia*" presented in Chapter 5, the uncertainty of the individual measurements is important. These are shown in Figure 9 of [Lindegren et al. \(2018\)](#) (see also the insets in Figure 5.2). The red line in Figure 5.2 shows the formal precision in along-scan direction for one CCD measurement. The precision is mainly dominated by photon noise. Via an electronic reduction of the effective exposure time, the number of photons is roughly constant for sources brighter than $G = 12$ mag, with a precision down to 0.05 mas. For $G = 20$ the expected precision is about 5 mas. The blue line in Figure 5.2 shows the actual scatter of the post-fit residuals. The difference between the two curves represents the combination of all unmodeled errors ([Lindegren et al., 2018](#)). These are presently, i.e. for DR2, on the order of 0.2 mas. This is expected to be improved for upcoming data releases.

3.2 *Gaia* catalogues¹³

The results of the *Gaia* mission are published in several data releases by the *Gaia* Collaboration. The first data release ([Gaia Collaboration et al., 2016a](#), *Gaia* DR1) was published in summer 2016. It contains the position and G magnitude of 1.1 billion sources. Since *Gaia* DR1 was only based on the first year of observations (mid 2014 - mid 2015), the determination of the proper motion was only possible for about two million sources, using external information of the Tycho 2 and Hipparcos catalogues ([Lindegren et al., 2016](#)). *Gaia* DR1 also contains photometric data of selected variable stars from the first month of observation. During this period a slightly different scanning law was used, repeatedly observing the ecliptic poles ([Gaia Collaboration et al., 2016a](#)).

¹²Table: *Gaia*'s end-of-mission performance: <https://www.cosmos.esa.int/web/gaia/sp-table1>, accessed on May 13th 2020.

¹³*Gaia* Data Release Scenario: <https://www.cosmos.esa.int/web/gaia/release>, accessed on May 13th 2020.

3.2.1 *Gaia* DR2

The second and most recent data release was published on 25 April 2018 ([Gaia Collaboration et al., 2018](#)). It is based on roughly two years of observations (July 2014 - May 2015). Besides the position ($\phi = (\alpha, \delta)$) and G magnitude of 1.7 billion sources, it was also possible to determine the proper motion ($\mu = (\mu_{\alpha^*}, \mu_{\delta})$) and parallax (ϖ) of 1.3 billion sources independently from external data. For most of the sources (1.4 billion), *Gaia* DR2 also contains the integrated flux of the two photometers (G_{Bp} and G_{Rp}). Mean radial velocities were published for 7.2 million bright sources. Furthermore, *Gaia* DR2 contains multi epoch data for known solar system objects.

Additionally, the catalogue also contains temperatures, extinctions, stellar radii and luminosities from a deeper analysis ([Andrae et al., 2018](#)) for about 100 million source.

3.2.2 Upcoming data releases and data products

In the next years, further data releases will follow. Besides the longer baseline, additional data products will be included and the measurements will be analysed in more detail. An exception of this is the early data release 3 (*Gaia* eDR3). This is only a partial release of the third data release (*Gaia* DR3). *Gaia* eDR3 contains “only” the positions, parallaxes and proper motions as well as the G , G_{Bp} and G_{Rp} magnitudes.

In addition to improved results for the data products of the first two data releases, *Gaia* DR3 will also contain some astrometric orbital solutions for binary stars, object classifiers, spectra from the two photometers and from the radial velocity sensor. Furthermore, the epoch photometry for all variable sources will be published. Especially the orbital solutions may improve the studies presented in this thesis. Further, for *Gaia* DR1,2 and *Gaia* DR3 the truncated windows are not processed¹⁴. This will be included for *Gaia* DR4

With the fourth data release *Gaia* DR4 (expected in 2024), all individual *Gaia* measurements of the nominal 5-year mission will be published. The individual measurements of the extended mission will be published in the final data release, along with further improved parallaxes, proper motions etc. The data processing for *Gaia* DR1,2&3 considers one source per readout window. This will be improved in later data releases and thereby increasing the angular resolution.

¹⁴*Gaia* Data Release Documentation - Data model description
https://gea.esac.esa.int/archive/documentation/GDR2/Gaia_archive/chap_datamodel/sec_dm_main_tables/ssec_dm_gaia_source.html, accessed on May 13th 2020.

Chapter 4

Prediction of astrometric microlensing events from *Gaia* DR2

4.1 Introduction

The greatest advantage of astrometric microlensing is the opportunity to predict events with high confidence using stars with well-known proper motions (Paczynski, 1995). For that purpose, faint nearby stars with high proper motions are of particular interest. High proper motions are preferred because the covered sky area within a given time is larger, hence microlensing events are more likely. Nearby stars are preferred because their Einstein radius is larger and therefore the expected shift is larger as well. Finally, faint lenses are favourable since the measurement of the source position is less contaminated by the lens brightness.

The first systematic search for astrometric microlensing events was done by Salim and Gould (2000). They found 146 candidates between 2005 and 2015. Proft et al. (2011) predicted 1118 candidates between 2014-2019, using the best stellar proper motion catalogues available at the time. They also found large discrepancies between the different catalogues, which made confident predictions impossible. Only 43 of their events use reliable proper motions. Furthermore, due to missing parallax measurements, it is challenging to estimate the expected effect.

With the *Gaia* data these problems could be solved. Due to its outstanding accuracy, *Gaia* provides the ideal data sets for such studies. Based on *Gaia* DR1, McGill et al. (2018) predicted one event caused by a white dwarf in 2019. The currently most precise predictions are based on *Gaia* DR2. In (Klüter et al., 2018a,b), my co-authors and I published the prediction of two at that time ongoing astrometric microlensing events, as well as 3912 further events until mid-2065. At the same time, Bramich (2018) and Bramich and Nielsen (2018) published independently the

prediction of about 2600 events between 2014 and 2100. Naturally, our results partly overlap with their predictions. Several dozen events were also found by combining *Gaia* DR2 with external catalogues (e.g. [Nielsen and Bramich, 2018](#); [McGill et al., 2019a](#)).

Some of the events may also produce a photometric signal. However it is not possible to predict these events with high confidence due to the uncertainty of the measured proper motion. [Mustill et al. \(2018b\)](#) searched explicitly for photometric events and found 30 events with a probability for entering the Einstein radius larger than 10 % until 2032.

In the following, our method and the results on the prediction of astrometric microlensing, published in [Klüter et al. \(2018a,b\)](#) are presented.

The basic idea to find candidates for astrometric microlensing only slightly varies between the different publication. Our method consists of four steps: 1) Determine a list of high-proper-motion stars (HPMS) as potential lenses in Section 4.2. 2) Find background sources close to their paths on the sky in Section 4.3. 3) Forecast the exact positions of source and lens stars based on their current positions, proper motions and parallaxes as well as determine the angular separation and epoch of the closest approach 4.4. 4) Calculate the expected microlensing effects, that is, the shift of the background star position, based on an approximated mass in Section 4.5. The last step was only made possible due to the precise parallaxes from *Gaia* DR2.

4.2 List of high-proper-motion stars

In our work, we focused on high-proper-motion stars with a total proper motion $\mu = \sqrt{\mu_{\alpha^*}^2 + \mu_{\delta}^2}$ larger than 150 mas/yr. About 170 000 sources in *Gaia* DR2 fulfill this criterion. As the *Gaia* Consortium has mentioned ([Lindegren et al., 2018](#)), DR2 contains a small proportion of erroneous astrometric solutions, most noticeably a set of unrealistically high proper motions or parallaxes. Hence a clean-up of our list of potential lenses was necessary. For that purpose, we defined a set of quality cuts, listed in Table 4.1. Firstly, we selected only sources with a highly significant parallax ($\varpi > 8\sigma_{\varpi}$). This also ensures a good quality of the other astrometric parameters, which is needed to confidently forecast the path of the lens. Figure 4.1 shows the absolute values of the proper motions and the parallaxes of the remaining high-proper-motion stars. Four different populations are clearly visible. The two lower ones are interpreted as the real populations of halo stars with a typical tangential velocity of $v_{tan} \approx 350$ km/s (green line), and old stars ($v_{tan} \approx 75$ km/s, blue line), whereas the two upper populations (red lines) are incorrect data, since such stars do not exist, at least not in such numbers and at distances of 10 pc or smaller. It

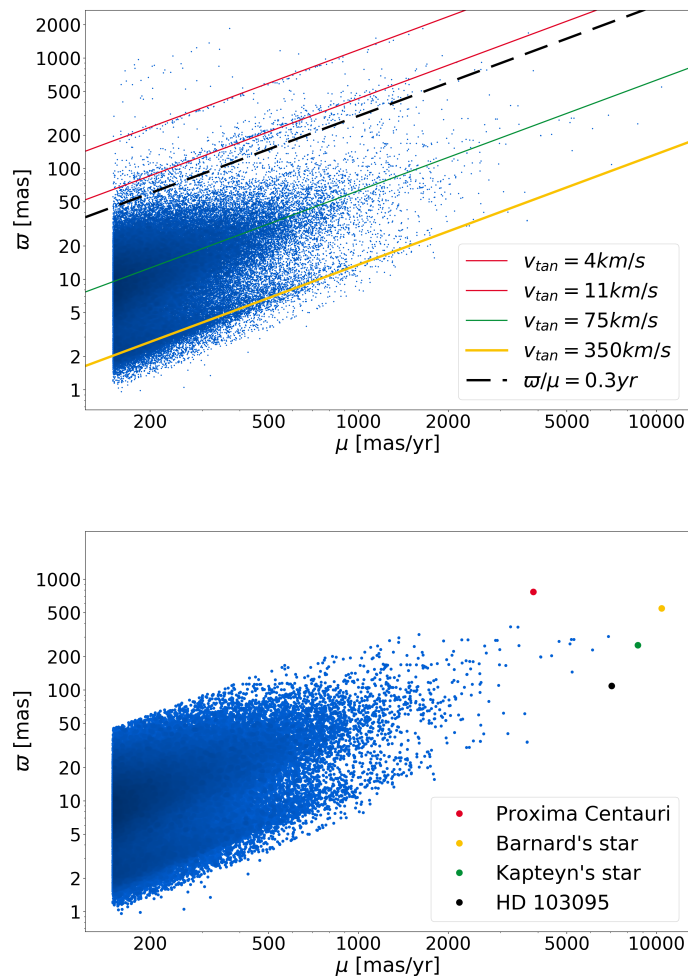


FIGURE 4.1: Proper motions (μ) vs parallaxes (ϖ) of the high-proper-motion stars. Top: all sources with significant parallaxes. The yellow line indicates the population of halo stars and the green line indicates the population of old stars. The red lines indicate two sharp populations of obviously erroneous objects. Bottom: the cleaned sample. The isolated points with very high proper motion correspond to real stars, for example Proxima Centauri (red), Barnard's star (yellow), Kapteyn's star (green), and HD 103095 (black) (adapted from Klüter et al., 2018b, Figure 3).

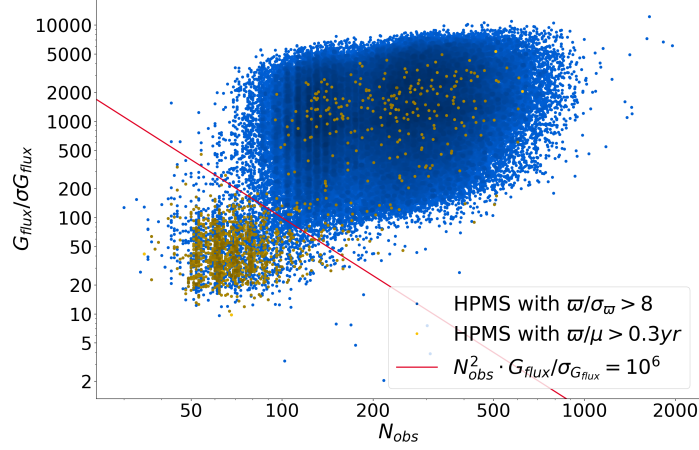


FIGURE 4.2: Number of photometric observations by *Gaia* (n_{obs}) and significance of the *G* flux ($G_{flux}/\sigma_{G_{flux}}$) for all high-proper-motions stars with significant parallaxes. The yellow dots indicate the sources with $\varpi/\mu > 0.3yr$. The red line indicates our used limit. The excluded lenses right above this limit are most likely real objects (adapted from Klüter et al., 2018b, Figure 4).

is not clear why the faulty *Gaia* DR2 data show such sharp relations between parallax and proper motions (private communication with the *Gaia* astrometry group). To exclude those faulty *Gaia* data, we neglected all stars with $\varpi/\mu > 0.3yr$. This limit is shown as dashed line in Figure 4.1. By a visual inspection of the various columns of *Gaia* DR2, we found that the suspicious data also cluster when the significance of the *Gaia* *G* flux ($G_{flux}/\sigma_{G_{flux}}$) is plotted versus the number of photometric observations by *Gaia* (n_{obs}) (see Figure 4.2). We therefore excluded all sources with $n_{obs}^2 \cdot G_{flux}/\sigma_{G_{flux}} < 10^6$ (i.e below-left of the red line in Figure 4.2).

The final list of potential lenses contains about 148 000 high-proper-motion stars. As expected, these nearby objects are quite evenly distributed over the sky (see Figure 4.3, top panel), with a small under-density towards the solar apex ($3h48'$, $+22^\circ32'$) and antapex ($16h12'$, $-22^\circ32'$). The rejected objects, on the other hand, mainly cluster towards dense areas either in the galactic disc and bulge or towards the Magellanic Clouds (see Figure 4.3, bottom panel).

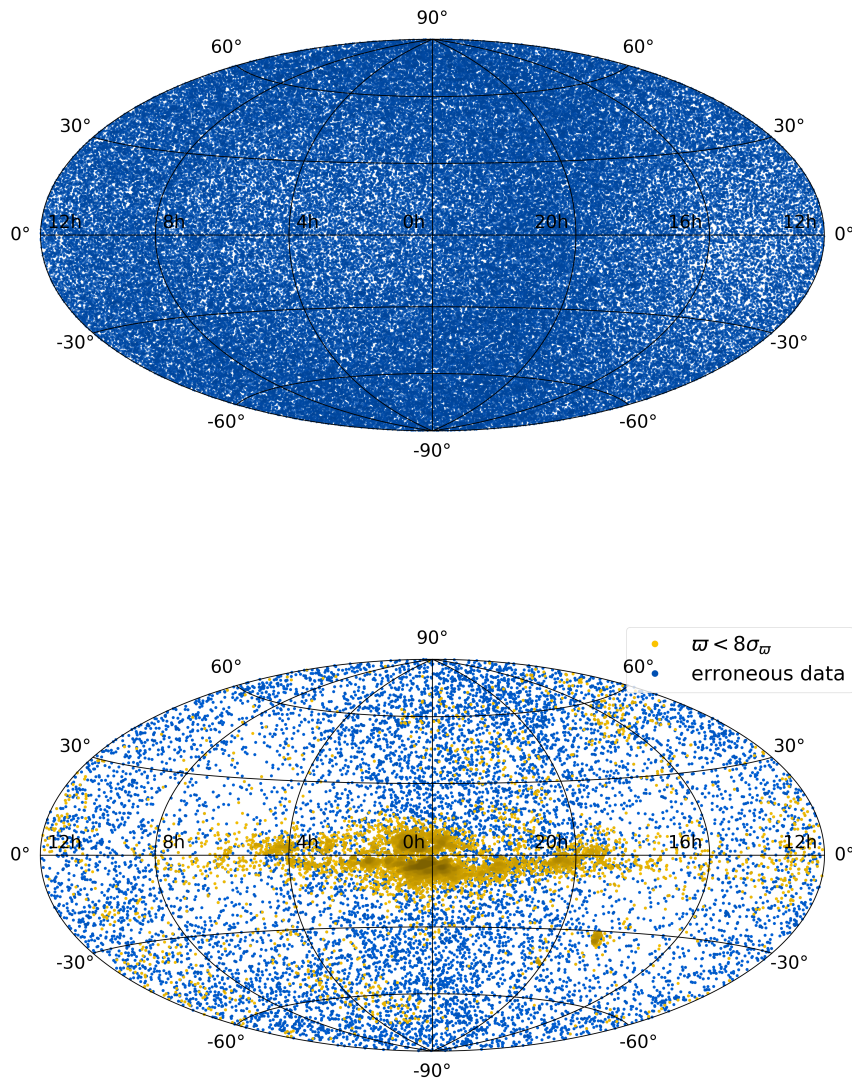


FIGURE 4.3: Top: Aitoff projection all-sky map for the high-proper-motion stars with $\mu > 150$ mas/yr. The small under-densities around $(4h, 0^\circ)$ and $(16h, 0^\circ)$ are caused by the solar apex and antapex. Bottom: All excluded objects. The blue dots show the sources with non-significant parallaxes, the yellow dots indicate the erroneous data, according to the red line in Figure 4.2 (adapted from Klüter et al., 2018b, Figure 2).

4.3 Background stars

We then searched for background sources close to the paths of the remaining $\sim 148\,000$ high-proper-motion stars. For this, we defined a box by using the position of the source at the epochs J2010.0 and J2065.5 with a half-width $w = 7''$ perpendicular to the direction of the proper motion (see Figure 4.4). The large box width is mainly adopted to account for potential motions of background sources. A widening shape would be more physically appropriate, however, for simplicity we used the rectangular shape. We thereby found about 226 000 distinct pairs. Throughout the rest of this chapter, each such pair, i.e. the combination of a high-proper-motion foreground lens and a background source is called a “candidate”. The source parameters are labelled with the prefix “Sou_”.

In order to avoid suspicious sources, we also included four quality cuts for the sources. We removed sources with a significantly negative parallax ($\text{Sou}_\varpi < -3 \cdot \text{Sou}_\sigma_\varpi - 0.029$ mas). The offset of -0.029 mas is used to correct for the zero-point of *Gaia*’s parallaxes, determined from a sample of known quasars (Lindgren et al., 2018). We then required a standard error in the J2015.5 position below 10 mas ($\sqrt{\text{Sou}_\sigma_{\alpha^*}^2 + \text{Sou}_\sigma_\delta^2} < 10$ mas).

For sources with non-significant negative parallaxes (-0.029 mas $>$ $\text{Sou}_\varpi + 3 \cdot \text{Sou}_\sigma_\varpi$) or without parallax in *Gaia* DR2, we assumed a value of $\text{Sou}_\varpi = -0.029$ mas again for correcting the zero-point of *Gaia*’s parallaxes.

About 25% of our potential background sources, have no measured parallax and proper motion listed in *Gaia* DR2. In order to compensate for the unknown proper motion and parallax, we assumed a standard error of $\text{Sou}_\sigma_{\mu_{\alpha^*,\delta}} = 10$ mas/yr, $\text{Sou}_\sigma_\varpi = 2$ mas, respectively. Roughly 90% of the background sources with a 5-parameter solution have proper-motions and parallaxes below this value.

To avoid binary stars and co-moving stars in our candidate list, we excluded pairs with common proper motion, that is,

$$|\boldsymbol{\mu} - \text{Sou}_\boldsymbol{\mu}| < 0.7 \cdot |\boldsymbol{\mu}|. \quad (4.1)$$

These criteria can only be used if the proper motion of the source is given in *Gaia* DR2. Hence, events without a given proper motion of the source have to be treated carefully, especially when the estimated date of the closest approach is close to the *Gaia* reference epoch J2015.5. Nevertheless, most of them are expected to be real events.

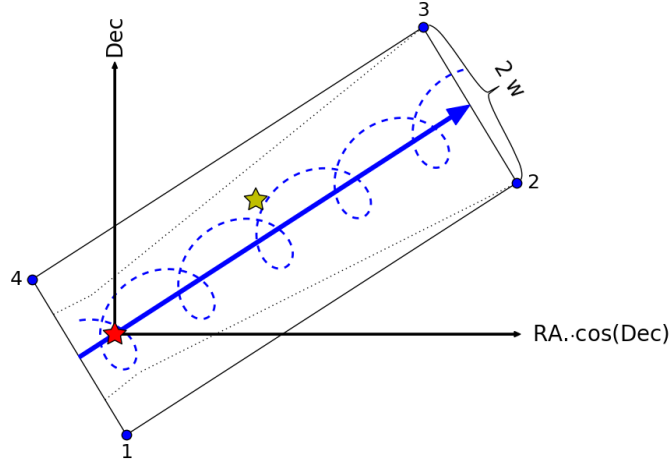


FIGURE 4.4: Illustration of the sky window used in the search for background stars. The thick solid blue line indicates the proper motion of the lens (red star), and the origin is set to the J2015.5 position of the lens. The blue dashed line indicates the real motion, which includes the parallax. When a background star (yellow star) is within the black box, it is considered as a candidate. The box is defined by the position of the lens in J2010.0 and J2065.5 and a half-width of $7''$ (Here only 5 years are shown and the). To account for the proper motion of the background source, the widening shape (dotted black line) would be more physically appropriate (adapted from Klüter et al., 2018b, Figure 5).

Finally, we excluded candidates where the parallax of the source is larger than the parallax of the lens ($\text{Sou}_\varpi > \varpi$), to avoid imaginary Einstein radii. An astrometric microlensing event caused by a high-proper-motion star passing behind a foreground star would be interesting. For the few cases, it turned out that no measurable effect is expected when the role of lens and source is swapped. Stronger cuts on the parallax are not necessary since comparable parallaxes will lead to small Einstein radii and hence to small astrometric shifts.

4.4 Position forecast and determination of the closest approach

Roughly 68 000 candidates fulfill all criteria. For those, we estimated the closest approach by forecasting the positions of source and lens from *Gaia* DR2's positions, proper motions, and parallaxes. Since we are interested in the global minima, and since the periodic motion of the

Earth may cause many local minima, we first neglected the Earth's motion and calculated an approximate separation and epoch of the closest approach by using a nested-intervals algorithm. Whenever the expected shift according to Equation (2.21) for the approximate separation was larger than 0.03 mas, the exact value was calculated by including the parallax.

In order to account for the multiple minima, we evaluated the separation as function of time within ± 1 year around the approximate epoch using intervals of roughly four weeks. Around all detected minima, we determined the exact minimum separations ($\Delta\phi_{min}$) and the epoch of the closest approaches (T_{CA}), again using the nested-intervals algorithm. By comparing these values we selected the global minima. Depending on the parallax, and proper motion, the epoch of the global minimum differs by up to 0.5 years from the approximated epoch.

Gaia is located at the Lagrange point L2, as will be the future James Web Space Telescope (JWST). L2 will also be the favourable location for other future space telescopes. Since the heliocentric orbit at L2 is roughly 1% larger than for the Earth, a slightly different impact parameter can be observed. In order to take this into account we repeated this analysis using a 1% larger parallax. As expected, the effects only differ when the smallest separation is small compared to the parallax, but for a few events the difference might be measurable.

4.5 Approximate mass and Einstein radius

In order to determine a realistic value for the expected astrometric shifts of our candidates, a realistic mass has to be assumed. Using the *Gaia* photometry, we determined a mass as follows:

First, we divided our candidates into three categories — white dwarfs (WD), main-sequence stars (MS), and red giants (RG) — by using the following cuts in colour-magnitude space, as shown in Figure 4.5:

$$\begin{aligned} WD : \quad G_{BP,abs} &\geq 4 \cdot (G - G_{RP})^2 + 4.5 \cdot (G - G_{RP}) + 6, \\ RG : \quad G_{BP,abs} &\leq -3 \cdot (G - G_{RP})^2 + 8 \cdot (G - G_{RP}) - 1.3. \end{aligned} \tag{4.2}$$

Here, $G_{BP,abs}$ represents the absolute magnitude determined via the distance modulus using the measured parallax. Lenses without G_{BP} and G_{RP} magnitudes were assumed to be main-sequence stars.

For white dwarfs and red giants, we used typical masses of $M_{WD} = (0.65 \pm 0.15) M_{\odot}$ and $M_{RG} = (1.0 \pm 0.5 M_{\odot})$, respectively, where the indicated uncertainties are used for the error calculus. For the main-sequence stars, we determined a relation between G magnitudes and

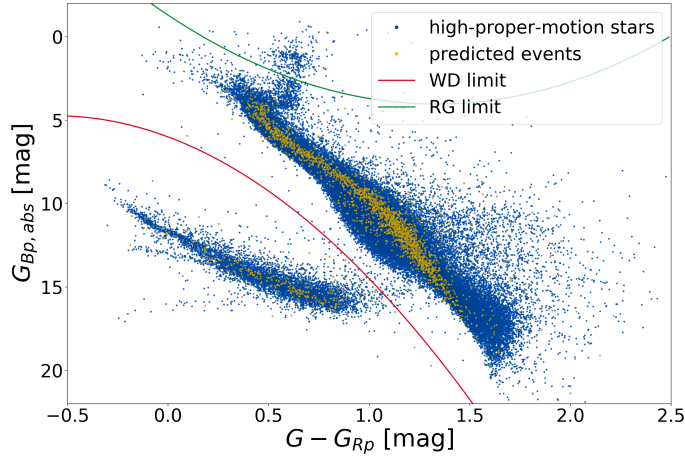


FIGURE 4.5: Colour-absolute magnitude diagram of all potential lenses (blue dots) with full *Gaia* DR2 photometry G , G_{Rp} , and G_{Bp} . The yellow dots indicate the lenses of the predicted events. All stars above the green line are considered as red giants and all sources below the red line as white dwarfs (adapted from Klüter et al., 2018b, Figure 6).

stellar masses. We started with a list of temperatures, stellar radii, absolute V magnitudes, and $V - I_C$ colours for different stellar types on the main sequence (Pecaut and Mamajek, 2013). We then translated these relations into the *Gaia* filter system using the colour relation from Jordi et al. (2010),

$$G - V = -0.0257 - 0.0924(V - I_C) - 0.1623(V - I_C)^2 + 0.0090(V - I_C)^3. \quad (4.3)$$

For the different stellar types, we calculated the stellar masses using the luminosity equation

$$\frac{L}{L_\odot} = \left(\frac{R}{R_\odot}\right)^2 \left(\frac{T}{T_\odot}\right)^4, \quad (4.4)$$

and the mass-luminosity relations (Salaris and Cassisi, 2005):

$$\begin{aligned} \text{for } L < 0.0304 : \frac{L}{L_\odot} &= 0.23 \left(\frac{M}{M_\odot}\right)^{2.3}, \\ \text{for } L > 0.0304 : \frac{L}{L_\odot} &= \left(\frac{M}{M_\odot}\right)^4. \end{aligned} \quad (4.5)$$

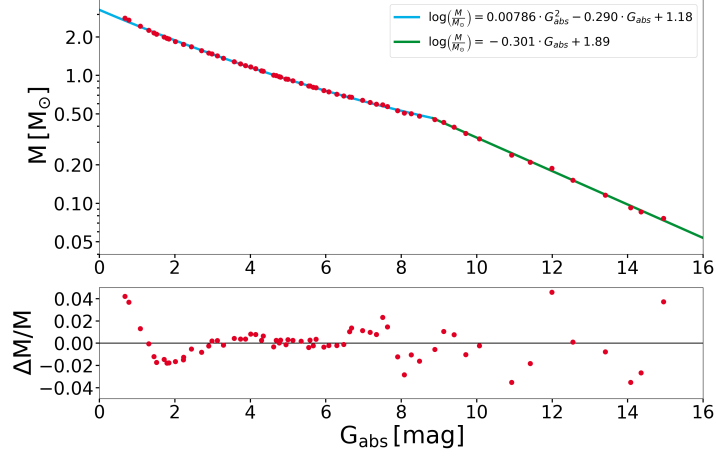


FIGURE 4.6: Determined $G_{abs} - M$ relation. The red points show the derived masses for different stellar types on the main sequence. The blue ($G_{abs} < 8.85$) and green ($G_{abs} > 8.85$) lines show the fitted relations. The two slopes are caused by the different luminosity-mass relations. In the bottom panel, the relative residuals after the fit are shown, which are typically below 2% (adapted from Klüter et al., 2018b, Figure 7).

Finally, we fitted two exponential functions to the data and obtained the equations:

for $G_{abs} < 8.85$:

$$\log\left(\frac{M}{M_{\odot}}\right) = 0.00786 G_{abs}^2 - 0.290 G_{abs} + 1.18, \quad (4.6)$$

for $8.85 < G_{abs} < 15$:

$$\log\left(\frac{M}{M_{\odot}}\right) = -0.301 G_{abs} + 1.89.$$

Figure 4.6 shows the fitted relation and its residuals. The relative residuals in the interesting regime ($\sim 2 < G_{abs} < \sim 15$) are below 2%, which is amply sufficient for the present purpose. However, in the error calculus, we considered a mean error of 10% to account also for the uncertainties in G magnitude, parallax, in the equations used and in the dependence on metallicity. We did not use a relation based on *Gaia* colours, for two reasons: first, some of our lenses do not have colour information in DR2, and second, our sample contains many metal-poor halo stars. Hence they appear much bluer, whereas the change in absolute magnitude is rather small. For

$G_{abs} > 15.0$ (i.e. $M < \sim 0.07 M_{\odot}$) we reach the area of brown dwarfs. Those stars cannot be described by a mass-luminosity relation. Instead, we chose a fixed mass of $(0.07 \pm 0.03) M_{\odot}$. The calculated masses are only rough estimates in order to get an expectation of the Einstein radii, astrometric shifts, and magnifications of the predicted microlensing events. An exact and direct determination of their masses would not be a prerequisite, but rather the goal when observing these events.

Using the estimated masses M_L and the *Gaia* DR2 parallaxes ϖ and $\text{Sou_}\varpi$, we calculated the Einstein radii via Equation (2.4). Furthermore, we computed the impact parameter in units of the Einstein radius (u), and determined the expected shifts for the major image ($\delta\theta_+$), the centre of light ($\delta\theta_c$) and for the centre of light assuming luminous-lens effects ($\delta\theta_{c,lum}$) using Equations (2.5), (2.16), (2.18) and (2.19). We also determined the expected magnification of the combined light of lens and source (δm_{lum}) using Equation (2.12). Finally, we only selected those candidates where $\delta\theta_+ > 0.1$ mas.

TABLE 4.1: Quality cuts for the prediction of microlensing events applied to the raw target list of high-proper-motion stars, background sources, and events. These quantities are based on the position (ra , dec), the total proper motion (μ), the parallax (ϖ), the number of photometric observations in G (n_{obs}) by *Gaia*, the G flux (G_{flux}), the corresponding errors ($\sigma_{...}$) as well as the expected shift of the major image ($\delta\theta_+$). Parameters from the background source are indicated with a Sou_ prefix.

application	criteria
Lenses	$\mu > 150$ mas/yr
Lenses	$\varpi/\sigma_{\varpi} > 8$
Lenses	$\varpi/\mu < 0.3$ yr
Lenses	$n_{obs}^2 \cdot G_{flux}/\sigma_{G_{flux}} > 10^6$
Sources	$(\text{Sou_}\varpi + 0.029 \text{ mas})/\text{Sou_}\sigma_{\varpi} > -3$
Sources	$\sqrt{\text{Sou_}\sigma_{\alpha^*}^2 + \text{Sou_}\sigma_{\delta}^2} < 10$ mas
Sources	$ \mu - \text{Sou_}\mu < 0.7 \cdot \mu $
Sources	$\text{Sou_}\varpi < \varpi$
Events	$\delta\theta_+ > 0.1$ mas

4.6 Results

Using the method described above, we predicted 3914 microlensing events between J2010.0 and J2065.5. These are caused by 2875 different lenses. Their locations on the sky are shown in

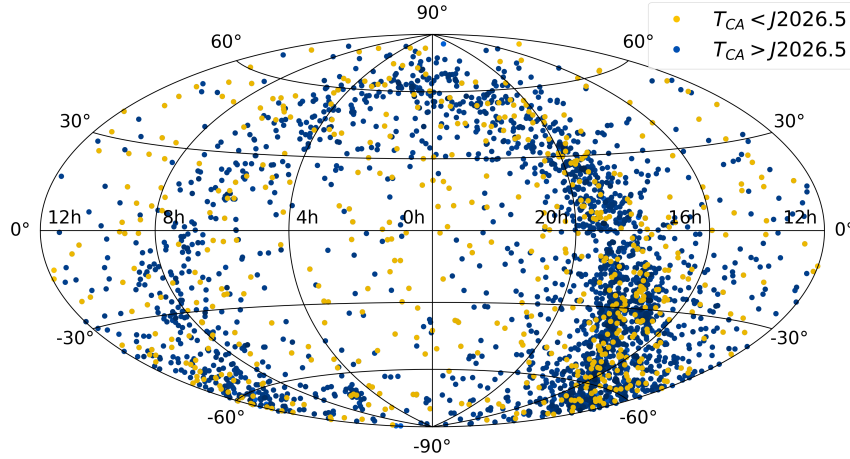


FIGURE 4.7: Aitoff projection in equatorial coordinates of the events before J2026.5 (yellow) and after J2026.5 (blue). Most of the events are in the galactic plane (adapted from Klüter et al., 2018b, Figure 8).

Figure 4.7. As expected, the events are mainly located towards the galactic plane or the Large Magellanic Cloud. Table A.1 lists the results of a few interesting events. The full catalogue of microlensing events can be accessed through the GAVO Data Center¹⁵.

In the following, “shift” refers to the astrometric displacement of the major image only ($\delta\theta_+$) and “shift of the centre of light” refers to the combined centre of light ($\delta\theta_{c,lum}$) considering luminous-lens effects.

***G* magnitudes**

Typically, the lens is much brighter in the *G* magnitudes than the source. Only for 210 events, this is not the case. The lenses of these events are usually white or brown dwarfs. For 726 events, the source is less than three magnitudes fainter than the lens, while for 1050 events, the brightness difference is between three and six magnitudes. For roughly half of the events (1928), the magnitude difference in *G* is larger than six magnitudes. The high fraction is caused

¹⁵German Astrophysical Virtual Observatory,
<http://dc.zah.uni-heidelberg.de/amlensing/q2/q/form>

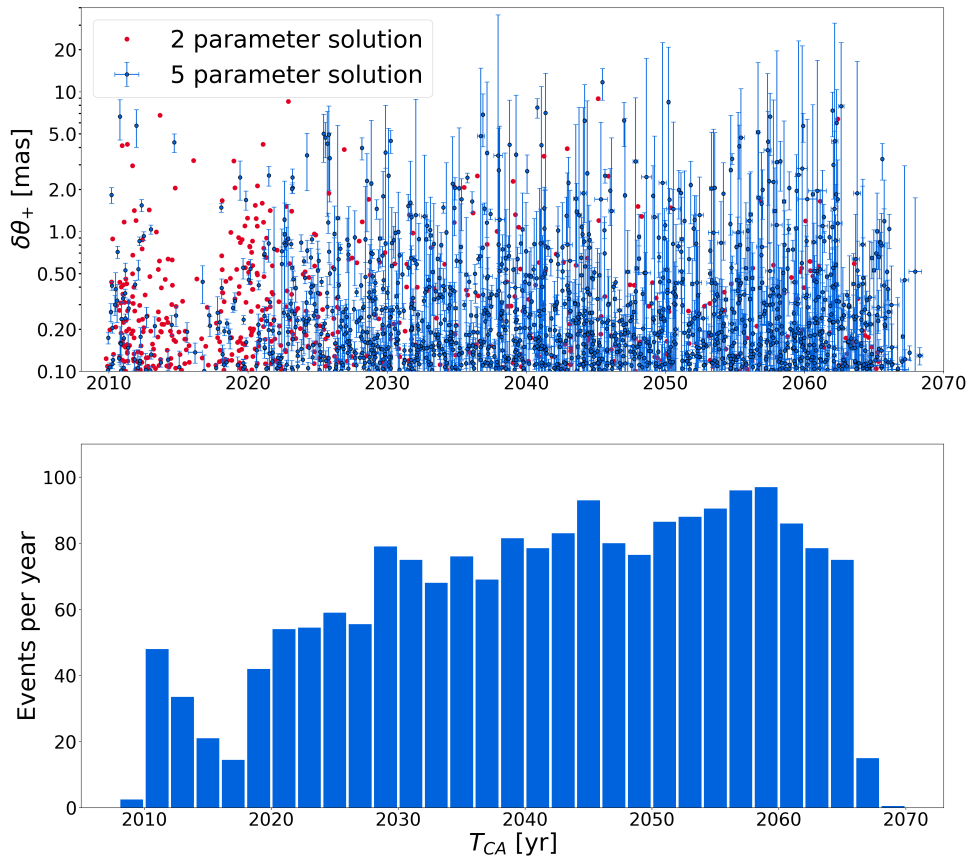


FIGURE 4.8: Temporal distribution of the predicted events. Top: Expected maximum shifts ($\delta\theta_+$) for all events with a source less than six magnitudes fainter than the lens. The red dots indicate the events where the proper motions and parallaxes of the sources are unknown. The blue dots show the events with five-parameter solutions for the background sources, as well as the determined standard errors ($\sigma_{\delta\theta_+}$ and $\sigma_{T_{CA}}$). Typically, the uncertainties for the predicted dates are smaller than the size of the dots (adapted from Klüter et al., 2018b, Figure 9).

Bottom: Number of events per year (including events with $\Delta G > 6$ mag). The apparent lack of events during the *Gaia* mission time is due to the angular resolution limit of *Gaia* DR2. The slight increase of between 2030 and 2060 is due to multiple events caused by a lens. The events before 2010 and after 2065.5 are due to the proper-motion of the source.

by the fact that bright sources typically have large Einstein radii. They are either close-by or more luminous and therefore more massive. Hence, a measurable deflection is also expected at separations of a few mas. This allows measurements using coronagraphs. [Zurlo et al. \(2018\)](#) has demonstrated that such high-contrast measurements are possible. Aside from that, it is possible to reduce the difference in brightness by using different filters. In the following section, the given numbers refer to the sample of $210 + 726 + 1050 = 1986$ events with a magnitude difference below 6 mag.

Expected shifts

The top panel of Figure 4.8 shows the date of the closest approach and the expected astrometric shift. The number of events per year is shown in the bottom panel. Between 2012 and 2021 the number of events (20-40 events per year) is much lower than the average of 70 events per year. This is caused by the limited angular resolution of the underlying star catalogue. For *Gaia* DR2 it is about 400 mas. Furthermore, the number of events slightly increases with time, which is caused by lenses passing several background stars. The few events before or after our time-range from 2010 to 2065.5 are due to the proper motion of the background source.

Most of the events have a shift below 0.5 mas, but with modern instruments it is possible to measure such small variations. For 431, 201, and 54 events, we expect a shift of the brightest image larger than 0.5 mas, 1 mas, and 3 mas, respectively. Among these, 88, 18 and two, have a minimum separation larger than 100 mas. In total, 679 of the events have a smallest separation below 100 mas. Hence, luminous-lens effects should be considered for these events. Among the 679 events, 198, 44, and 18 events have an expected shift of the centre of light larger than 0.1 mas, 0.5 mas and 1 mas, respectively. We note that the luminosity effects depend on the used filters, and modern telescopes with adaptive optics or interferometry can even resolve separations smaller than 100 mas.

Events during the *Gaia* mission

Since *Gaia* obtains many precise measurements over its mission time (from J2014.5 up to possibly J2024.5), events during this time are of special interest. During a slightly extended period of time (2026.5; to accommodate events starting during the late *Gaia* mission), we found 544 events with an astrometric shift above 0.1 mas. Only 245 events have proper motions and parallaxes of the sources listed in *Gaia* DR2, but very probably will obtain motions and parallaxes in future *Gaia* data releases. The numbers for those events will be given in parentheses. Of

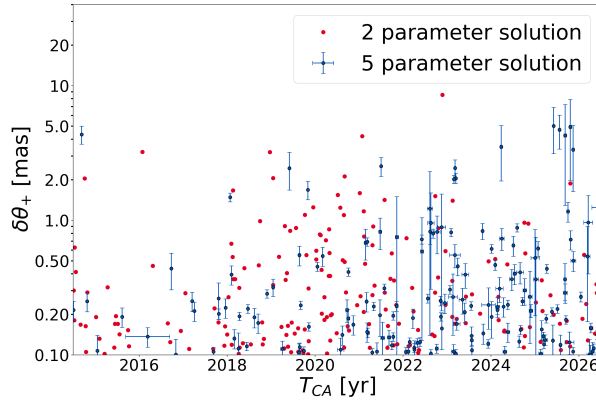


FIGURE 4.9: Maximum shifts for all expected events between 2014.5 and 2026.5, with (blue) and without (red) a five-parameter solution for the background source in *Gaia* DR2 (adapted from Klüter et al., 2018b, Figure 11).

the events during the *Gaia* era, 147 (62) have a minimum separation below 100 mas and will be (or were) blended for *Gaia* during the closest approach in the along-scan direction. In the across-scan direction they will be blended for a more extended time interval. For 44 (19) events the shift of the blended centre of light is larger than 0.1 mas. For 29 (19) events we expect also a measurable magnification above 1 mmag. The epoch and the astrometric shifts for our predicted events during the *Gaia* mission are shown in Figure 4.9. Since the expected timescales are on the order of a few years, it might be possible that *Gaia* observes the beginning or end of an event with a closest approach before 2014.5 or after 2024.5. Whether it is possible for *Gaia* to measure the astrometric shift for these events is part of the study presented in the chapter below.

Events caused by white dwarfs

Our catalogue contains 486 events caused by 352 different white dwarfs. For 427 of those, the background source is less than six magnitudes fainter in the *G* magnitudes. Since white dwarfs are blue objects, using infrared filters will be more advantageous for possible follow-up observations. Of these events, 84 will happen between 2014.5 and 2026.5. For 98 of the events, the expected maximum shift is above 0.5 mas and for 53 above 1 mas (17 and 5 for the period 2014.5-2026.5). For 22 events also the blended centre of light will be shifted by more than 0.5 mas.

4.6.1 Proxima Centauri - the nearest

[Sahu et al. \(2014\)](#) predicted two microlensing events of Proxima Centauri in October 2014 and February 2016 with a closest separation of 1600 mas and 500 mas, respectively. By observing those events with VLT, equipped with the SPHERE instrument, and with HST, equipped with the WFC3, [Zurlo et al. \(2018\)](#) were able to determine the mass of Proxima Centauri, but with an uncertainty of about 40%. We did not recover either of those two events, since the background stars are not listed in *Gaia* DR2. However, we found 84 further microlensing events of Proxima Centauri until J2065.5. Nine of those have an expected shift larger than 1 mas. With a G magnitude of 8.9 mag, Proxima Centauri is much brighter than the sources ($\Delta m \sim 6 - 12$ mag). Therefore a significant shift of the centre of light of the blended system cannot be observed. Due to the large Einstein radius of Proxima Centauri ($\Theta_E \simeq 27.1$ mas), a shift of 1 mas can still be observed at a separation of ~ 700 mas and for all sources with a separation smaller than 7000 mas a shift larger than 0.1 mas is expected. At this separation it is possible to observe background stars next to Proxima Centauri (see e.g. [Zurlo et al., 2018](#); [Gratton et al., 2020](#))

4.6.2 Barnard's star - the fastest

Barnard's star is the fastest star on the sky. Hence, the sky area passed by this star is the largest in our sample. Between J2010.0 and J2065.5 we found 37 astrometric microlensing events for Barnard's star. Seven of those happen between 2014.5 and 2026.5, and so *Gaia* might measure the deflections. Barnard's star has a G magnitude of 8.2 mag, and we determined an Einstein radius of ~ 28.6 mas. Due to its brightness, most of the sources are more than six magnitudes fainter. However, in 2035 it will pass by a $G = 11.8$ mag star with a closest separation of (335 ± 13) mas. If it is possible to resolve source and lens, a shift of (2.43 ± 0.20) mas is expected. The shift of the blended centre of light will be smaller than 0.1 mas. This event is listed in Table A.1 as event #11.

4.6.3 Two microlensing events in 2018

In [Klüter et al. \(2018a\)](#) we reported two "Ongoing astrometric microlensing events of two nearby stars" in summer 2018 by the high-proper-motion stars Luyten 143-23 and Ross 322. The expected maximum shifts are 1.74 ± 0.12 mas and 0.76 ± 0.06 mas, respectively.

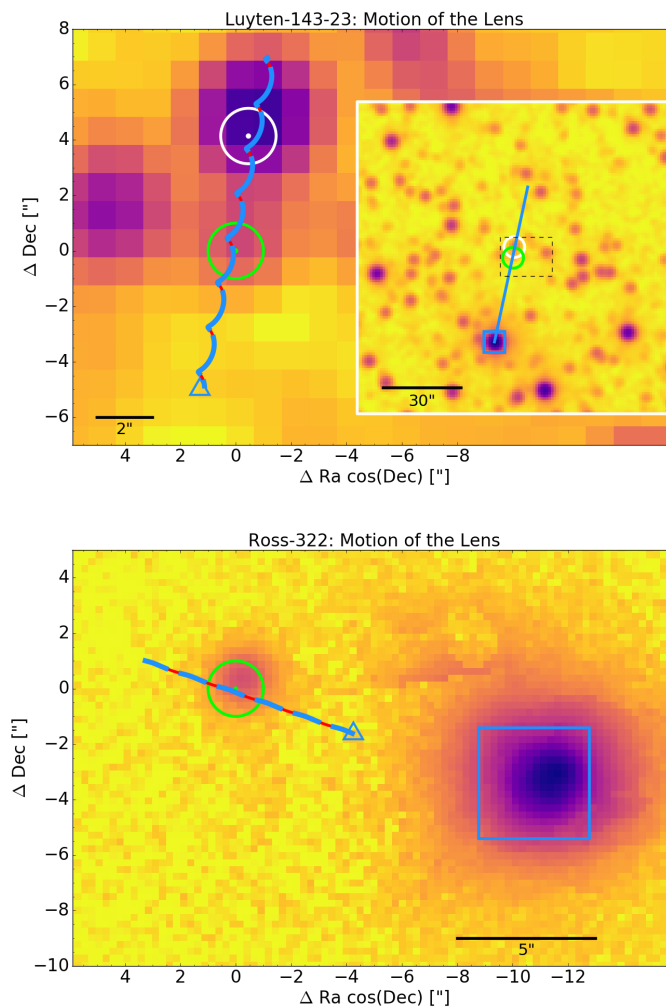


FIGURE 4.10: The top panel shows a 2MASS image with the two background stars that Luyten 143-23 passes by in July 2018 (green circle) and in March 2021 (white circle), respectively. A larger view of the sky area is displayed in the inset. The blue lines in the insets show the motion of the lens stars until 2035. The bottom panel shows a Pan-STARRS image with the background star which Ross 322 passes by in August 2018 (green circle). The exact positions of the background sources are indicated with small dots at the centres of the circles. Their motions and the uncertainties are smaller than the size of the dots. The triangles indicate the J2015.5 positions of the lens stars measured by *Gaia*. The predicted motions are shown as thick blue/thin red curves, where the thin red parts indicate the epochs at which the stars cannot be observed. In both panels, the original positions (at earlier epochs) of the lens stars in the 2MASS and Pan-STARRS images are indicated as squares (adapted from Klüter et al., 2018a, Figure 1).

Luyten 143-23

Luyten 143-23 is an M dwarf (M4V) with a parallax of 206.8 mas and an absolute proper motion of 1647.2 mas/yr. Its apparent G magnitude is 11.9 mag. By using our G_{abs} – mass relation (Equation (4.6)) we determined an approximate mass of $0.12 M_{\odot}$. We found that it passed a $G = 18.5$ mag star with a closest approach on July 7, 2018 and a smallest separation of 108.53 mas. (see Table A.1, event #1).

The top panel of Figure 4.10 shows a 2MASS (Two Micron All Sky Survey) (Skrutskie et al., 2006) image of Luyten 143-23. Its position at the epoch of the 2MASS observation is given as blue square in the inlay, and for the epoch J2015.5 as blue triangle. The predicted path of Luyten 143-23 is shown as a thick blue/thin red line, where the red parts indicate the times at which Luyten 143-23 is not observable. The observable periods are only a rough estimate, since they depend on the location of the observatory and the capability of the instruments. The positional background source is marked with a green circle.

Due to the large Einstein radius of $\theta_E = 14.0$ mas caused by the small distance of Luyten 143-23, a maximum shift of (1.74 ± 0.12) mas was expected. The unlensed motion of the background star as well as the predicted path due to lensing are shown in the top panel of Figure 4.11. Due to the high proper motion of Luyten 143-23, a rapid change of the astrometric shift between June and September 2018 (1.3 mas in 3 months) was expected. Unfortunately, Luyten 143-23 was not observable in August/September 2018 from the ground or by *Gaia*. For December 2018 we expected a shift of 0.4 mas, which should still be measurable. (see Chapter 6)

We found another close encounter of Luyten 143-23 with a $G = 17.0$ mag star to occur in 2021. The smallest separation of (280.1 ± 1.1) mas is reached on March 9, 2021; we expect a maximum shift of (0.69 ± 0.05) mas. This background star is marked with a white circle in Figure 4.10. Its expected motion is shown in the middle panel of Figure 4.11. (see Table A.1, event #5).

Ross 322

Ross 322 is an M dwarf (M2V) with a parallax of 42.5 mas. Its absolute proper motion is 1455.2 mas/yr. We determined an approximate mass of $0.28 M_{\odot}$. In 2018, Ross 322 passed by a $G = 18.6$ mag star with a closest approach on August 8, with a separation of (125.3 ± 3.4) mas.

Since the Einstein radius of Ross 322 is smaller than that of Luyten 143-23, the expected shift is only (0.76 ± 0.06) mas. The important parameters of this events are given in Table A.1, event # and the same plots as for Luyten 143-23 are given in the bottom panels of Figures 4.10

and 4.11, superposed on a Pan-STARRS (Panoramic Survey Telescope And Rapid Response System) image (Chambers and Pan-STARRS Team, 2018). The event was also predicted in Proft et al. (2011), but their predicted date was one year earlier ($T_{CA} = J2017.46$), and their determined minimum separation was three times as large 485mas.

4.6.4 Photometric microlensing effects of our astrometric microlensing events.

Using *Gaia* DR2, Mustill et al. (2018a) reported 30 possible photometric microlensing events in the next 20 years (J2015.5 to J2035.5). Twenty-four of their candidates are also listed in our sample, the other six have an absolute proper motion below 150 mas/yr. We found 246 events in the same time range with a magnification greater than $A_{lum} - 1 > 10^{-7}$, which is the lowest magnification of their candidates. The typical photometric precision of photometric microlensing surveys is on the order of a few milli-magnitudes (Udalski et al., 2015). Hence, we assume a limit of 1 mmag to talk about photometric microlensing events. This criterion is only fulfilled for five of Mustill et al. (2018a) events. For the same five events, a shift of the combined centre of light above 0.1 mas is expected. In our sample, 127 events fulfill the 1 mmag criterion, and for 20 events the magnification is above 0.1 mag. For 104 and 18 of those, respectively, the motion of the background source is not known from *Gaia* DR2, but will probably be given in future data releases. For all of our photometric events, Figure 4.12 shows the magnification and the predicted date. Since the predicted separation has to be really small, of the order of θ_E , in order to produce a photometric effect, almost all predicted magnifications are not significant, especially when *Gaia* DR2 provides only a two-parameter solution for the background source. In passing, we note that for many of these photometric events the difference between the L2 magnification and the magnification seen from Earth is measurable.

Two photometric microlensing events in 2019

In June 2019, a $G = 15.2$ mag star (*Gaia* DR2 source id: 5862333044226605056) has passed a $G = 18.1$ mag star with a closest separation of (6.48 ± 3.4) mas. For this event we determined an Einstein radius of (4.66 ± 0.24) mas. The blended centre of light has been shifted by $(\delta\theta_{c,lum} = 0.18 \pm 0.06)$ mas and we expected a magnification of (0.011 ± 0.014) mag.

The second event happened in November 2019 when the $G = 17.2$ mag star 2MASS J13055171-7218081 (*Gaia* DR2 source id: 5840411363658156032) passed a $G = 18.2$ mag star with a closest separation of (5.83 ± 1.32) mas. We determined an Einstein radius of (3.56 ± 0.18) mas. We expected a magnification of (0.032 ± 0.019) mag and the estimated shift of the

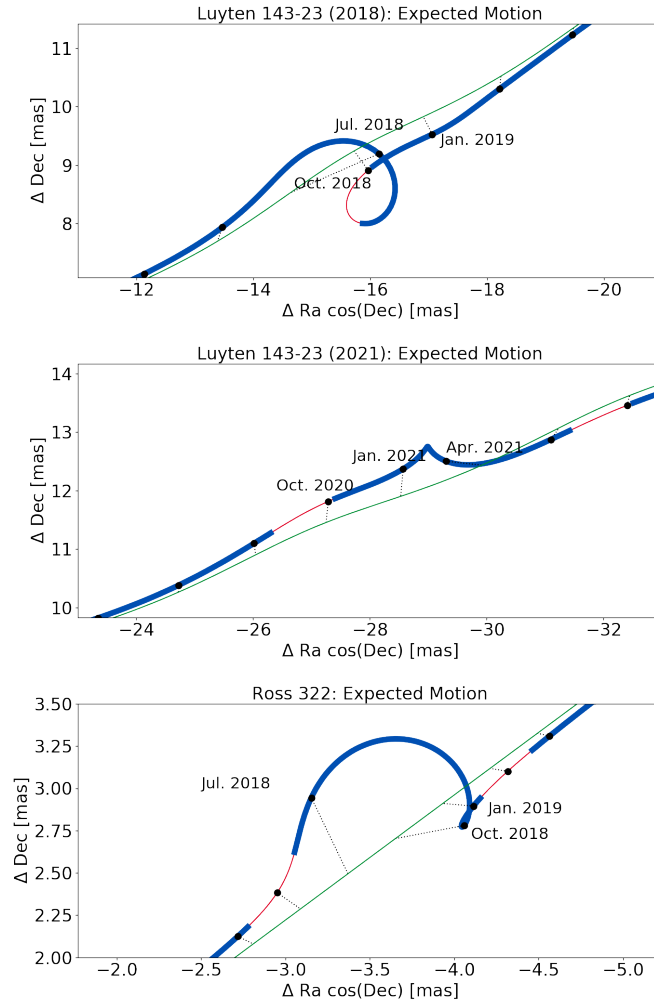


FIGURE 4.11: Predicted motions of the background stars for the events by Luyten 143-23 in 2018 (top), in 2021 (middle), and by Ross 322 in 2018 (bottom). The origin of the coordinate system is the background star's J2015.5 position. The thin green lines show the unaffected motions of the background stars, while the expected paths due to gravitational lensing are shown as thick blue/thin red lines, where the red parts indicate the epochs at which the star is not observable. The black dots indicate equal time intervals of 3 months. $\delta\theta_+$ is the difference between both lines at the same epoch indicated as black dotted lines (adapted from Klüter et al., 2018a, Figure 2).

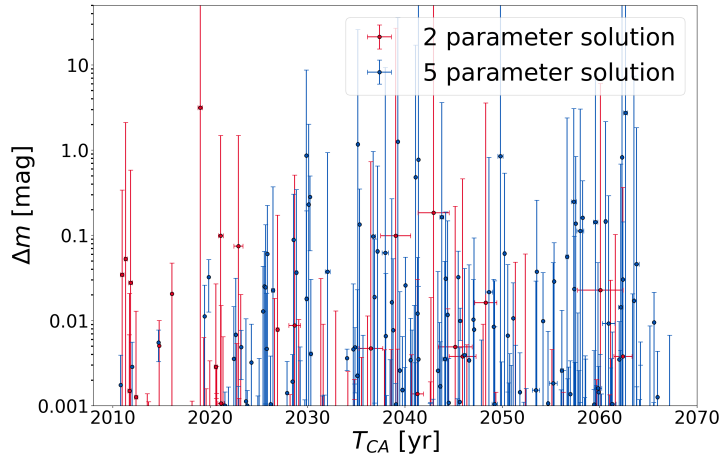


FIGURE 4.12: Expected maximum magnification for all photometric events, with (blue) and without (red) a five-parameter solution for the background source in *Gaia* DR2 (adapted from Klüter et al., 2018b, Figure 10).

combined centre of light to be (0.50 ± 0.08) mas. Both events are listed in Table A.1 #3 and #4). Both events were also predicted by McGill et al. (2019b). Furthermore, they showed that it might be possible to determine the mass of the lenses with an accuracy of 30% and 20%, respectively, assuming a precision of 1 mmag. The event of 2MASS J13055171-7218081 was also predicted independently by Bramich (2018).

4.7 Summary and conclusion

We determined a list of $\sim 148\,000$ high-proper-motion stars using *Gaia* DR2. We then searched for background sources close to their paths and found $\sim 68\,000$ candidates for astrometric microlensing events. For those, we computed the closest projected distances and the expected astrometric and photometric effects. The main difficulty in this process was to sort out probably erroneous DR2 data while losing as few valid events as possible. We chose the rejection criteria such as to be confident that our list shows a small false positive rate, while not deleting too many promising predictions.

Because of the large sample, and due to limited resources, we were not able to perform a Monte Carlo simulation to determine the uncertainties of our predictions. Instead, we used

an analytical error propagation, which leads to robust values as long as the relative errors are small. At small separations, the derived uncertainties for shift and magnification tend to be overestimated.

In total, we gave predictions for 3914 microlensing events caused by 2875 different lens stars with an expected shift of the brighter image larger than 0.1 mas. Currently, this is the largest available catalogue of predicted events. Thanks to the precise data of *Gaia* DR2, we were able to predict the date of the closest approach with a typical accuracy of a few weeks. In the best cases the standard error can be only a few hours. This is much smaller than the duration of the events. The standard error for the minimum separation is typically on the order of a few dozen mas. Large uncertainties are mostly caused by unknown proper motions of the source. As expected, the standard errors increase with the time before and after J2015.5. However, for the year 2065, it is still possible to predict events with a separation significantly below 100 mas ($d + 3\sigma_d < 100$ mas). Typically, the lenses are much brighter than the sources. Half of the events have even a difference in *G* magnitude above 6 mag. These are hard to observe, but by using more suitable wavelength bands the brightness differences can be reduced.

Based on *Gaia* DR2, [Bramich \(2018\)](#) has reported 76 events during the *Gaia* mission life time (between J2014.5 and J2026.5), and [Bramich and Nielsen \(2018\)](#) predicted 2509 events between 2026.5 and 2100. Out of the 76 events published by [Bramich \(2018\)](#), we independently discovered 60 of his events. The dates and impact parameters of the common events are similar except for ten events where [Bramich \(2018\)](#) listed the dates close to J2026.5 or J2014.5 and we expect the date a few years later or earlier. Out of the 2509 events predicted by [Bramich and Nielsen \(2018\)](#) we only detected 656 events, due to different selection criteria and time ranges. The independent detection of those shows the reliability of the respective methods. For all common events, the predicted dates and impact parameters are similar, within the standard errors. The masses of the lenses estimated by [Bramich \(2018\)](#) and [Bramich and Nielsen \(2018\)](#) are typically 10% larger than the approximated masses in this study. Hence, we tend to underestimate the effect, leading to a conservative prediction. Most of the events which we did not reproduce have a date of the closest approach after 2065.5 (1263 cases). Of the remaining 666 events, only 56 have a total proper motion of the lens above 150 mas/yr. We deliberately excluded these events from our sample due to the following reasons: The majority have either a positional uncertainty of the source above 10 mas (26 cases), a separation larger than 7'' (13 cases) or comparable proper motions between lens and source (3 cases). Two events are excluded due to a low tangential velocity of the lens. For 12 events, the exact reason is not known, however since

the expected shift estimated by [Bramich and Nielsen \(2018\)](#) is only slightly above our limit of $\delta\theta_+ > 0.1$ mas it is most likely that we determined a shift below 0.1 mas.

We also independently recovered the events of WD 1142-645 predicted by [McGill et al. \(2018\)](#) and the one of Stein 2051B, which was already observed by [Sahu et al. \(2017\)](#).

Observations of the events and the determination of the lens masses will lead to a better understanding of mass relations for main-sequence stars ([Paczynski, 1991](#)). Perhaps even more interestingly, our sample contains also events caused by 352 different white dwarfs. The observation and subsequent mass determination of those will help to gain insights on white dwarfs and on the final phase of the evolution of stars. Additionally, white dwarfs are also the ideal lenses due to their low brightness in relation to their mass.

It might also be interesting to observe the potential photometric events. However, these can only be predicted with low confidence. It might be helpful to study these events in more detail. For the two events in 2019 such a study was carried out by [McGill et al. \(2019b\)](#).

With *Gaia* eDR3 (expected in late 2020) we expect an improvement of the standard errors. In other words, the precision of the predicted events will increase. In addition, the number of background sources with five-parameter solutions will increase, which again leads to better predictions. Furthermore, *Gaia* DR3 will include some detections and a treatment of binary stars, while for *Gaia* DR2 all stars were treated as single stars. This will help to make improve the predictions for the paths of the lenses.

Chapter 5

Measuring stellar masses using astrometric microlensing with *Gaia*¹⁶

5.1 Introduction

Besides the predictability of the events, another advantage of astrometric microlensing is the timescale of a few months (Dominik and Sahu, 2000). For events with large Einstein radii, a deflection can be measured even over a period of a few years. Therefore, they might be detected and characterised by *Gaia* alone, even though *Gaia* observes each star only occasionally. Due to the precision of *Gaia*'s astrometric measurements it might be possible, for *Gaia* to measure the positional shift of the background star. However, this depends on the temporal distribution of measurements, and since *Gaia* effectively measures only in along-scan direction, it depends also on the orientation of each measurement. Hence, for a reliable estimate on the expected precision, it is necessary to know the location and orientation of the event. Such knowledge may help in order to plan observational campaigns. This is the aim of the study published in Klüter et al. (2020), where my co-authors and I simulated the individual *Gaia* measurements of 501 predicted astrometric microlensing events. In this chapter, our simulation and analysis is presented. The basic structure of the simulated data set is illustrated in Figure 5.1. First, the selection of lens and source stars are discussed (Section 5.2). Afterwards, we calculated the observed positions using the *Gaia* DR2 positions, proper motions, and parallaxes, as well as an assumed mass (Subsection 5.3.1; Figure 5.1 solid grey and solid blue lines). We then determined the one-dimensional *Gaia* measurements including realistic uncertainties (Subsection 5.3.2 and 5.3.3; Figure 5.1 black rectangles). Finally, we simultaneously fitting the motion of lens and source

¹⁶The Python-based code for our simulation is has been made publicly available at <https://github.com/jkluter/MLG>

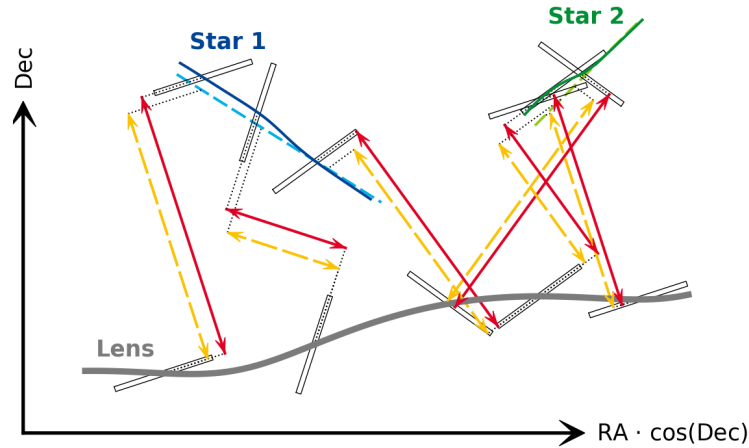


FIGURE 5.1: Illustration of our simulation. While the lens (thick grey line) passes the background star 1 (dashed blue line) the observed position of the background star is slightly shifted due to microlensing (solid blue line). The *Gaia* measurements are indicated as black rectangles, where the precision in along-scan direction is much better than the precision in across-scan direction. The red arrows indicate the along-scan separation including microlensing, and the yellow dashed arrows show the along-scan separation without microlensing. The difference between both sources shows the astrometric microlensing signal. Due to the different scanning direction, an observation close to the maximal deflection of the microlensing event does not necessarily have the largest signal. A further background star 2 (green) can improve the result (adapted from Klüter et al., 2020, Figure 4).

to the simulated data using only the residuals in along-scan direction. We repeated these steps to estimate the expected uncertainties of the mass determination via a Monte-Carlo approach (Section 5.4).

In Section 5.5, our results on the opportunities of direct stellar mass determinations by *Gaia* are displayed. Finally, a summary of our simulations and results is given in Section 5.6.

5.2 Data input

We simulated 501 events predicted in the previous chapter with an epoch of the closest approach between 2013.5 and 2026.5. We also included some events outside the most extended mission

of *Gaia* (ending in 2024.5), since it might be possible to determine the mass only from the tail of an event, or from using both *Gaia* measurements and additional observations. This is true for the events #62 - #65 in Table A.3. The sample is naturally divided into two categories: events where the motion of the background source is known, and events where the motion of the background source is unknown. A missing proper motion in DR2 will not automatically mean that *Gaia* cannot measure the motion of the background source, since the data for *Gaia* DR2 are derived only from a 2-year baseline. With the 5-year baseline for the nominal mission, which ended in mid-2019, and also with the potential extended 10-year baseline, *Gaia* is expected to provide proper motions and parallaxes for almost all of those sources. In order to deal with the unknown proper motions and parallaxes, we used randomly selected values from a normal distribution with means of 5 mas/yr and 2 mas, respectively and standard deviations of 3 mas/yr and 1 mas, respectively, while assuming a uniform distribution for the direction of the proper motion. For the parallaxes, we only used the positive part of the distribution. Both distributions roughly reflect the sample of all potential background stars from the previous chapter.

Multiple background sources

As discussed in Chapter 4, many of the high-proper-motion stars pass close enough to multiple background stars, thus causing several measurable astrometric effects. This is also true for 22 lenses, if we consider only the 13 years from 2013.5 to 2026.5. As an extreme case, the light deflection by Proxima Centauri causes a measurable shift (larger than 0.1 mas) on 18 background stars. This is due to the star's large Einstein radius, its high proper motion and the dense background. Since those events are physically connected, we simulated and fitted the motion of the lens and multiple background sources simultaneously (see Figure 5.1, Star 2). We also compared three different scenarios: A first one where we used all background sources for the mass estimate, a second one where we only selected those with known proper motion and a third one where we only selected those with a precision in along-scan direction better than 0.5 mas per field of view transit (assuming 9 CCD observations). The latter limit corresponds roughly to sources brighter than $G \simeq 18.5$ mag.

5.3 Simulation of *Gaia*'s individual astrometric measurements

We expect that *Gaia* DR4 and the full release of the extended mission will provide for each single CCD observation the position and uncertainty in along-scan direction, in combination

with the observation epochs. These data were simulated as a basis for the presented study. We thereby assumed that all variations and systematic effects caused by the satellite itself are corrected beforehand. However, since we are only interested in relative astrometry, measuring the astrometric deflection is not affected by most of the systematics, as for example the slightly negative parallax zero-point (Luri et al., 2018). In addition to the astrometric measurements, *Gaia* DR4 will also publish the scan angle and the barycentric location of the *Gaia* satellite for each measurement.

We found that our results strongly depend on the temporal distribution of the measurements and their scan directions. Therefore, we used the predefined epochs and scan angles for each event, provided by the *Gaia* observation forecast tool (GOST)¹⁷ online tool. This tool only lists the times and angles when a certain area is passing the field of view of *Gaia*. However, it is not guaranteed that a measurement is actually taken and transmitted to Earth. We assumed that for each transit, *Gaia* measures the position of the background source and lens simultaneously (if resolvable), with a certain probability for missing data points and clipped outliers.

To implement the parallax effect for the simulated measurements, we assumed that the position of the *Gaia* satellite is exactly at a 1% larger distance to the Sun than the Earth. Compared to a strict treatment of the actual *Gaia* orbit, we did not expect any differences in the results, since first, *Gaia*'s distance from this point (roughly L2) is very small compared to the distance to the Sun, and second, we consistently used 1.01 times the Earth orbit for the simulation and for the fitting routine. We note that in principle both routines can be provided with an arbitrary location, hence observations from different sites can be fitted simultaneously.

The simulation of the astrometric *Gaia* measurements is described in the following subsections.

5.3.1 Astrometry

Using the *Gaia* DR2 data as input parameters of the position (α_0, δ_0) , proper motions $(\mu_{\alpha^*,0}, \mu_{\delta,0})$ and parallaxes (ϖ_0) we calculated the unlensed positions α_t, δ_t of lens and background source seen by *Gaia* as a function of time (see Figure 5.1 solid grey line and dashed blue line), using the following equation:

$$\begin{pmatrix} \alpha_t \\ \delta_t \end{pmatrix} = \begin{pmatrix} \alpha_0 \\ \delta_0 \end{pmatrix} + (t - t_0) \begin{pmatrix} \mu_{\alpha^*,0} / \cos \delta_0 \\ \mu_{\delta,0} \end{pmatrix} + 1.01 \cdot \varpi_0 \cdot \mathbf{J}_{\Theta}^{-1} \mathbf{E}(t), \quad (5.1)$$

¹⁷*Gaia* observation forecast tool: <https://gaia.esac.esa.int/gost/>

where $\mathbf{E}(t)$ is the barycentric position of the Earth, in Cartesian coordinates and in astronomical units, and

$$\mathbf{J}_{\Theta}^{-1} = \begin{pmatrix} \sin \alpha_0 / \cos \delta_0 & -\cos \alpha_0 / \cos \delta_0 & 0 \\ \cos \alpha_0 \sin \delta_0 & \sin \alpha_0 \sin \delta_0 & -\cos \delta_0 \end{pmatrix} \quad (5.2)$$

is the inverse Jacobian matrix for the transformation into a spherical coordinate system, evaluated at the lens position.

We then estimated the observed position of the source (see Figure 5.1 solid blue line) by adding the microlensing term. To do so we used the approximated mass determined in the previous chapter (Section 4.5). Here we assumed that all our measurements are in the resolved case. That means, *Gaia* observes the position of the major image of the source. Further, we assumed that the measurement of the lens position is not affected by the minor image of the source. Using Equation (2.16), the exact location of the image can be calculated as follows:

$$\begin{pmatrix} \alpha_{obs} \\ \delta_{obs} \end{pmatrix} = \begin{pmatrix} \alpha_t \\ \delta_t \end{pmatrix} + \begin{pmatrix} \Delta\alpha_t \\ \Delta\delta_t \end{pmatrix} \cdot \left(\sqrt{0.25 + \frac{\theta_E^2}{\Delta\phi_t^2}} - 0.5 \right), \quad (5.3)$$

where $\Delta\phi_t = \sqrt{(\Delta\alpha_t \cos \delta_t)^2 + (\Delta\delta_t)^2}$ is the unlensed angular separation between lens and source and $(\Delta\alpha_t, \Delta\delta_t) = (\alpha_{t,source} - \alpha_{t,lens}, \delta_{t,source} - \delta_{t,lens})$ are the unlensed differences in right ascension and declination, respectively. However, this equation shows an unstable behaviour in the fitting process, caused by the square root. This results in a time-consuming fitting process. To overcome this problem we used the shift of the centre of light (Equation (2.17)) as approximation for the shift of the brightest image. This approximation is used for both the simulation of the data and the fitting procedure:

$$\begin{pmatrix} \alpha_{obs} \\ \delta_{obs} \end{pmatrix} = \begin{pmatrix} \alpha_t \\ \delta_t \end{pmatrix} + \begin{pmatrix} \Delta\alpha_t \\ \Delta\delta_t \end{pmatrix} \cdot \frac{\theta_E^2}{(\Delta\phi_t^2 + 2\theta_E^2)}. \quad (5.4)$$

The differences between Equation (5.3) and Equation (5.4) are by at least a factor 10 smaller than the measurements errors (for most of the events even by a factor 100 or more). Furthermore, using this approximation we underestimated the microlensing effect, thus being on a conservative track for the estimation of mass determination efficiency.

We did not include any orbital motion in this analysis even though SIMBAD listed some of the lenses (e.g. 75 Cnc) as binary stars. However, from an inspection of their orbital parameters

(e.g. periods of a few days, see [Pourbaix et al., 2004](#)), we expected that this would influence our result only slightly. Furthermore, an inclusion of the orbital motion would only be meaningful if a good prior would be available. This might come for a few sources with *Gaia* DR3 (expected by the end of 2021).

5.3.2 Resolution

As discussed in Subsection 3.1.3, the resolution of *Gaia* is currently not limited by *Gaia*'s optical point-spread function, but limited by the size of the readout windows (it is not yet clear how much this can be improved for future data releases). Using the apparent position and G magnitude of lens and source, we investigated for all given epochs whether *Gaia* can resolve both stars or only measure the brightest of both (mostly the lens, see Figure 3.4). We therefore calculated the separation both in along-scan and across-scan direction, as

$$\begin{aligned}\Delta\phi_{AL} &= |\sin\Theta \cdot \Delta\alpha_{obs} \cos\delta_{obs} + \cos\Theta \cdot \Delta\delta_{obs}|, \\ \Delta\phi_{AC} &= |\cos\Theta \cdot \Delta\alpha_{obs} \cos\delta_{obs} - \sin\Theta \cdot \Delta\delta_{obs}|,\end{aligned}\tag{5.5}$$

where Θ is the position angle of the scan direction counting from North towards East. When the fainter star is outside of the readout window of the brighter star, i.e. the separation in along-scan direction is larger than 354 mas or the separation in across-scan direction is larger than 1062 mas, we assumed that *Gaia* measures the positions of both sources. Otherwise we assumed that only the position of the brightest star is measured, unless both sources have a similar brightness ($\Delta G < 1$ mag). In that case, we excluded the measurements of both stars.

5.3.3 Measurement errors

In order to include a realistic representation for the uncertainty in along-scan direction, we derived an analytical relation as function of G magnitude as follows. We started with the equation for the end-of-mission parallax standard error (Equation (3.1)), where we ignore the additional colour term (see Figure 5.2, light-blue dashed line). We then adjusted this relation in order to describe the actual precision in along-scan direction per CCD shown in [Lindgren et al. \(2018\)](#) (Figure 5.2, solid blue line) by multiplying it with a factor of 7.75 and adding an offset of 100 μas . We also adjusted z (Equation (3.2)) to be constant for $G < 14$ mag (Figure 5.2, green dotted line). These adjustments are done heuristically. For bright sources, we overestimated the precision, however most of the background sources, which carry the astrometric microlensing signal, are

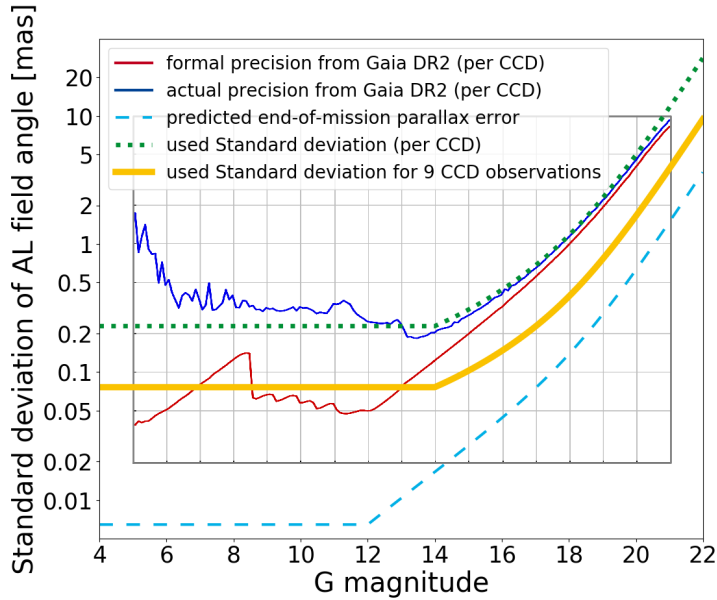


FIGURE 5.2: Precision in along-scan direction as function of G magnitude. The red line indicates the expected formal precision from *Gaia* DR2 for one CCD observation. The blue solid line is the actually achieved precision (Lindegren et al., 2018). The light blue dashed line shows the relation for the end-of-mission parallax error (Gaia Collaboration et al., 2016b), and the green dotted line shows the adopted relation for the precision per CCD observation for the present study. The adopted precision for using all nine CCDs observations is shown as the thick yellow curve. The inset (red and blue curve) is taken from Lindegren et al. (2018), Figure 9; (adapted from Klüter et al., 2020, Figure 3).

fainter than $G = 13$ mag. For those sources the assumed precision is slightly worse compared to the actually achieved precision for *Gaia* DR2. In the future, a better treatment of systematics may improve the uncertainties for the bright sources. We did not simulate all CCD measurements separately, but rather a mean measurement of all eight or nine CCD measurements during a field of view transit. The scatter between the CCD measurements can be used to assess the uncertainties and to remove outliers. Finally, we assumed that during each field-of-view transit all nine (or eight) CCD observations are usable. Hence, we divide the CCD precision by $\sqrt{N_{CCD}} = 3$ (or 2.828) to determine the standard error in along-scan direction per field-of-view

transit:

$$\sigma_{AL} = \frac{\left(\sqrt{-1.631 + 680.766 \cdot \tilde{z} + 32.732 \cdot \tilde{z}^2} \cdot 7.75 + 100\right)}{\sqrt{N_{CCD}}} \mu\text{as}, \quad (5.6)$$

with

$$\tilde{z} = 10^{(0.4(\max(G, 14) - 15))}. \quad (5.7)$$

In across-scan direction we assumed a precision of $\sigma_{AC} = 1''$. This is only used as a rough estimate for the simulation, since only the along-scan component is used in the fitting routine.

For each star and each field-of-view transit we picked a value from a 2D Gaussian distribution with σ_{AL} and σ_{AC} in along-scan and across-scan direction, respectively, as positional measurement. Finally, the data of all resolved measurements were forwarded to the fitting routine. These contain the positional measurements (α_{obs} , δ_{obs}), the standard error in along-scan direction (σ_{AL}), the epoch of the observation (t), the current scanning direction (Θ) as well as an identifier for the corresponding star (i.e. if the measurement corresponds to the lens or source star). The “true” values, i.e the position, proper-motion, parallax and mass, used for the simulation are separately stored for a comparison.

5.4 Mass reconstruction and analysis of fit results

To reconstruct the mass of the lens we fitted Equation (5.4) (including the dependencies of Equation (2.4) and (5.1)) to the observations of the lens and the source simultaneously. For this we used a weighted-least-squares method. Since *Gaia* measures precisely in along-scan direction only (see Figure 5.1 black boxes), we computed the weighted residuals r as follows:

$$r = \frac{\sin \Theta (\alpha_{model} - \alpha_{obs}) \cdot \cos \delta_{obs} + \cos \Theta (\delta_{model} - \delta_{obs})}{\sigma_{AL}}, \quad (5.8)$$

while ignoring the across-scan component. The open parameters of this equation are the mass of the lens as well as the 5 astrometric parameters of the lens and of each source. This adds up to 11 fitted parameters for a single event, and $5 \times n + 6$ fitted parameters for the case of n background sources (e.g. $5 \times 18 + 6 = 96$ parameters for the case of 18 background sources of Proxima Centauri).

The used least-squares method is a Trust-Region-Reflective algorithm (Branch et al., 1999), which we also provided with the analytic form of the Jacobian matrix of Equation (5.8) (including all inner dependencies from Equations (2.4), (5.1) and (5.4)). We did not limit the parameter

space to positive masses and parallaxes, since, due to the noise, there is a non-zero probability that the determined mass will be below zero. As an initial guess, we used the first data point of each star as position, along with zero parallax, zero proper motion as well as a mass of $M = 0.5 M_{\odot}$. One could use the motion without microlensing to analytically calculate an initial guess, however, we found that this neither improves the results or reduces the computing time significantly.

Via a Monte Carlo approach, we then estimated the precision of the mass determination. We first create a set of error-free data points using the astrometric parameters provided by *Gaia* and the approximated mass of the lens based on the G magnitude estimated in Section 4.5. We then created distinct 500 sets of observations by randomly picking values from the error ellipse of each data point. We also included a 5% chance that a data point is missing, or is clipped as an outlier. From the sample of 500 reconstructed masses, we determined the 15.8, 50, and 84.2 percentiles (see Figure 5.3). These represent the median and the 1σ confidence interval. It should be mentioned that using the real observations will lead to one value from the determined distribution and not necessarily a value close to the true or median value. However, the standard deviation of our simulated distribution will be similar to the precision of a real measurement. Furthermore, the median value provides an insight whether we can reconstruct the correct value.

To determine the influence of the input parameters, we repeated this process 100 times while varying the positions, proper motions and parallaxes of the lens and source as well as the mass of the lens, within the individual error distributions. This additional analysis was only done for events where the first analysis using the error-free values derived from *Gaia* DR2 led to a 1σ uncertainty smaller than the assumed mass of the lens.

5.5 Results

Using the method described above, we determined the scatter of individual fits. The scatter gives us an insight into the reachable precision of the mass determination using the individual *Gaia* measurements. In our analysis we found three different types of distributions. For each of these, a representative case is shown in Figure 5.3. For the first two events (Figure 5.3 (A) and 5.3 (B)), the width of the distributions, calculated via the 50th percentile minus the 15.8th percentile and the 84.2th percentile minus the 50th percentile, is smaller than 15% and 30% of the assumed mass, respectively (These value roughly reflects the standard errors of the distribution). For such events it will be possible to determine the mass of the lens once the individual *Gaia* observations

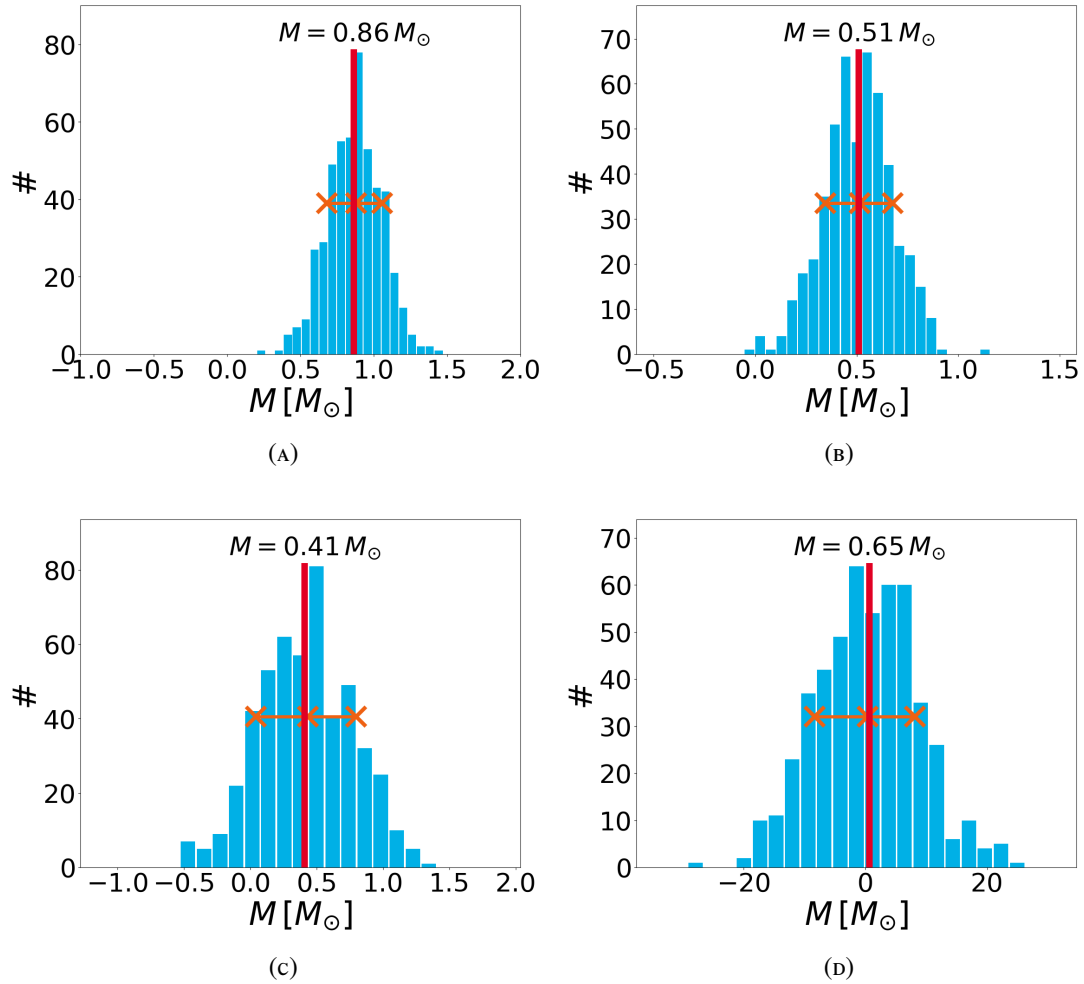


FIGURE 5.3: Histogram of the simulated mass determination for four different cases: (A) and (B) show a relative uncertainty of about 15% and 30%, respectively; *Gaia* is able to measure the mass of the lens; (C) shows a relative uncertainty between 50% and 100%; for these events *Gaia* can detect a deflection, but a good mass determination is not possible; In (D) the scatter is larger than the mass of the lens; *Gaia* is not able to detect a deflection of the background source. The orange crosses show the 15.8th, 50th and 84.2th percentiles (1σ confidence interval) of the 500 realisations, and the red vertical line indicates the input mass. Note the much wider x-scale for case (D)! (adapted from Klüter et al., 2020, Figure 5)

are released. For the event in Figure 5.3 (C) the standard error is of the same order as the mass itself. For such events the *Gaia* data are affected by astrometric microlensing, but the signal is not strong enough to determine a precise mass. By including further (non-*Gaia*) data, for example from HST observations during the peak of the event, a good mass determination might be possible. This is of special interest for upcoming events in the next years. If the scatter is much larger than the mass itself as in Figure 5.3 (D), the mass cannot be determined using the *Gaia* data.

5.5.1 Single background source

In this analysis, we tested 501 microlensing events, predicted in the previous chapter, with a date of the closest approach between J2013.5 until J2026.5. Using data for the potential 10-year extended *Gaia* mission, we found that the mass of 13 lenses can be reconstructed with a relative uncertainty of 15% or better. Further 21 events can be reconstructed with a relative standard uncertainty better than 30% and additional 31 events with an uncertainty better than 50% (i.e. $13 + 21 + 31 = 65$ events can be reconstructed with an uncertainty smaller than 50% of the mass). The percentage of events, where we were able reconstruct the mass, increases with the mass of the lens (see Figure 5.4). This is not surprising since a larger lens mass results in a larger microlensing effect. Nevertheless, with *Gaia* data it is also possible to derive the masses of some of the low-mass stars ($M < 0.65 M_{\odot}$), with a small relative error ($< 15\%$). It was also expected that for brighter background sources it is easier to reconstruct the mass of the event (Figure 5.6 top panel), due to the better precision of *Gaia* (see Figure 5.2). Furthermore, the impact parameters of the reconstructable events are typically below $1.67''$ with a peak around $0.35''$ (Figure 5.6 bottom panel). This is caused by the size of *Gaia*'s readout windows. Using only the data of the nominal 5-year mission the same trend can be observed. However, apart from the fact that most of the events reach the maximal deflection after the end of the nominal mission (2019.5), the fraction of events with a given relative uncertainty of the mass reconstruction is much smaller due to the fewer data points and the typically larger impact parameters (see Figure 5.5). Hence, the mass can only be determined for 2, $2 + 5 = 7$, and $2 + 5 + 8 = 15$ events with a relative uncertainty better than 15%, 30% and 50%, respectively.

For 114 events, where the expected relative uncertainty is smaller than 100%, we expect that *Gaia* can at least qualitatively detect the astrometric deflection. For those we repeated the analysis while varying the input parameters for the data simulation. Figure 5.7 shows the achievable precision as a function of the input mass for a representative subsample. If the proper motion

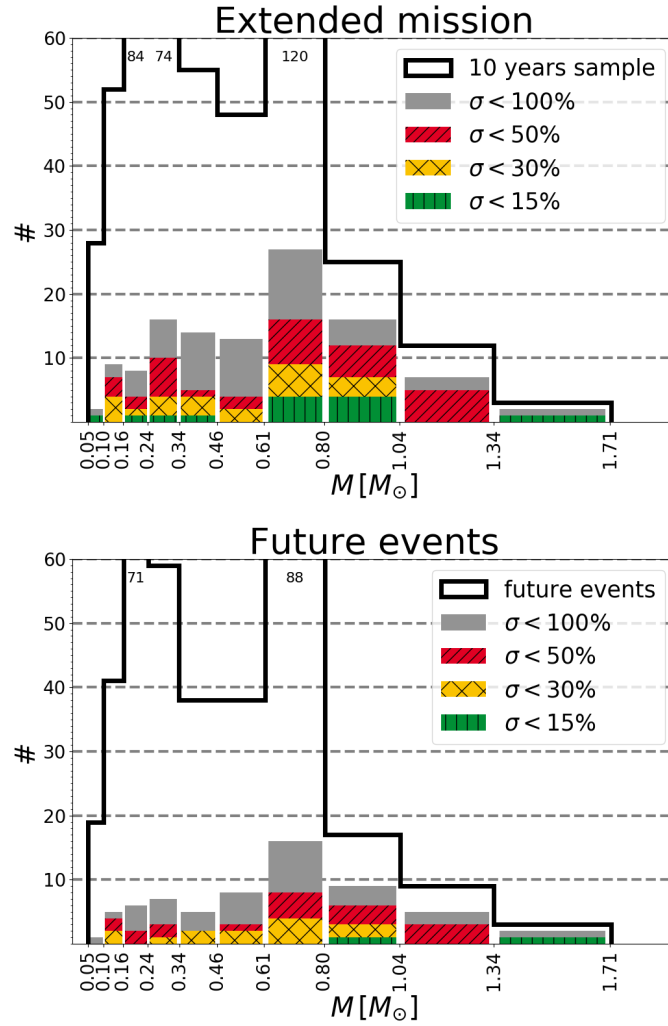


FIGURE 5.4: Distribution of the assumed masses and the resulting relative standard errors of the mass determination for the investigated events. Top panel: Using the data of the extended 10-year mission. Bottom panel: Events with a closest approach after mid-2019. The grey, red, yellow and green parts correspond to a relative standard error better than 100%, 50%, 30% and 15%. The thick black line shows the distribution of the input sample, where the numbers at top show the number of events in the corresponding bins. The peak at $0.65 M_{\odot}$ is caused by the sample of white dwarfs. The bin size increases by a constant factor of 1.25 from bin to bin (adapted from Klüter et al., 2020, Figure 6).

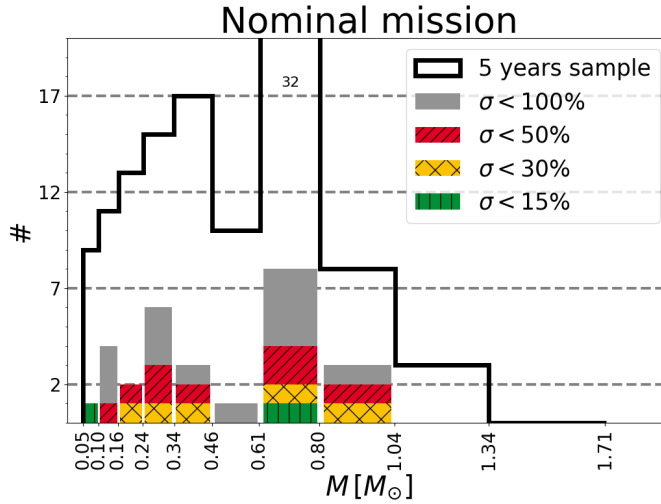


FIGURE 5.5: Distribution of the assumed masses and the resulting relative standard error of the mass determination for the investigated events. Using only the data of the nominal 5-year mission. The grey, red, yellow and green parts correspond to a relative standard error better than 100%, 50%, 30% and 15%. The thick black line shows the distribution of events during the nominal mission, where the numbers at top show the number of events in the corresponding bins. The peak at $0.65 M_{\odot}$ is caused by the sample of white dwarfs. The bin size increases by a constant factor of 1.25 from bin to bin (adapted from Klüter et al., 2020, Figure 6).

of the background star is known from *Gaia* DR2, the uncertainty of the achievable precision is about 6%, and it is about 10% if the proper motion is unknown. We found that the reachable uncertainty (in solar masses) depends only weakly on the input mass, and is closer connected to the impact parameter, which is a function of all astrometric input parameters. Hence, the scatter of the achievable precision is smaller when the proper motion and parallax of the background source is known from *Gaia* DR2. For the 65 events with a relative standard error better than 50%, Table A.2 and Table A.3 list the achievable relative uncertainty for each individual star as well as the determined scatter, for the extended mission σM_{10} . Table A.2 contains all events during the nominal mission (before 2019.5), and also includes the determined scatter using only the data of the nominal mission σM_5 . Table A.3 lists all future events with a closest approach after 2019.5.

Future events

In our sample, 383 events have a closest approach after 2019.5 (Figure 5.4 bottom panel). These events are of special interest, since it is possible to obtain further observations using other telescopes, and to combine the data. In principle, one might expect that about 50% of the events should occur after this date (assuming a constant event-rate per year). However, the events with a closest approach close to the epochs used for *Gaia* DR2 are more difficult to treat by the *Gaia* reduction (e.g. fewer observations due to blending and truncated readout windows). Therefore, many background sources are not included in *Gaia* DR2. For 17 of these future events, the achievable relative uncertainty is between 30% and 50%. Hence, the combination with further precise measurements around the closest approach is needed to determine a precise mass of the lens. To investigate the possible benefits of additional observations, we repeated the simulation while adding two 2-dimensional observations (each consists of two perpendicular 1D observations) around the epoch of the closest approach. We only considered epochs where the separation between the source and lens stars is larger than 150 mas. Furthermore, we assumed that these observations have the same precision as the *Gaia* observations. These results are listed in the column $\sigma M_{obs}/M_{in}$ of Table A.3.

By including these external observations, the results can be improved by typically 2 to 5 percentage points. In extreme cases, the improvement can even be of a factor 2 when the impact parameter is below $0.5''$, since *Gaia* will lose measurements due to combined readout windows. The events #63 to #65 are special cases, since they are outside the extended mission, and *Gaia* will only observe the leading tail of the event.

5.5.2 Multiple background sources

For the 22 events with multiple background sources, we tested three different cases: Firstly, we used all potential background sources. Secondly, we only used background sources where *Gaia* DR2 provides all 5 astrometric parameters, and finally, we selected only those background sources for which the expected precision of *Gaia* individual measurements is better than 0.5 mas. The expected relative uncertainties of the mass determinations for the different cases are shown in Figures 5.8 and 5.9, as well as the expected relative uncertainties for the best case using only one background source. By using multiple background sources, a better precision of the mass determination can be reached. We note that averaging the results of the individual fitted masses will not necessarily increase the precision, since the values are highly correlated.

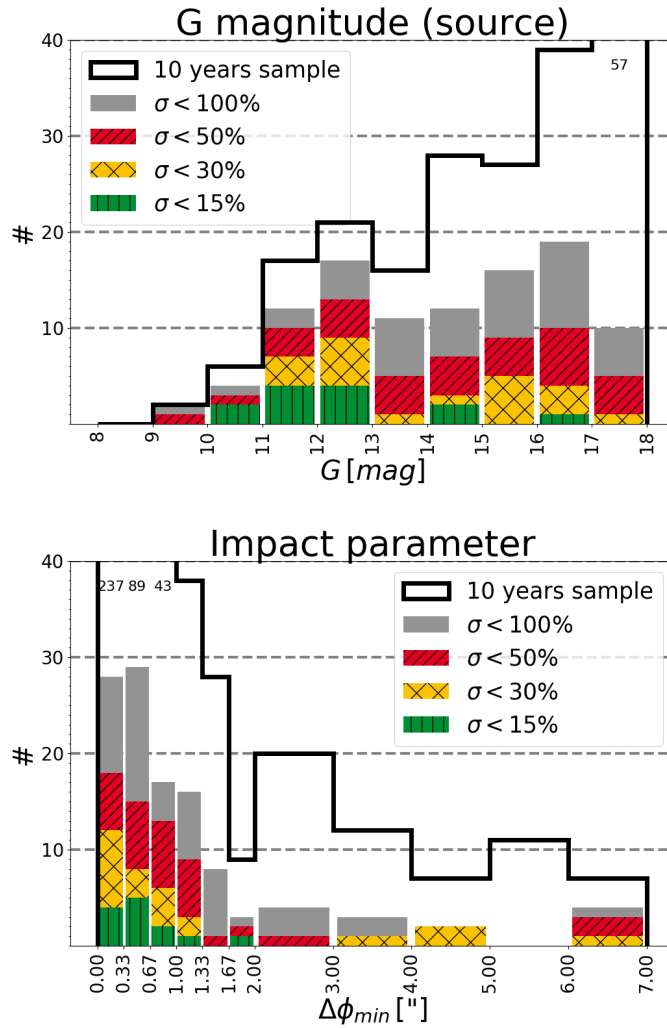


FIGURE 5.6: Distribution of the G magnitude of the source (top) and impact parameter (bottom) as well as the resulting relative standard error of the mass determination for the investigated events. The grey, red, yellow and green parts correspond to a relative standard error better than 100%, 50%, 30% and 15%, respectively. The thick black line shows the distribution of the input sample, where the numbers at the top show the number of events in the corresponding bins. Note the different bin width of $0.33''$ below $\Delta\phi_{min} = 2''$ and $1''$ above $\Delta\phi_{min} = 2''$ in the bottom panel (adapted from Klüter et al., 2020, Figure 7).

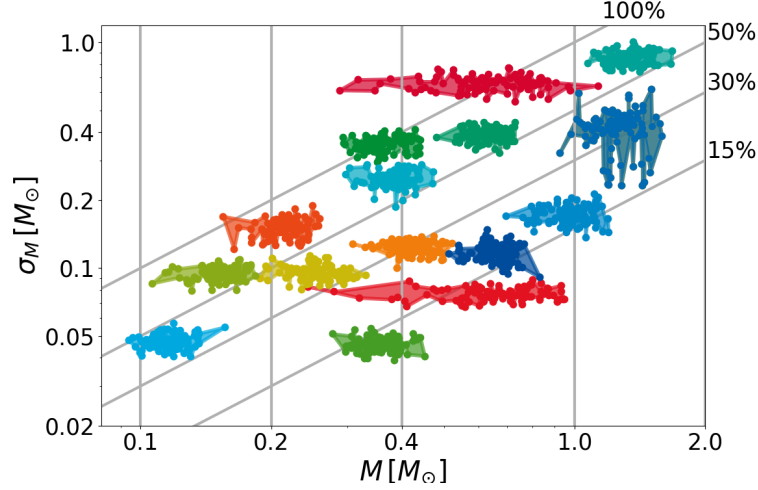


FIGURE 5.7: Achievable standard error as a function of the assumed true mass for 15 events. The two red events with a wide range for the input mass are white dwarfs, where the mass can only be poorly determined from the G magnitude. The absolute uncertainty is roughly constant as a function of the input mass. The diagonal lines indicate relative uncertainties of 15%, 30%, 50% and 100%, respectively (adapted from Klüter et al., 2020, Figure 8).

Using all sources it is possible to determine the mass of Proxima Centauri with a standard error of $\sigma_M = 0.012 M_\odot$ for the extended 10-year mission of *Gaia*. This corresponds to a relative uncertainty of 10%, considering the assumed mass of $M = 0.117 M_\odot$. This is roughly a factor ~ 0.7 better than the uncertainty of the best event only (see Figure 5.8 top panel, $\sigma_M = 0.019 M_\odot \hat{=} 16\%$). Since we do not include the potential data points of the two events predicted by Sahu et al. (2014), it might be possible to reach an even higher precision. For those two events, Zurlo et al. (2018) measured the deflection using the VLT/SPHERE. They derived a mass of $M = 0.150^{+0.062}_{-0.051} M_\odot$. Comparing our expectations with their mass determination, we expect to reach a six times smaller standard error.

A further source which passes multiple background sources is the white dwarf LAWD 37, where we assume a mass of $0.65 M_\odot$. Its most promising event, which was first predicted by McGill et al. (2018) occurred in November 2019. McGill et al. (2018) also mentioned that *Gaia* might be able to determine the mass with an accuracy of 3%. However this was done without knowing the scanning law for the extended mission. We expect an uncertainty for the mass determination by *Gaia* of $0.12 M_\odot$, which corresponds to 19%. Within the extended *Gaia*

mission the star passes 12 further background sources. By combining the information of all astrometric microlensing events by LAWD 37, this result can be improved slightly (see Figure 5.8 (D)). We then expect a precision of $0.10 M_{\odot}$ (16%).

For 8 of the 22 lenses with multiple events the expected relative standard error is better than 50%. The results of these events are given in Table A.4 and displayed in Figure 5.8 and 5.9. In addition to our three cases, a more detailed selection of the used background sources can be done. However, this is only meaningful once the quality of the real data is known.

5.6 Summary and conclusion

In this study, we showed that *Gaia* can determine stellar masses for single stars using astrometric microlensing. For that purpose we simulated the individual *Gaia* measurements for 501 predicted events during the *Gaia* era, using conservative cuts on the resolution and precision of *Gaia*.

In a similar study, [Rybicki et al. \(2018\)](#) showed that *Gaia* might be able to measure the astrometric deflection caused by a stellar-mass black hole ($M \sim 10 M_{\odot}$), based on results from a photometric microlensing event detected by OGLE ([Wyrzykowski et al., 2016](#)). Further, they claimed that for faint background sources ($G > 17.5$ mag) *Gaia* might be able to detect the deflection of black holes more massive than $30 M_{\odot}$. In the present study, however, we consider bright lenses, which are also observed by *Gaia*. Hence, due to the additional measurements of the lens positions, we found that *Gaia* can measure much smaller masses.

In this study we did not consider orbital motion. However, the orbital motion can be included in the fitting routine for the analysis of the real *Gaia* measurements. *Gaia* DR3 (expected for end of 2021) will include orbital parameters for a fraction of the contained stars. This information can be used to decide if orbital motion has to be considered or not. Further, for a few events where the motion of the source is not listed in *Gaia* DR2 it can not be ruled out that lens and source are part of the same binary system, since the source is blended by the lens in all other full-sky surveys.

We also assumed that source and lens can only be resolved if both have individual readout windows. However, it might be possible to measure the separation in along-scan direction even from the blended measurement in one readout window. Due to the FWHM of 103 mas ([Fabricius et al., 2016](#)) *Gaia* might be able to resolve much closer lens-source pairs. The astrometric microlensing signal of such measurements is stronger. Hence, the results of events with impact

parameters smaller than the window size can be improved by a careful analysis of the data. Efforts in this direction are foreseen by the *Gaia* consortium for *Gaia* DR4 and DR5.

Via a Monte Carlo approach we determined the expected relative precision of the mass determination and found that for 34 events, a precision better than 30%, and sometimes down to 5% can be achieved. By varying the input parameters we found that our results depend only weakly on selected input parameters. The scatter is of the order of 6% if the proper motion of the background star is known from *Gaia* DR2 and of the order of 10% if it is unknown. Moreover, the dependency on the selected input mass is even weaker.

For 17 future events (closest approach after 2019.5), the *Gaia* data alone are not sufficient to derive a precise mass. For these events, it will be helpful to take further observations, for example, using HST, VLT, or the Very Large Telescope Interferometer (VLTI). Such two-dimensional measurements can easily be included in our fitting routine by adding two observations with perpendicular scanning directions. We showed that two additional highly accurate measurements can improve the results significantly, especially when the impact parameter of the event is smaller than 1". However, since the results depend on the resolution and precision of the additional observations, these properties should be implemented for such analyses, which is easily achievable. By doing so, our code can be a powerful tool to investigate different observation strategies. The combination of *Gaia* data and additional information might also lead to better mass constraints for the two previously observed astrometric microlensing events of Stein 51b (Sahu et al., 2017) and Proxima Centauri (Zurlo et al., 2018). Even though for the latter, *Gaia* DR2 does not contain the background sources, we are confident that they have both been observed by *Gaia*. Finally, once the individual *Gaia* measurements are published (DR4 or DR5), our code can be used to analyse the data, which will result in multiple well-measured masses of single stars. The code can also be used to fit the motion of multiple background sources simultaneously. When combining these data, *Gaia* can determine the mass of Proxima Centauri with a precision of $0.012 M_{\odot}$ (10%).

¹⁷For an explanation of a Violin plot see NIST: <https://www.itl.nist.gov/div898/software/dataplot/refman1/auxillar/violplot.htm>

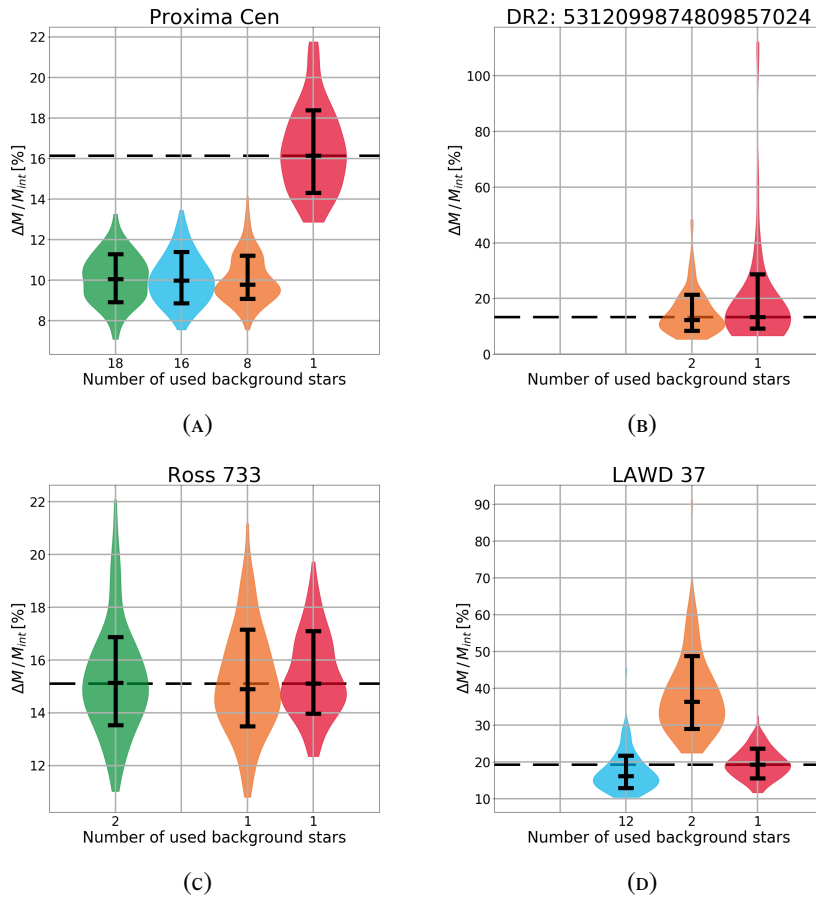


FIGURE 5.8: Violin plot¹⁷ of the achievable uncertainties for the four different methods for: (A) Proxima Centauri, (B) *Gaia* DR2: 5312099874809857024, (C) Ross 733 and (D) LAWD 37. For each method the 16th, 50th and 84th, percentile are shown. The shape shows the distribution of the 100 uncertainties determined by varying the input parameter. This distribution is smoothed with a Gaussian kernel. The green “violins” use all of the background sources. For the blue “violins” only background sources with a 5-parameter solution are used, while for the orange “violins” only stars with a precision in along-scan direction better than 0.5 mas and a 5-parameter solution are taken into account. The red “violins” indicate the best results when only one source is used. The dashed line indicates the median of this distribution. For each method the number of used stars is listed below the “violin”. The missing green “violins” (e.g. LAWD 37 (D)) are due to no additional background stars with a 2-parameter solution only. Hence they would be identical to the blue one and are therefore not determined. Missing blue “violins” (e.g. Ross 733, (C)) are due to no additional background stars sources with a 5-parameter solution have an expected precision in along-scan direction better than 0.5 mas (adapted from Klüter et al., 2020, Figure 9 and 10).

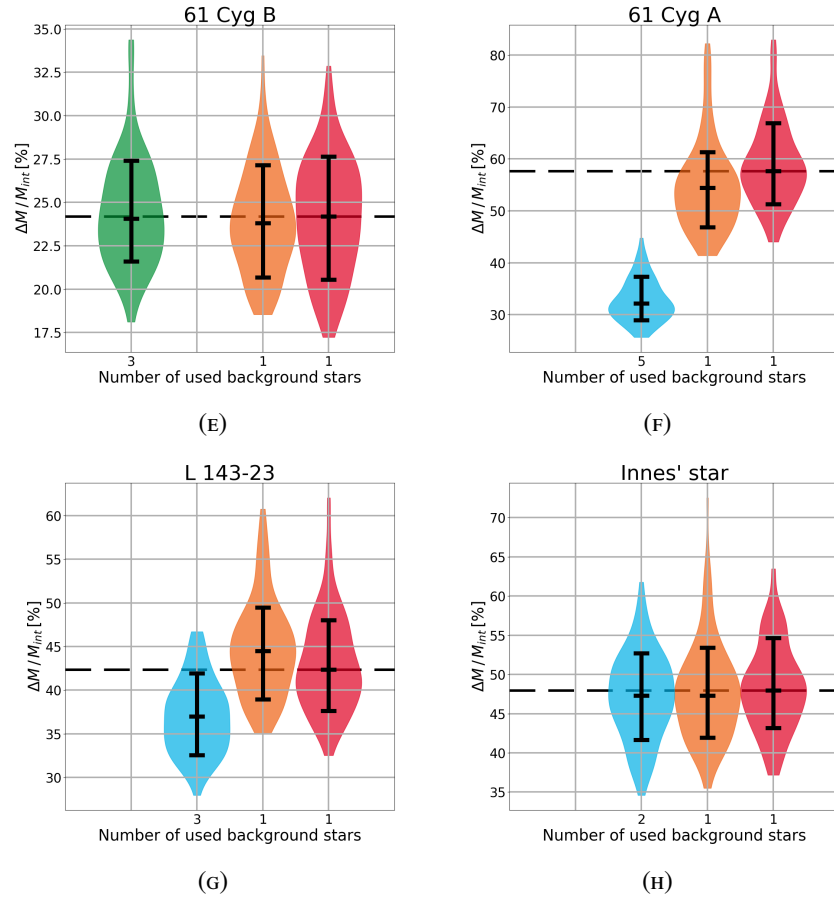


FIGURE 5.9: Violin plot of the achievable precision for the four different methods for: (E) 61 Cyg B, (F) 61 Cyg A, (G) L 143-23 and (H) Innes' star. For each method the 16th, 50th and 84th, percentile are shown. The shape shows the distribution of the 100 uncertainties determined by varying the input parameter. This distribution is smoothed with a Gaussian kernel. The green "violins" use all of the background sources. For the blue "violins" only background sources with a 5-parameter solution are used, while for the orange "violins" only stars with a precision in along-scan direction better than 0.5 mas and a 5-parameter solution are taken into account. The red "violins" indicate the best results when only one source is used. The dashed line indicates the median of this distribution. For each method the number of used stars is listed below the "violin". The missing green "violins" (e.g. L 143-23 (G)) are due to no additional background stars with a 2-parameter solution only. Missing blue "violins" (e.g. 61 Cyg B, (E)) are due to no additional background stars sources with a 5-parameter solution have an expected precision in along-scan direction better than 0.5 mas (adapted from Klüter et al., 2020, Figure 10).

Chapter 6

Summary and perspectives

Within this thesis, I have presented my studies on the use of *Gaia* for astrometric microlensing. After giving an introduction to astrometric microlensing as well as a description of the *Gaia* satellite, I have shown in Chapter 4 how the second data release of *Gaia* can be used to predict astrometric microlensing events in the near and distant future. Through a careful analysis, we managed to determine the largest catalogue of astrometric microlensing events to date. The study can be further extended using future *Gaia* data releases. Besides more precise positions, proper motions and parallaxes, due to a longer baseline, the angular resolution will also be improved due to a better data treatment of the readout windows. In particular, this will increase the number of events in the near future. Furthermore, it is possible to extend the search to lower proper motions. In combination with a better treatment of the readout windows, it will then also be possible to find events of these stars in the nearby future. In addition, the lenses for several of the predicted events are part of a binary system. For some of these, *Gaia* DR3 will publish orbital parameters. The orbital motion can then be included in the analysis, leading to better predictions.

By observing the predicted events, it is possible to determine the mass of individual stars. Furthermore, since the lenses are typically bright sources, it is possible to characterise the lensing star spectroscopically. Hence, these stars are then ideal candidates to calibrate the mass-luminosity function. They may also lead to a better understanding of the structure of isolated stars. During the time working on this thesis, only a few promising events occurred. We investigated if it is possible to observe the event of Luyten 143-23 using GRAVITY at the VLTI (an observation of the event of Ross 322 was not possible due to its location on the sky). Unfortunately during the peak of the event, the source was not observable using ground-based telescopes. An attempt to actually measure this event in December 2018 has failed for technical and scheduling reasons. In 2021 Luyten 143-23 will pass by another background source. The

background source is about 1.5 mag brighter (in G), and the event will be observable during closest approach. Hence, it is a promising target for observations in the near future. Additionally, HST observations of two further events by caused 2MASS J13055171-7218081 and LAWD 37 were initiated by [Sahu et al.\(2019a; 2019b](#), HST proposal, including Klüter, J.).

In Chapter 5, I have demonstrated that *Gaia* can determine the mass for some of the events. This study differs from previous studies (e.g. [Belokurov and Evans, 2002](#); [Rybicki et al., 2018](#)) in four substantial points:

1. This study is based on well-founded assumptions on the performance of *Gaia* based on the second data release.
2. We consider luminous lenses which are typically much brighter than the source. Hence *Gaia* will not only observe the position of the source but also of the lens. Due to this additional data, it is possible to directly determine the mass of the lens even for low-mass stars.
3. The presented study contains real events, hence making it possible to use the real scanning law. The distributions of measurements and scanning directions, however, have a large impact on the determined predictions, since *Gaia* only measures in along-scan direction.
4. This study also discusses the opportunity to determine the mass of the lens by using the positions of multiple background sources. Especially for Proxima Centauri, it is possible to determine the mass from the positional shift of several background sources at larger separations.

We found that *Gaia* can determine the mass for 13 events with a relative standard error below 15%, and for 34 events with a relative standard error below 30%. Additionally, the results can improved if more than on background source is used. Doing so, we expect a mass measurement of Proxima Centauri, with an uncertainty $0.012 M_{\odot}$.

We expect another 200 events during the *Gaia* mission assuming a constant event rate. These tend to have small impact parameters (i.e below the effective angular resolution of *Gaia* DR2). Hence, the astrometric shift would be larger. Even though *Gaia* might not resolve both stars during the epoch of the closest approach, it can determine the angular shift during the tails of the events leading to precise masses.

Once the individual *Gaia* measurements are published, the developed code can be used to determine the masses of lensing stars. For some of these (unpredicted) events it might be possible for *Gaia* to measure the shift of the centre of light of the blended system. This may improve the mass determination, and should then be implemented.

The results for future events can also be improved by including a few additional measurements during the peak of the events. To this end, the developed code can be used to investigate different observations strategies.

An additional extension of this study is the optimisation of the *Gaia* scanning law. The initial phases of the scanning law of *Gaia* have been chosen to observe bright stars close to Jupiter. However, no events are expected for the remaining *Gaia* mission (private communication with F. Mignard). Hence, it might be possible to optimise the scanning law for the rest of the *Gaia* mission in order to precisely measure the mass of one event. By implementing an analytic form of the scanning law we repeated our study for events with a closest approach between 2021 and 2023. We explicitly ignored events without a 5-parameter solution of the source (e.g. 75 Cnc). We found that the standard error for the mass determination of CD-32 12693 and OGLE SMC115.5 319 can be improved by a factor of two. However, even in the best case an uncertainty of 10% and 12% can be reached only. This is not an big improvement, since for other stars such this level can be reached with the current scanning law. Therefore, we refrained from proposing a change of the scanning law to the *Gaia* project.

Even though *Gaia* was faced with several challenges at the beginning of its mission, it provides indispensable data for this study. Moreover, particularly due to its unexpected longevity, *Gaia* is very suitable for predicting, detecting and measuring astrometric microlensing events.

Appendix A

Tables

TABLE A.1: List of 30 especially promising astrometric microlensing events. The table lists the Gaia Source ID of lens and background star, the stellar type (*ST*) of the lens, its mass (*M*), the Einstein radius θ_E , the Julian year T_{CA} after 2000 of the closest approach, with uncertainty, the minimum separation ($\Delta\theta_{min}$), as well as the expected shift of the combined centre of light ($\delta\theta_{c, lum}$), the shift of the brightest image only ($\delta\theta_+$), and the expected magnification (Δm). The corresponding errors are indicated by σ_{\dots} . The full table of 3914 predicted event can be accessed online^a Event #1 #2 and 5 (light grey) are the events of Lythen 143-23 and Ross 322 in 2018 and 2021, respectively. Events #3 and #4 are the photometric events in 2019. Event #11 (dark grey) is the event of Barnard's star in 2035 (Klitter et al., 2018b, Table 2).

#	source ID	Source ID	ST	<i>M</i> M _⊙	θ_E mas	$T_{CA} - 2000$ Year	$\Delta\theta_{min}$ mas	$\sigma_{\Delta\theta_{min}}$ mas	$\delta\theta_{c, lum}$ mas	$\sigma_{\delta\theta_{c, lum}}$ mas	$\delta\theta_+$ mas	$\sigma_{\delta\theta_+}$ mas	Δm mag	$\sigma_{\Delta m}$ mag
1	5254061535097566848	5254061535052907008	MS	0.116	13.9	18.5124	108.6	1.5	0.00384	0.00028	1.76	0.13	1.19E-6	2.4E-7
2	314922605789778048	314922601464808064	MS	0.279	9.8	18.600	125.4	2.0	0.00244	0.00018	0.764	0.056	2.53E-7	5.2E-8
3	5862333044226005056	5862333048529855560	MS	0.400	4.7	19.42	6.5	3.5	0.184	0.069	2.44	0.76	0.011	0.015
4	5840411365658156032	5840411359550016128	MS	0.174	3.6	19.839	5.4	1.4	0.505	0.079	1.69	0.27	0.052	0.020
5	5254061535097566848	5254061535097574016	MS	0.116	14.0	21.1876	280.1	1.7	0.00615	0.00045	0.693	0.050	1.17E-7	2.4E-8
6	468744550065789184	4687445599404851456	WD	0.65	13.	21.500	70.4	2.0	0.98	0.16	2.52	0.41	0.00101	0.00045
7	4248799013208327424	4248799013215266176	MS	0.219	4.1	29.88	0.9	9.7	0.9	3.8	3.8	4.4	0.9	7.9
8	5918299904067162240	5918299908658483840	MS	0.113	6.9	30.248	6.3	2.8	2.17	0.16	4.46	0.84	0.28	0.22
9	613050067036025312	613050067281038080	MS	0.319	2.2	35.16	0.2	7.4	0.4	4.3	2.0	3.5	1.	25.
10	5863711561290571008	5863711561290570112	MS	0.199	3.4	35.33	5.0	3.4	1.79	0.087	1.70	0.69	0.13	0.21
11	447283213094257872	447283292758713216	MS	0.184	28.7	35.764	335.	14.	0.0802	0.0065	2.43	0.20	3.68E-6	9.2E-7
12	6074397471079633328	6074397471080397776	WD	0.65	8.3	36.7	10.	40.	1.7	2.6	5.	10.	0.10	0.87
13	5556349476589422336	5556349472293892224	WD	0.65	7.9	37.17	14.	47.	2.1	3.2	3.7	8.2	0.07	0.59
14	588694260142781760	5886942601374152096	MS	0.180	3.7	39.26	0.3	13.	0.7	8.0	3.5	5.9	1.	35.
15	5715906236031073280	5715906236031079040	WD	0.65	7.9	40.04	20.0	6.9	2.06	0.52	2.71	0.84	0.026	0.030
16	533260622595645952	5332606277474703456	WD	0.65	3.4	40.790	139.6	4.9	0.0470	0.0078	7.7	1.3	3.4E-5	1.6E-5
17	4118914220102650624	4118914185707335040	MS	0.319	7.1	41.38	0.8	14.	0.1	5.1	7.1	6.5	1.	93.
18	428051391503714432	428051391509474816	WD	0.65	8.2	43.6	47.	29.	1.27	0.72	1.39	0.83	0.0017	0.0040
19	5605383430285597696	560538357671689856	WD	0.65	15.	43.973	207.5	4.6	1.04	0.17	1.08	0.18	5.6-5	2.7E-5
20	6282457918962299776	6282457815883084928	WD	0.65	20.	45.47	22.	10.	1.53	0.43	11.7	3.0	0.032	0.033
21	3365063724883180288	3365062964671171712	MS	0.119	11.1	45.61	119.	14.	0.0095	0.0013	1.02	0.14	1.44E-6	7.1E-7
22	1822711900548572544	1822711900548570064	MS	0.212	2.3	49.8	0.3	44.	0.2	7.	2.	21.	1.	100.
23	4203875751318123904	420387564823893696	BD	0.07	5.	53.4	11.	22.	1.2	1.5	2.1	3.1	0.04	0.22
24	4117081643422165120	4117081467277401344	WD	0.65	11.	56.98	66.	25.	1.45	0.55	1.99	0.77	0.0014	0.0021
25	6126095232211644160	6126095300951121024	WD	0.65	5.7	57.3	4.6	32.	1.52	0.22	3.8	9.8	0.2	2.9
26	642625402561169024	642625402559392896	MS	0.272	4.9	58.25	4.5	4.2	1.12	0.20	3.2	1.3	0.16	0.28
27	524359408126953872	524359423068231168	MS	0.175	14.8	58.867	208.4	5.8	0.00767	0.00059	1.042	0.079	3.93E-7	8.9E-8
28	4484348145137238016	448434814513723904	BD	0.07	3.4	60.60	4.	28.	1.06	0.96	1.8	6.3	0.1	2.1
29	6082407619449932032	6082407619449930880	MS	0.560	6.0	62.30	0.08	8.9	0.07	3.8	6.0	4.4	1.	69.
30	2025071788687899776	202507179295978688	WD	0.65	8.1	62.6	0.3	30.	2.	8.	8.	15.	3.	101.

^a<http://dc.zah.uni-heidelberg.de/amLensing/q2/q/Form>

TABLE A.2: Estimated uncertainties of mass measurements with astrometric microlensing with *Gaia* for single events with an epoch of the closest approach during the nominal *Gaia* mission. The table lists the name (Name-Lens) and *Gaia* DR2 source ID (*DR2_ID*-Lens) of the lens and the source ID of the background sources (*DR2_ID*-Source). An asterisk indicates that *Gaia* DR2 provides only the position of the sources. Further, the table lists the epoch of the closest approach (T_{CA}) and the assumed mass of the lens (M_{in}). The expected precision for the use of the data of the extended 10 years mission are given in (σM_{10}), including the uncertainty due to the errors in the input parameters, and as percentage ($\sigma M_{10}/M_{in}$). The expected precision for the use of the nominal 5 years mission is given in (σM_5) if it is below 100% of the input mass (Klüter et al., 2020, Table 1).

#	Name-Lens	<i>DR2_ID</i> -Lens	<i>DR2_ID</i> -Source	T_{CA} Year	M_{in} M_{\odot}	σM_{10} M_{\odot}	$\sigma M_{10}/M_{in}$	σM_5 M_{\odot}
1	HD 22399	488099359330834432	488099363630877824*	2013.711	1.3	$\pm 0.60^{+0.07}_{-0.05}$	47%	
2	HD 177758	4198685678421509376	4198685678400752128*	2013.812	1.1	$\pm 0.41^{+0.04}_{-0.04}$	36%	
3	L 820-19	5736464668224470400	5736464668223622784*	2014.419	0.28	$\pm 0.058^{+0.004}_{-0.004}$	21%	$\pm 0.11^{+0.01}_{-0.01}$
4		2081388160068434048	2081388160059813120*	2014.526	0.82	$\pm 0.39^{+0.05}_{-0.04}$	47%	
5		478978296199510912	478978296204261248	2014.692	0.65	$\pm 0.24^{+0.02}_{-0.02}$	36%	$\pm 0.49^{+0.04}_{-0.04}$
6	G 123-61B	1543076475514008064	1543076471216523008*	2014.763	0.26	$\pm 0.099^{+0.010}_{-0.009}$	37%	$\pm 0.18^{+0.02}_{-0.02}$
7	L 601-78	5600272625752039296	5600272629670698880*	2014.783	0.21	$\pm 0.041^{+0.003}_{-0.004}$	19%	$\pm 0.068^{+0.006}_{-0.005}$
8	UCAC3 27-74415	6368299918479525632	6368299918477801728*	2015.284	0.36	$\pm 0.047^{+0.005}_{-0.005}$	13%	$\pm 0.11^{+0.01}_{-0.01}$
9	BD+00 5017	2646280705713202816	2646280710008284416*	2015.471	0.58	$\pm 0.18^{+0.02}_{-0.02}$	30%	$\pm 0.44^{+0.04}_{-0.05}$
10	G 123-61A	1543076475509704192	1543076471216523008*	2016.311	0.32	$\pm 0.079^{+0.007}_{-0.008}$	24%	$\pm 0.14^{+0.02}_{-0.02}$
11	EC 19249-7343	6415630939116638464	6415630939119055872*	2016.650	0.26	$\pm 0.099^{+0.008}_{-0.008}$	38%	
12		5312099874809857024	5312099870497937152	2016.731	0.07	$\pm 0.0088^{+0.0006}_{-0.0006}$	12%	$\pm 0.0098^{+0.0010}_{-0.0007}$
13	PM J08503-5848	5302618648583292800	5302618648591015808	2017.204	0.65	$\pm 0.17^{+0.02}_{-0.02}$	26%	$\pm 0.29^{+0.03}_{-0.03}$
14		5334619419176460928	5334619414818244992	2017.258	0.65	$\pm 0.23^{+0.02}_{-0.02}$	35%	$\pm 0.43^{+0.04}_{-0.03}$
15	Proxima Centauri	5853498713160606720	5853498708818460032	2017.392	0.12	$\pm 0.034^{+0.003}_{-0.003}$	29%	$\pm 0.082^{+0.006}_{-0.006}$
16	Innes' star	5339892367683264384	5339892367683265408	2017.693	0.33	$\pm 0.16^{+0.02}_{-0.01}$	48%	$\pm 0.22^{+0.02}_{-0.02}$
17	L 51-47	4687511776265158400	4687511780573305984	2018.069	0.28	$\pm 0.035^{+0.003}_{-0.003}$	12%	$\pm 0.046^{+0.004}_{-0.004}$
18		4970215770740383616	4970215770743066240	2018.098	0.65	$\pm 0.076^{+0.008}_{-0.005}$	12%	$\pm 0.21^{+0.02}_{-0.02}$
19	BD-06 855	3202470247468181632	3202470247468181760*	2018.106	0.8	$\pm 0.38^{+0.05}_{-0.05}$	46%	$\pm 0.72^{+0.19}_{-0.08}$
20	G 217-32	429297924157113856	429297859741477888*	2018.134	0.23	$\pm 0.018^{+0.002}_{-0.002}$	7.5%	$\pm 0.040^{+0.003}_{-0.004}$
21		5865259639247544448	5865259639247544064*	2018.142	0.8	$\pm 0.053^{+0.008}_{-0.006}$	6.6%	$\pm 0.12^{+0.02}_{-0.02}$
22	HD 146868	1625058605098521600	1625058605097111168*	2018.183	0.92	$\pm 0.060^{+0.005}_{-0.005}$	6.5%	$\pm 0.14^{+0.02}_{-0.02}$
23	Ross 733	4516199240734836608	4516199313402714368	2018.282	0.43	$\pm 0.067^{+0.005}_{-0.006}$	15%	$\pm 0.13^{+0.01}_{-0.02}$
24	LP 859-51	6213824650812054528	6213824650808938880*	2018.359	0.43	$\pm 0.19^{+0.03}_{-0.03}$	43%	
25	L 230-188	4780100658292046592	4780100653995447552	2018.450	0.15	$\pm 0.073^{+0.007}_{-0.004}$	49%	$\pm 0.11^{+0.01}_{-0.01}$
26	HD 149192	5930568598406530048	5930568568425533440*	2018.718	0.67	$\pm 0.043^{+0.007}_{-0.004}$	6.3%	$\pm 0.12^{+0.01}_{-0.01}$
27	HD 85228	5309386791195469824	5309386795502307968*	2018.751	0.82	$\pm 0.043^{+0.004}_{-0.004}$	5.1%	$\pm 0.65^{+0.05}_{-0.06}$
28	HD 155918	5801950515627094400	5801950515623081728*	2018.773	1	$\pm 0.13^{+0.02}_{-0.02}$	13%	$\pm 0.35^{+0.03}_{-0.03}$
29	HD 77006	1015799283499485440	1015799283498355584*	2018.796	1	$\pm 0.42^{+0.05}_{-0.05}$	41%	
30	Proxima Centauri	5853498713160606720	5853498713181091840	2018.819	0.12	$\pm 0.020^{+0.002}_{-0.002}$	16%	$\pm 0.052^{+0.005}_{-0.005}$
31	HD 2404	2315857227976341504	2315857227975556736*	2019.045	0.84	$\pm 0.19^{+0.02}_{-0.02}$	22%	
32	LP 350-66	2790883634570755968	2790883634570196608*	2019.299	0.32	$\pm 0.15^{+0.02}_{-0.02}$	46%	
33	HD 110833	1568219729458240128	1568219729456499584*	2019.360	0.78	$\pm 0.056^{+0.005}_{-0.004}$	7.2%	

TABLE A.3: Estimated uncertainties of mass measurements with astrometric microlensing with *Gaia* for single events with an epoch of the closest approach after 2019.5. The table lists the name (Name-Lens) and *Gaia* DR2 source ID (*DR2_ID*-Lens) of the lens and the source ID of the background sources (*DR2_ID*-Source). An asterisk indicates that *Gaia* DR2 provides only the position of the sources. Further, the table lists the epoch of the closest approach (T_{CA}) and the assumed mass of the lens (M_{in}). The expected precision for the use of the data of the extended 10 years mission are given in (σM_{10}), including the uncertainty due to the errors in the input parameters, and as percentage ($\sigma M_{10}/M_{in}$). The expected relative precision while including two external 2D observations is given in ($\sigma M_{obs}/M_{in}$) (Klüter et al., 2020, Table 3).

#	Name-Lens	<i>DR2_ID</i> -Lens	<i>DR2_ID</i> -Source	T_{CA} Year	M_{in} M_{\odot}	σM_{10} M_{\odot}	$\sigma M_{10}/M_{in}$	$\sigma M_{obs}/M_{in}$
34	L 702-43	4116840541184279296	4116840536790875904	2019.673	0.22	$\pm 0.085^{+0.006}_{-0.006}$	39%	27%
35	G 251-35	1136512191212093440	1136512191210614272*	2019.856	0.64	$\pm 0.26^{+0.02}_{-0.03}$	39%	39%
36	G 245-47A	546488928621555328	546488928619704320	2019.858	0.27	$\pm 0.075^{+0.006}_{-0.006}$	28%	26%
37	LAWD 37	5332606522595645952	5332606350796955904	2019.865	0.65	$\pm 0.13^{+0.02}_{-0.01}$	19%	12%
38	LSPM J2129+4720	1978296747258230912	1978296747268742784*	2019.960	0.34	$\pm 0.13^{+0.02}_{-0.02}$	38%	9.2%
39		5788178166117584640	5788178170416392192*	2020.126	0.54	$\pm 0.12^{+0.02}_{-0.02}$	22%	6.5%
40	G 16-29	4451575895403432064	4451575895400387968*	2020.214	0.51	$\pm 0.19^{+0.05}_{-0.03}$	37%	17%
41	HD 66553	654826970401335296	654826970399770368*	2020.309	0.87	$\pm 0.11^{+0.02}_{-0.02}$	12%	9%
42	HD 120065	1251328585567327744	1251328589861875840*	2020.344	1.2	$\pm 0.54^{+0.09}_{-0.06}$	44%	42%
43	HD 78663	3842095911266162432	3842095915561269888*	2020.356	0.8	$\pm 0.28^{+0.05}_{-0.04}$	34%	32%
44	HD 124584	5849427049801267200	5849427114177683584*	2020.742	1.2	$\pm 0.47^{+0.06}_{-0.04}$	39%	39%
45	Proxima Centauri	5853498713160606720	5853498713181092224	2020.823	0.12	$\pm 0.023^{+0.002}_{-0.002}$	19%	19%
46	HD 222506	2390377345808152832	2390377350103204096*	2021.017	0.86	$\pm 0.20^{+0.03}_{-0.02}$	23%	9.8%
47		3670594366739201664	3670594366739201536*	2021.115	0.65	$\pm 0.13^{+0.02}_{-0.02}$	18%	5.8%
48	L 143-23	5254061535097566848	5254061535097574016	2021.188	0.12	$\pm 0.050^{+0.004}_{-0.004}$	43%	21%
49	HD 44573	2937651222655480832	2937651222651937408*	2021.226	0.77	$\pm 0.18^{+0.02}_{-0.02}$	22%	22%
50	CD-32 12693	5979367986779538432	5979367982463635840	2021.336	0.43	$\pm 0.13^{+0.01}_{-0.01}$	28%	25%
51	75 Cnc	689004018040211072	689004018038546560*	2021.378	1.4	$\pm 0.11^{+0.01}_{-0.01}$	7.6%	5.4%
52	OGLE SMC115.5 319	4687445500635789184	4687445599404851456	2021.500	0.65	$\pm 0.13^{+0.01}_{-0.01}$	20%	12%
53	HD 197484	6677000246203170944	6677000246201701120*	2021.579	0.99	$\pm 0.26^{+0.06}_{-0.04}$	26%	12%
54	LAWD 37	5332606522595645952	5332606350771972352	2022.226	0.65	$\pm 0.31^{+0.03}_{-0.03}$	47%	47%
55	BD+43 4138	1962597885872344704	1962597885867565312*	2022.663	0.96	$\pm 0.48^{+0.07}_{-0.05}$	49%	49%
56	L 100-115	5243594081269535872	5243594081263121792	2022.847	0.17	$\pm 0.054^{+0.005}_{-0.004}$	31%	27%
57	G 100-35B	3398414352092062720	3398414347798489472	2022.859	0.25	$\pm 0.093^{+0.007}_{-0.007}$	37%	33%
58	Proxima Centauri	5853498713160606720	5853498713180840704	2023.349	0.12	$\pm 0.047^{+0.005}_{-0.004}$	40%	40%
59		5340884333294888064	5340884328994222208	2023.559	0.65	$\pm 0.32^{+0.03}_{-0.03}$	49%	48%
60	HD 18757	466294295706341760	466294295706435712	2023.762	1	$\pm 0.36^{+0.03}_{-0.03}$	35%	34%
61	Proxima Centauri	5853498713160606720	5853498713180846592	2023.849	0.12	$\pm 0.034^{+0.002}_{-0.003}$	28%	27%
62	OGLE LMC162.5 41235	465798264349556608	4657982639152973184	2024.283	0.65	$\pm 0.23^{+0.02}_{-0.02}$	35%	30%
63	L 31-84	462388263033283328	462388263033283968	2024.593	0.35	$\pm 0.088^{+0.007}_{-0.007}$	25%	12%
64	61 Cyg B	1872046574983497216	1872046605038072448	2024.661	0.55	$\pm 0.14^{+0.01}_{-0.01}$	24%	11%
65	HD 207450	6585158207436506368	6585158211732350592*	2025.805	1.2	$\pm 0.44^{+0.06}_{-0.09}$	35%	3.5%

TABLE A.4: Estimated uncertainties of mass measurements with astrometric microlensing with *Gaia* for multiple background sources. The table lists the name (Name-Lens) and *Gaia* DR2 source ID (*DR2_ID*) of the lens and DR2 source IDs of the background sources. The background sources are grouped into sources where *Gaia* DR2 does only provides only the position (2-parameter), sources with a full 5-parameter solution (5-parameter), and sources with a 5-parameter solution in combination with an expected precision in along-scan direction better than of 0.5 mas (sigma). The assumed mass of the lens is listed in M_{in} , and the expected precisions of the mass determination for the three cases are given in σ_{M_x}/M_{in} , including the uncertainty due to the errors in the input parameters, as well as the percentage in σ_{M_x}/M_{in} , where x indicates the use of all background stars (all), background stars with a 5-parameters solution (5-par.) and background stars with expected precision in along-scan direction better than of 0.5 mas (sig.) (Klitner et al., 2020, Table 3).

#	Name-Lens <i>DR2_ID</i> -Lens	<i>DR2_ID</i> -Source (2-parameter)	<i>DR2_ID</i> -Source (5-parameter)	<i>DR2_ID</i> -Source (sigma)	M_{in} M_{\odot}	$\sigma_{M_{all}}$ M_{\odot}	$\sigma_{M_{all}}/M_{in}$ %	$\sigma_{M_{5-par}}$ M_{\odot}	$\sigma_{M_{5-par}}/M_{in}$ %	$\sigma_{M_{sig}}$ M_{\odot}	$\sigma_{M_{sig}}/M_{in}$ %
A	Proxima Cen 585349871316066720	5853498713161902848	5853498713162466688	5853498713181091840	0.12	$\pm 0.012^{+0.001}_{-0.001}$	10%	$\pm 0.012^{+0.001}_{-0.001}$	10%	$\pm 0.012^{+0.001}_{-0.001}$	10%
		5853498713161549312	5853498713161800504	5853498713180846720	1.888						
			5853498713160604800	5853498713180846720							
			585349864442433280	5853498713160651648							
			5853498644461348864	5853498713180846592							
B	5312099874809857024	5853498713160648448	5853498713160648448	5853498713181092224							
		5853498713160653088	5853498713180840704								
		5853498713161549440	5853498708818460032								
			5312099874795679488								
			451619931338490936	4516199313402714368	0.43	$\pm 0.065^{+0.004}_{-0.005}$	15%				$\pm 0.066^{+0.005}_{-0.006}$
C	Ross 733 4516199240734836608										
D	LAWD 37 5332606522595645952										
E	61 Cyg B 1872046574983497216	1872046609337556608	1872046605038072448		0.55	$\pm 0.14^{+0.01}_{-0.01}$	24%			$\pm 0.14^{+0.01}_{-0.02}$	24%
		1872046609337556608	1872046609337556608								
F	61 Cyg A 1872046574983907456	1872046609337556608	1872047330897752832		0.63	$\pm 0.21^{+0.02}_{-0.02}$	32%			$\pm 0.33^{+0.03}_{-0.03}$	53%
		1872046609337556608	1872046609337556608								
G	L 143-23 5254061533097566848	5254061533097566848	5254061533097566848		0.12	$\pm 0.043^{+0.003}_{-0.003}$	37%			$\pm 0.051^{+0.004}_{-0.004}$	44%
		5254061533097566848	5254061533097566848								
H	James' star 5339892367683264384	5339892367683264384	5339892367683264384	0.33	$\pm 0.16^{+0.01}_{-0.01}$	47%			$\pm 0.16^{+0.02}_{-0.02}$	48%	

List of Figures

2.1	Light deflection by a point mass	5
2.2	Distortion due to gravitational lensing	7
2.3	Light curves of photometric microlensing events	10
2.4	Positional shift of an astrometric microlensing event	14
2.5	Comparison between astrometric microlensing and photometric microlensing	17
3.1	Illustration of <i>Gaia</i> 's scanning law	20
3.2	Number of focal-plane transits for the nominal mission of <i>Gaia</i>	21
3.3	Focal plane of <i>Gaia</i>	22
3.4	Illustration of the readout windows	23
4.1	Proper motions vs parallaxes of the high-proper-motion stars	29
4.2	Number of photometric observations vs significance of the G flux	30
4.3	Distribution of the high-proper-motion stars, and the excluded objects on the sky	31
4.4	Illustration of the sky window used in the search for background stars	33
4.5	Colour-absolute magnitude diagram of all potential lenses	35
4.6	$G_{abs} - M$ relation	36
4.7	Distribution of the predicted events on the sky	38
4.8	Temporal distribution of the predicted events	39
4.9	Maximum shifts for all expected events between 2014.5 and 2026.5	41
4.10	Image of Luyten 143-23 and Ross 322	43
4.11	Predicted motions of the background stars for the events by Luyten 143-23 and by Ross 322)	46
4.12	Expected maximum magnification for all photometric events	47
5.1	Illustration of our simulation	52
5.2	Precision in along-scan direction as function of G magnitude	57
5.3	Histogram of the simulated mass determination	60
5.4	Distribution of the assumed masses and the resulting relative standard error from the extended mission	62
5.5	Distribution of the assumed masses and the resulting relative standard error from the nominal mission	63
5.6	Distribution of the G magnitude of the source and impact parameter	65

5.7	Achievable standard error as a function of the input mass	66
5.8	Violin plot of the achievable uncertainties (A-D)	69
5.9	Violin plot of the achievable uncertainties (E-H)	70

List of Tables

3.1	End-of-mission sky average astrometric performance	25
4.1	Quality cuts for the prediction of microlensing events	37
A.1	List of 30 especially promising astrometric microlensing events	76
A.2	Estimated uncertainties of mass measurements with astrometric microlensing with <i>Gaia</i> for single events with an epoch of the closest approach during the nominal <i>Gaia</i> mission	77
A.3	Estimated uncertainties of mass measurements with astrometric microlensing with <i>Gaia</i> for single events with an epoch of the closest approach after 2019.5 .	78
A.4	Estimated uncertainties of mass measurements with astrometric microlensing with <i>Gaia</i> for multiple background sources	79

List of Abbreviations

2MASS	Two Micron All Sky Survey
AC	ACross-scan direction
AL	ALong-scan direction
ESA	European Space Agency
FWHM	Full Width at Half Maximum
<i>Gaia</i> DR1	<i>Gaia</i> Data Release 1
Gaia DR2	<i>Gaia</i> Data Release 2
Gaia DR3	<i>Gaia</i> Data Release 3
Gaia DR4	<i>Gaia</i> Data Release 4
Gaia DR5	<i>Gaia</i> Data Release 5
Gaia eDR3	early <i>Gaia</i> Data Release 3
GAVO	German Astrophysical Virtual Observatory,
GOST	Gaia observation forecast tool
HPMS	High-Proper-Motion Stars
HST	Hubble Space Telescope
JWST	James Web Space Telescope
KMTnet	Korea Microlensing Telescope Network
L2	Lagrangian Point L2 of the Sun-Earth system
MS	Main-Sequence stars
MOA	Microlensing Observations in Astrophysics
OGLE	Optical Gravitational Lensing Experiment
Pan-STARRS	Panoramic Survey Telescope And Rapid Response System
RG	Red Giants

SPHERE	Spectro-Polarimetric High-contrast Exoplanet REsearch
VLT	Very Large Telescope
VLTI	Very Large Telescope Interferometer
WD	White Dwarfs
WFC3	Wide Field Camera 3

Publications of Jonas Klüter

First author publications:

- **Klüter, J.**, Bastian, U. and Wambsganss, J.
“Expectations on the mass determination using astrometric microlensing by Gaia” (Chapter 5)
 2020, *Astronomy & Astrophysics*, in press [arXiv:1911.02584]
- **Klüter, J.**, Bastian, U., Demleitner, M. and Wambsganss, J.
“Prediction of astrometric microlensing events from Gaia DR2 proper motions” (Chapter 4)
 2018b, *Astronomy & Astrophysics*, 620, A175
- **Klüter, J.**, Bastian, U., Demleitner, M. and Wambsganss, J.
“ongoing astrometric microlensing events of two nearby stars” (Chapter 4)
 2018a, *Astronomy & Astrophysics*, 615, L11

Co-authored publications:

- Krone-Martins, A., Graham, M. J., Stern, D., Djorgovski, S. G. and Delchambre, L., Ducourant, C., Teixeira, R., Drake, A. J., Scarano, S., Jr., Surdej, J., Galluccio, L., Jalan, P., Wertz, O., **Klüter, J.**, Mignard, F., Spindola-Duarte, C., Dobie, D., Slezak, E. and Sluse, D., Murphy, T., Boehm, C., Nierenberg, A. M., Bastian, U., Wambsganss, J., and LeCampion, J. -F.
“Gaia GrAL: Gaia DR2 Gravitational Lens Systems. V. Doubly-imaged QSOs discovered from entropy and wavelets”
 2019, submitted to *Astronomy & Astrophysics*, [arXiv:1912.08977]
- Wertz, O., Stern, D., Krone-Martins, A., Delchambre, L., Ducourant, C., Gråe Jørgensen, U., Dominik, M., Burgdorf, M., Surdej, J., Mignard, F., Teixeira, R., Galluccio, L., **Klüter, J.**, Djorgovski, S. G., Graham, M. J., Bastian, U., Wambsganss, J., Boehm, C., LeCampion, J. -F. and Slezak, E.
“Gaia GrAL: Gaia DR2 gravitational lens systems. IV. Keck/LRIS spectroscopic confirmation of GRAL 113100-441959 and model prediction of time delays”
 2019, *Astronomy & Astrophysics*, 628, A17

- Delchambre, L., Krone-Martins, A., Wertz, O., Ducourant, C., Galluccio, L., **Klüter, J.**, Mignard, F., Teixeira, R., Djorgovski, S. G., Stern, D., Graham, M. J., Surdej, J., Bastian, U., Wambsganss, J., Le Campion, J. -F., Slezak, E.
“Gaia GraL: Gaia DR2 Gravitational Lens Systems. III. A systematic blind search for new lensed systems”
 2019, *Astronomy & Astrophysics*, 622, A165
- Ducourant, C., Wertz, O., Krone-Martins, A., Teixeira, R., Le Campion, J. -F., Galluccio, L., **Klüter, J.**, Delchambre, L., Surdej, J., Mignard, F., Wambsganss, J., Bastian, U., Graham, M. J., Djorgovski, S. G. and Slezak, E.
“Gaia GraL: Gaia DR2 gravitational lens systems. II. The known multiply imaged quasars”
 2018, *Astronomy & Astrophysics*, 618, A56
- Krone-Martins, A., Delchambre, L., Wertz, O., Ducourant, C., Mignard, F., Teixeira, R., **Klüter, J.**, Le Campion, J. -F., Galluccio, L., Surdej, J., Bastian, U., Wambsganss, J., Graham, M. J., Djorgovski, S. G. and Slezak, E.
“Gaia GraL: Gaia DR2 gravitational lens systems. I. New quadruply imaged quasar candidates around known quasars”
 2018, *Astronomy & Astrophysics*, 616, L11
- Krone-Martins, A., Delchambre, L., Wertz, O., Ducourant, C., Mignard, F., Teixeira, R., **Klüter, J.**, Le Campion, J. -F., Galluccio, L., Surdej, J., Bastian, U., Wambsganss, J., Graham, M. J., Djorgovski, S. G. and Slezak, E.
“Gaia GraL: Gaia DR2 gravitational lens systems. I. New quadruply imaged quasar candidates around known quasars”
 2018, *Astronomy & Astrophysics*, 616, L11
- Morales, J. C., Mustill, A. J., Ribas, I., Davies, M. B., et al. (including **Klüter, J.**)
“A giant exoplanet orbiting a very-low-mass star challenges planet formation models”
 2019, *Science*, 365, p1441-1445
- Zechmeister, M., Dreizler, S., Ribas, I., Reiners, A., et al. (including **Klüter, J.**)
“The CARMENES search for exoplanets around M dwarfs. Two temperate Earth-mass planet candidates around Teegarden’s Star”
 2018, *Astronomy & Astrophysics*, 627, A49
- Reiners, A., Zechmeister, M., Caballero, J. A., Ribas A., et al. (including **Klüter, J.**)
“The CARMENES search for exoplanets around M dwarfs. High-resolution optical and near-infrared spectroscopy of 324 survey stars”
 2018, *Astronomy & Astrophysics*, 612, A49

- Trifonov, T., Kürster, M., Zechmeister, M., Tal-Or, L., et al. (including **Klüter, J.**)
“*The CARMENES search for exoplanets around M dwarfs . First visual-channel radial-velocity measurements and orbital parameter updates of seven M-dwarf planetary systems*”
2018, *Astronomy & Astrophysics*, 609, A117
- Reiners, A., Ribas, I., Zechmeister, M., Caballero, J. A., et al. (including **Klüter, J.**)
“*The CARMENES search for exoplanets around M dwarfs. HD147379 b: A nearby Neptune in the temperate zone of an early-M dwarf*”
2018, *Astronomy & Astrophysics*, 609, L5

Bibliography

- Alcock, C., Akerlof, C. W., Allsman, R. A., Axelrod, T. S., et al. (1993). Possible gravitational microlensing of a star in the Large Magellanic Cloud. *Nature*, 365(6447):621–623.
- Andersen, J. (1991). Accurate masses and radii of normal stars. *A&A Rev.*, 3(2):91–126.
- Andrae, R., Fouesneau, M., Creevey, O., Ordenovic, C., et al. (2018). Gaia Data Release 2. First stellar parameters from Apsis. *A&A*, 616:A8.
- Aubourg, E., Bareyre, P., Bréhin, S., Gros, M., et al. (1993). Evidence for gravitational microlensing by dark objects in the Galactic halo. *Nature*, 365(6447):623–625.
- Belokurov, V. A. and Evans, N. W. (2002). Astrometric microlensing with the GAIA satellite. *MNRAS*, 331(3):649–665.
- Bennett, D. P. (2005). Large Magellanic Cloud Microlensing Optical Depth with Imperfect Event Selection. *ApJ*, 633(2):906–913.
- Bond, I. A., Abe, F., Dodd, R. J., Hearnshaw, J. B., et al. (2001). Real-time difference imaging analysis of MOA Galactic bulge observations during 2000. *MNRAS*, 327:868–880.
- Bond, I. A., Udalski, A., Jaroszyński, M., Rattenbury, N. J., et al. (2004). OGLE 2003-BLG-235/MOA 2003-BLG-53: A Planetary Microlensing Event. *ApJ*, 606(2):L155–L158.
- Brainerd, T. G., Blandford, R. D., and Smail, I. (1996). Weak Gravitational Lensing by Galaxies. *ApJ*, 466:623.
- Bramich, D. M. (2018). Predicted microlensing events from analysis of Gaia Data Release 2. *A&A*, 618:A44.
- Bramich, D. M. and Nielsen, M. B. (2018). An Almanac of Predicted Microlensing Events for the 21st Century. *Acta Astron.*, 68(3):183–203.
- Branch, M. A., Coleman, T. F., and Li, Y. (1999). A subspace, interior, and conjugate gradient method for large-scale bound-constrained minimization problems. *SIAM Journal on Scientific Computing*, 21(1):1–23.
- Bruns, D. G. (2018). Gravitational starlight deflection measurements during the 21 August 2017 total solar eclipse. *Classical and Quantum Gravity*, 35(7):075009.

- Carrasco, J. M., Evans, D. W., Montegriffo, P., Jordi, C., et al. (2016). Gaia data release 1 - principles of the photometric calibration of the g band. *A&A*, 595:A7.
- Cassan, A., Kubas, D., Beaulieu, J. P., Dominik, M., et al. (2012). One or more bound planets per Milky Way star from microlensing observations. *Nature*, 481(7380):167–169.
- Chambers, K. and Pan-STARRS Team (2018). The Pan-STARRS1 Surveys. In *American Astronomical Society Meeting Abstracts 231*, page 102.01.
- Chaplin, W. J., Basu, S., Huber, D., Serenelli, A., et al. (2014). Asteroseismic Fundamental Properties of Solar-type Stars Observed by the NASA Kepler Mission. *ApJS*, 210(1):1.
- Chung, S.-J., Zhu, W., Udalski, A., Lee, C.-U., et al. (2017). OGLE-2015-BLG-1482l: The first isolated low-mass microlens in the galactic bulge. *The Astrophysical Journal*, 838(2):154.
- Chwolson, O. (1924). Über eine mögliche Form fiktiver Doppelsterne. *Astronomische Nachrichten*, 221:329.
- Clowe, D., Bradač, M., Gonzalez, A. H., Markevitch, M., et al. (2006). A Direct Empirical Proof of the Existence of Dark Matter. *ApJ*, 648(2):L109–L113.
- Coe, D., Zitrin, A., Carrasco, M., Shu, X., et al. (2012). CLASH: THREE STRONGLY LENSED IMAGES OF a CANDIDATE $z \approx 11$ GALAXY. *The Astrophysical Journal*, 762(1):32.
- Cohen, I. B. (1998). Newton’s determination of the masses and densities of the Sun, Jupiter, Saturn and the Earth. *Archive for History of Exact Sciences*, 53(1):83–95.
- Congdon, A. B. and Keeton, C. (2018). *Principles of Gravitational Lensing: Light Deflection as a Probe of Astrophysics and Cosmology*.
- de Bruijne, J., Siddiqui, H., Lammers, U., Hoar, J., et al. (2010). Optimising the Gaia scanning law for relativity experiments. In Klioner, S. A., Seidelmann, P. K., and Soffel, M. H., editors, *Relativity in Fundamental Astronomy: Dynamics, Reference Frames, and Data Analysis*, volume 261 of *IAU Symposium*, pages 331–333.
- Delchambre, L., Krone-Martins, A., Wertz, O., Ducourant, C., et al. (2019). Gaia GraL: Gaia DR2 Gravitational Lens Systems. III. A systematic blind search for new lensed systems. *A&A*, 622:A165.
- Dominik, M. and Sahu, K. C. (2000). Astrometric Microlensing of Stars. *ApJ*, 534(1):213–226.
- Dong, S., Mérand, A., Delplancke-Ströbele, F., Gould, A., et al. (2019). First resolution of microlensed images. *The Astrophysical Journal*, 871(1):70.

- Dyson, F. W., Eddington, A. S., and Davidson, C. (1920). A Determination of the Deflection of Light by the Sun's Gravitational Field, from Observations Made at the Total Eclipse of May 29, 1919. *Philosophical Transactions of the Royal Society of London Series A*, 220:291–333.
- Einstein, A. (1915). Erklärung der Perihelbewegung des Merkur aus der allgemeinen Relativitätstheorie. *Sitzungsber. Preuss. Akad. Wiss.*, 47:831–839.
- Einstein, A. (1916). Die grundlage der allgemeinen relativitätstheorie. *Annalen der Physik*, 354(7):769–822.
- Einstein, A. (1936). Lens-Like Action of a Star by the Deviation of Light in the Gravitational Field. *Science*, 84:506–507.
- Evans, D. W., Riello, M., De Angeli, F., Carrasco, J. M., et al. (2018). Gaia Data Release 2. Photometric content and validation. *A&A*, 616:A4.
- Fabrizius, C., Bastian, U., Portell, J., Castañeda, J., et al. (2016). Gaia Data Release 1. Pre-processing and source list creation. *A&A*, 595:A3.
- Finet, F. and Surdej, J. (2016). Multiply imaged quasi-stellar objects in the Gaia survey. *A&A*, 590:A42.
- Gaia Collaboration, Brown, A. G. A., Vallenari, A., Prusti, T., et al. (2018). Gaia Data Release 2. Summary of the contents and survey properties. *A&A*, 616:A1.
- Gaia Collaboration, Brown, A. G. A., Vallenari, A., Prusti, T., et al. (2016a). Gaia Data Release 1. Summary of the astrometric, photometric, and survey properties. *A&A*, 595:A2.
- Gaia Collaboration, Prusti, T., de Bruijne, J. H. J., Brown, A. G. A., et al. (2016b). The Gaia mission. *A&A*, 595:A1.
- Gould, A. (1992). Extending the MACHO Search to approximately $10^6 M_{\text{sub sun}}$. *ApJ*, 392:442.
- Gould, A. (1994a). MACHO Velocities from Satellite-based Parallaxes. *ApJ*, 421:L75.
- Gould, A. (1994b). Proper Motions of MACHOs. *ApJ*, 421:L71.
- Gratton, R., Zurlo, A., Le Coroller, H., Damasso, M., et al. (2020). Searching for the near infrared counterpart of Proxima c using multi-epoch high contrast SPHERE data at VLT. *arXiv e-prints*, page arXiv:2004.06685.
- Griest, K., Cieplak, A. M., and Lehner, M. J. (2013). New Limits on Primordial Black Hole Dark Matter from an Analysis of Kepler Source Microlensing Data. *Phys. Rev. Lett.*, 111(18):181302.

- Halbwachs, J. L., Boffin, H. M. J., Le Bouquin, J. B., Kiefer, F., et al. (2016). Masses of the components of SB2s observed with Gaia - II. Masses derived from PIONIER interferometric observations for Gaia validation. *MNRAS*, 455(3):3303–3311.
- Hertzsprung, E. (1923). On the relation between mass and absolute brightness of components of double stars. *Bull. Astron. Inst. Netherlands*, 2:15.
- Hog, E., Novikov, I. D., and Polnarev, A. G. (1995). MACHO photometry and astrometry. *A&A*, 294:287–294.
- Honma, M. (2001). Detecting Galactic MACHOs with VERA through Astrometric Microlensing of Distant Radio Sources. *PASJ*, 53:233–241.
- Jordi, C., Gebran, M., Carrasco, J. M., de Bruijne, J., et al. (2010). Gaia broad band photometry. *A&A*, 523:A48.
- Kaiser, N. and Squires, G. (1993). Mapping the Dark Matter with Weak Gravitational Lensing. *ApJ*, 404:441.
- Kim, S.-L., Lee, C.-U., Park, B.-G., Kim, D.-J., et al. (2016). KMTNET: A Network of 1.6 m Wide-Field Optical Telescopes Installed at Three Southern Observatories. *Journal of Korean Astronomical Society*, 49(1):37–44.
- Klüter, J., Bastian, U., Demleitner, M., and Wambsganss, J. (2018a). Ongoing astrometric microlensing events of two nearby stars. *A&A*, 615:L11.
- Klüter, J., Bastian, U., Demleitner, M., and Wambsganss, J. (2018b). Prediction of astrometric microlensing events from Gaia DR2 proper motions. *A&A*, 620:A175.
- Klüter, J., Bastian, U., and Wambsganss, J. (2020). Expectations on the mass determination using astrometric microlensing by Gaia. *A&A*, in press:arXiv:1911.02584.
- Krone-Martins, A., Delchambre, L., Wertz, O., Ducourant, C., et al. (2018). Gaia GraL: Gaia DR2 gravitational lens systems. I. New quadruply imaged quasar candidates around known quasars. *A&A*, 616:L11.
- Krone-Martins, A., Graham, M. J., Stern, D., Djorgovski, S. G., et al. (2019). Gaia GraL: Gaia DR2 Gravitational Lens Systems. V. Doubly-imaged QSOs discovered from entropy and wavelets. *arXiv e-prints*, page arXiv:1912.08977.
- Lemon, C. A., Auger, M. W., McMahon, R. G., and Ostrovski, F. (2018). Gravitationally lensed quasars in Gaia - II. Discovery of 24 lensed quasars. *MNRAS*, 479(4):5060–5074.
- Lindgren, L., Hernández, J., Bombrun, A., Klioner, S., et al. (2018). Gaia Data Release 2. The astrometric solution. *A&A*, 616:A2.

- Lindegren, L., Lammers, U., Bastian, U., Hernández, J., et al. (2016). Gaia Data Release 1. Astrometry: one billion positions, two million proper motions and parallaxes. *A&A*, 595:A4.
- Luri, X., Brown, A. G. A., Sarro, L. M., Arenou, F., et al. (2018). Gaia Data Release 2. Using Gaia parallaxes. *A&A*, 616:A9.
- McGill, P., Smith, L. C., Evans, N. W., Belokurov, V., and Lucas, P. W. (2019a). Ongoing astrometric microlensing events from VVV and Gaia. *MNRAS*, 487(1):L7–L12.
- McGill, P., Smith, L. C., Evans, N. W., Belokurov, V., and Smart, R. L. (2018). A predicted astrometric microlensing event by a nearby white dwarf. *MNRAS*, 478(1):L29–L33.
- McGill, P., Smith, L. C., Evans, N. W., Belokurov, V., and Smart, R. L. (2018). A predicted astrometric microlensing event by a nearby white dwarf. *Monthly Notices of the Royal Astronomical Society: Letters*, 478(1):L29–L33.
- McGill, P., Smith, L. C., Evans, N. W., Belokurov, V., and Zhang, Z. H. (2019b). Microlens mass determination for Gaia’s predicted photometric events. *MNRAS*, 483(3):4210–4220.
- Mignard, F. (2005). Overall Science Goals of the Gaia Mission. In Turon, C., O’Flaherty, K. S., and Perryman, M. A. C., editors, *The Three-Dimensional Universe with Gaia*, volume 576 of *ESA Special Publication*, page 5.
- Miralda-Escude, J. (1996). Microlensing Events from Measurements of the Deflection. *ApJ*, 470:L113.
- Miyamoto, M. and Yoshii, Y. (1995). Astrometry for Determining the MACHO Mass and Trajectory. *AJ*, 110:1427.
- Mróz, P., Udalski, A., Skowron, J., Szymański, M. K., et al. (2019). Microlensing Optical Depth and Event Rate toward the Galactic Bulge from 8 yr of OGLE-IV Observations. *ApJS*, 244(2):29.
- Mustill, A. J., Davies, M. B., and Lindegren, L. (2018a). 20 years of photometric microlensing events predicted by Gaia DR2: Potential planet-hosting lenses within 100 pc. *ArXiv e-prints*.
- Mustill, A. J., Davies, M. B., and Lindegren, L. (2018b). Twenty years of photometric microlensing events predicted by Gaia DR2. Potential planet-hosting lenses within 100 pc. *A&A*, 617:A135.
- Nielsen, M. B. and Bramich, D. M. (2018). Predicted Microlensing Events by Nearby Very-Low-Mass Objects: Pan-STARRS DR1 vs. Gaia DR2. *Acta Astron.*, 68(4):351–370.
- Ostrovski, F., Lemon, C. A., Auger, M. W., McMahon, R. G., et al. (2018). The discovery of a five-image lensed quasar at $z = 3.34$ using PanSTARRS1 and Gaia. *MNRAS*, 473(1):L116–L120.

- Paczynski, B. (1986a). Gravitational microlensing at large optical depth. *ApJ*, 301:503–516.
- Paczynski, B. (1986b). Gravitational Microlensing by the Galactic Halo. *ApJ*, 304:1.
- Paczynski, B. (1991). Gravitational microlensing of the Galactic bulge stars. *ApJ*, 371:L63–L67.
- Paczynski, B. (1995). The Masses of Nearby Dwarfs Can Be Determined with Gravitational Microlensing. *Acta Astron.*, 45:345–348.
- Paczynski, B. (1996a). Gravitational Microlensing in the Local Group. *ARA&A*, 34:419–460.
- Paczynski, B. (1996b). The Masses of Nearby Dwarfs and Brown Dwarfs with the HST. *Acta Astron.*, 46:291–296.
- Paczynski, B. (1998). Gravitational Microlensing with the Space Interferometry Mission. *ApJ*, 494:L23–L26.
- Pecaut, M. J. and Mamajek, E. E. (2013). Intrinsic Colors, Temperatures, and Bolometric Corrections of Pre-main-sequence Stars. *ApJS*, 208:9.
- Pourbaix, D., Tokovinin, A. A., Batten, A. H., Fekel, F. C., et al. (2004). *S_B9* The ninth catalogue of spectroscopic binary orbits. *A&A*, 424:727–732.
- Proft, S., Demleitner, M., and Wambsganss, J. (2011). Prediction of astrometric microlensing events during the Gaia mission. *A&A*, 536:A50.
- Refsdal, S. (1964). On the possibility of determining Hubble's parameter and the masses of galaxies from the gravitational lens effect. *MNRAS*, 128:307.
- Russell, H. N., Adams, W. S., and Joy, A. H. (1923). A Comparison of Spectroscopic and Dynamical Parallaxes. *PASP*, 35(206):189.
- Rybicki, K. A., Wyrzykowski, Ł., Klencki, J., de Bruijne, J., et al. (2018). On the accuracy of mass measurement for microlensing black holes as seen by Gaia and OGLE. *MNRAS*, 476:2013–2028.
- Sahu, K. C., Anderson, J., Bellini, A., Belokurov, V., et al. (2019a). Accurate Mass Determination of the Nearby Single White Dwarf L145-141 (LAWD 37) through Astrometric Microlensing. HST Proposal.
- Sahu, K. C., Anderson, J., Bellini, A., Belokurov, V., et al. (2019b). Mass determination of an extreme halo M subdwarf through astrometric and photometric microlensing. HST Proposal.
- Sahu, K. C., Anderson, J., Casertano, S., Bond, H. E., et al. (2017). Relativistic deflection of background starlight measures the mass of a nearby white dwarf star. *Science*, 356:1046–1050.

- Sahu, K. C., Bond, H. E., Anderson, J., and Dominik, M. (2014). Microlensing Events by Proxima Centauri in 2014 and 2016: Opportunities for Mass Determination and Possible Planet Detection. *ApJ*, 782:89.
- Salaris, M. and Cassisi, S. (2005). *Evolution of Stars and Stellar Populations*.
- Salim, S. and Gould, A. (2000). Nearby Microlensing Events: Identification of the Candidates for the Space Interferometry Mission. *ApJ*, 539:241–257.
- Shvartzvald, Y., Yee, J. C., Skowron, J., Lee, C.-U., et al. (2019). Spitzer microlensing parallax for OGLE-2017-BLG-0896 reveals a counter-rotating low-mass brown dwarf. *The Astronomical Journal*, 157(3):106.
- Skrutskie, M. F., Cutri, R. M., Stiening, R., Weinberg, M. D., et al. (2006). The Two Micron All Sky Survey (2MASS). *AJ*, 131:1163–1183.
- Soldner, J. (1801). Über die ablenkung eines lichtstrahls von seiner geradlinigen bewegung durch die attraktion eines weltkörpers, an welchem er nahe vorbeigeht. *Berliner Astronomisches Jahrbuch, 1804*, 161.
- Tisserand, P., Le Guillou, L., Afonso, C., Albert, J. N., et al. (2007). Limits on the Macho content of the Galactic Halo from the EROS-2 Survey of the Magellanic Clouds. *A&A*, 469(2):387–404.
- Torres, G., Andersen, J., and Giménez, A. (2010). Accurate masses and radii of normal stars: modern results and applications. *A&A Rev.*, 18:67–126.
- Udalski, A. (2003). The Optical Gravitational Lensing Experiment. Real Time Data Analysis Systems in the OGLE-III Survey. *Acta Astron.*, 53:291–305.
- Udalski, A., Szymański, M. K., and Szymański, G. (2015). OGLE-IV: Fourth Phase of the Optical Gravitational Lensing Experiment. *Acta Astron.*, 65:1–38.
- Walker, M. A. (1995). Microlensed Image Motions. *ApJ*, 453:37.
- Walsh, D., Carswell, R. F., and Weymann, R. J. (1979). 0957+561 A, B: twin quasistellar objects or gravitational lens? *Nature*, 279:381–384.
- Wertz, O., Stern, D., Krone-Martins, A., Delchambre, L., et al. (2019). Gaia GraL: Gaia DR2 gravitational lens systems. IV. Keck/LRIS spectroscopic confirmation of GRAL 113100-441959 and model prediction of time delays. *A&A*, 628:A17.
- Wyrykowski, Ł., Kostrzewa-Rutkowska, Z., Skowron, J., Rybicki, K. A., et al. (2016). Black hole, neutron star and white dwarf candidates from microlensing with OGLE-III. *MNRAS*, 458(3):3012–3026.

- Wyrzykowski, Ł., Mróz, P., Rybicki, K. A., Gromadzki, M., et al. (2020). Full orbital solution for the binary system in the northern Galactic disc microlensing event Gaia16aye. *A&A*, 633:A98.
- Zang, W., Shvartzvald, Y., Wang, T., Udalski, A., et al. (2020). Spitzer microlensing parallax reveals two isolated stars in the galactic bulge. *The Astrophysical Journal*, 891(1):3.
- Zheng, W., Postman, M., Zitrin, A., Moustakas, J., et al. (2012). A magnified young galaxy from about 500 million years after the Big Bang. *Nature*, 489(7416):406–408.
- Zhu, W., Calchi Novati, S., Gould, A., Udalski, A., et al. (2016). Mass Measurements of Isolated Objects from Space-based Microlensing. *ApJ*, 825(1):60.
- Zurlo, A., Gratton, R., Mesa, D., Desidera, S., et al. (2018). The gravitational mass of Proxima Centauri measured with SPHERE from a microlensing event. *MNRAS*, 480(1):236–244.
- Zwicky, F. (1937). On the Masses of Nebulae and of Clusters of Nebulae. *ApJ*, 86:217.

Statement of Authorship - Selbstständigkeitserklärung

Ich, Jonas Klüter, versichere, dass ich diese Dissertation selbstständig verfasst habe und keine anderen als die angegebenen Quellen und Hilfsmittel benutzt habe.

Acknowledgements

At the end of this thesis, I wish to acknowledge everyone who supported me on my way to this dissertation. I could not have done this without you.

First and foremost I would like to thank my supervisor Joachim Wambsganß. I am immensely thankful for all the possibilities you offered me during my time at the Astronomisches Rechen-Institut, for all the scientific advice and for the financial support during the work on this thesis. To the same extent, I would like to thank Ulrich Bastian. I am very grateful for all the time and feedback you gave me, and all your patience.

It was a pleasure for me to do my research under your supervision. Your mentorship, encouragement, and advice have been invaluable.

I would like to thank Jochen Heidt, for his immediate agreement to be the second corrector of my dissertation and for being a member of my thesis committee.

I also want to thank Anna Pasquali and André Butz for completing my examination committee.

I would like to thank Markus Hundertmark, Robert Schmidt, Yiannis Tsapras, and all other members of the Lensing Group for the many discussions in and outside of our group seminar, for giving me feedback on my research and the innumerable little things in the last years.

I would like to thank the Gaia GraL group for the warm welcome, in particular, Ludovic Delchambre, Olivier Wertz, Laurent Galluccio, Christine Ducourant, François Mignard and especially, Alberto Krone-Martins.

It is a pleasure for me to search for lensed quasars with you, and I will never forget the x-hour video conference after the release of Gaia DR2.

Another thank you goes out to Markus Demleitner for his support to access the Gaia database.

Finally, I want to thank my parents, siblings and my closest friends who always believed in me. I am so glad that you accompany me on my way. What would I do without you?

*“All I know:
Time is a valuable thing
Watch it fly by as the pendulum swings”*

In the End, LINKIN PARK